Winter 12-15-2015

Implications of a Fully Nonlocal Implementation of the Dispersive Optical Model

MohammadHossein Mahzoon
Washington University in St. Louis

WASHINGTON UNIVERSITY IN ST. LOUIS

Department of Physics

Dissertation Examination Commitee:
Willem H. Dickhoff, Chair
Mark Alford
Robert J. Charity
Demetrios G. Sarantites
Lee G. Sobotka

Implications of a Fully Nonlocal Implementation of the Dispersive Optical Model

by

Mohammadhossein Mahzoon

A dissertation presented to the
Graduate School of Arts and Sciences
of Washington University in
partial fulfillment of the
requirements for the degree
of Doctor of Philosophy

December 2015
Saint Louis, Missouri

Contents

List of Figures

List of Tables

Acknowledgements

I would like to express my special appreciation and thanks to my advisor Wim Dickhoff for his patience and guidance. I would like to thank you for encouraging my research and for allowing me to grow as a researcher. Your advice on both research as well as on my career have been invaluable. Having daily meetings with you indicates your wonderful mentoring and helped me tremendously getting to this point.

I would especially like to thank Bob Charity for his considerable help in the course of my research and learning the details about coding and physical aspects of the DOM.

I would also thank my committee members Mark Alford, Bob Charity, Demetrios Sarantites and Lee Sobotka for serving as my committee and their valuable feedbacks.

During my experience as a graduate student in the physics department I had the opportunity to collaborate with the experimental group in Radio Chemistry. I would like to thank Lee Sobotka, Bob Charity and John Elson for teaching and engaging me in the nuclear experimental area. Thanks for giving me the opportunity to become familiar with experimental tools and methods in nuclear physics.

Working with Demetrios Sarantites for more than three semesters gave me a wonderful

experience in getting to know fundamental experimental and theoretical nuclear physics. I would like to thank you for your devotion and patience in exposing me to several interesting nuclear physics experiments. It was a unique experience for me to learn about the electronics and some smart experimental methods as well as analyzing tools.

I give thanks to Seth Waldecker my wonderful friend and the former PhD student in our group. He was a great help and mentor initiating my research when I first joined the group.

I would also like to thank Helber Dussan for his contributions in developing several aspects of the DOM especially the calculations for positive energies.

I also thank Pawel Danielewicz and Alex Brown for their feedbacks on my visit to Michigan State University.

A special thanks to my family. Words cannot express how grateful I am to my mother and father. Your prayer for me was what sustained me thus far.

This work was supported by the U.S. Department of Energy, Division of Nuclear Physics under Grant No. DE-FG02-87ER-40316 and the U.S. National Science Foundation under Grants No. PHY-0968941 and No. PHY-1304242.

Hossein Mahzoon

Washington University in Saint Louis

December 2015

ABSTRACT OF THE DISSERTATION

Implications of a Fully Nonlocal Implementation of the Dispersive Optical Model

by

MohammadHossein Mahzoon

Doctor of Philosophy in Physics

Washington University in St. Louis, 2015

Professor Willem H. Dickhoff, Chairperson

A fully nonlocal treatment for the dispersive optical model (DOM) is implemented for both the real and imaginary part of the self-energy inspired by ab initio theoretical calculations of this quantity. By means of the dispersion relation between the real and imaginary part of the optical potential a link between the energy domain of nuclear reactions and nuclear structure is established. The relevant scattering data for neutrons and protons on ^{40}Ca are described with the same quality as was accomplished with previous local versions of the DOM. The solution of the Dyson equation at positive and negative energies is generated with a complete treatment of the nonlocality of the potentials. The resulting propagator has been utilized to explain and predict relevant quantities of the ground-state of the ^{40}Ca nucleus. In particular the charge density, spectral strength and particle number can, for the first time, be accurately described. Moreover, due to the introduction of nonlocality in the imaginary part of the self-energy it is also possible to describe high-momentum protons and the contribution of the two-body interaction to the ground-state energy. The calculation of the spectral density at positive energies allows for the determination of the spectral strength of mostly occupied single-particle orbits in the continuum. Consistency of the resulting

depletion numbers with the corresponding occupation numbers is studied and compared to ab initio calculations for these quantities. Starting from the ^{40}Ca self-energy, an extension to the ^{48}Ca nucleus is implemented focusing on the $N - Z$ dependence of the nucleon self-energy. Neutron scattering data can be described with even better quality than previous local DOM calculations. The scattering properties for protons are of similar excellent quality as for previous local results. From the solution of the Dyson equation for neutrons it is possible to calculate the neutron distribution of this nucleus allowing for the determination of the neutron skin which is relevant for the physics of neutron stars. The resulting value is larger than most calculations previously reported including an ab initio one. An argument supporting a large neutron skin is provided by analyzing proton elastic scattering data on both ^{40}Ca and ^{48}Ca.

1 Introduction

One of the most important quantities in nuclear physics is the interaction between a nucleon and the nucleus. It characterizes the elastic and inelastic scattering of nucleons by nuclei and also clarifies the nuclear channels in nuclear reactions. For elastic scattering this interaction is traditionally described by a potential $V(\boldsymbol{r})$ where the vector $\boldsymbol{r}$ is the distance between the nucleon and the center of the target nucleus. Knowing the potential function, the elastic scattering cross section can be extracted by using the formalism of quantum mechanics. It was realized as early as 1959 [1] that the interaction should be considered to be nonlocal, complex as well as energy dependent to generate all essential features both for scattering and bound-states. The knowledge about the so-called self-energy enables the cross-section calculation as a function of energy for nucleons on a required nuclear target. The corresponding distorted wave function can be calculated which is useful for reaction calculations. Therefore it is of great importance both theoretically and experimentally to determine the interaction self-energy as precisely as possible [2]. The same self-energy can be used to generate the properties and motion of the bound nucleons in the nucleus. Thus this self-energy or interaction can be considered as a mean-field that unifies the nuclear structure and nuclear reaction domain since it describes both the scattering and bound-state properties of nucleons.

There are two major ways to determine the self-energy $\Sigma^*_{\ell j}(r, r'; E)$. One is to employ theoretical methods where the nucleon-nucleus interaction is calculated by approximately solving the many-body problem for a given nucleus and nucleon type. The other is the phenomenological approach in which a reasonable functional form for the self-energy is assumed. The form should be physically appropriate and a set of parameters introduced characterizing the self-energy. These are adjusted through a fit process to optimize the description of the available experimental data thereby generating the constrained self-energy, within the required accuracy. Both methods have advantages and drawbacks. In the theoretical approach there is always a computational challenge including the fact that many-body calculations cannot yet accurately describe experiments at this time. In the latter approach there maybe various sets of parameters that can represent the data leading to ambiguities. In this work we are concentrating on the phenomenological approach but use input from the theoretical approach. There are different ways that the nuclear structure of the target nucleus can affect the cross-section pattern. In the case of elastic scattering of a nucleon, the incident nucleon at low energies can be captured by the target nucleus and form a compound system which might decay in various ways. One of the decay channels could be the emission of the incident nucleon at its initial energy. At higher energies the incident nucleon most probably scattered directly, also leading to a loss of flux in the elastic channel. Nuclear structure therefore affects the elastic scattering cross section in this case too.

The shell model or independent-particle model (IPM) calculations generate spectroscopic factors (representing removal probabilities) comparable to unity whereas experiment e.g. the $(e, e'p)$ reaction generates spectroscopic factors of the single-particle excitations that are less than unity. In other words even a low-lying single-particle excitation cannot be considered as one unit particle added to or taken out from the ground state of the many-body system. The $(e, e'p)$ experiments show that the single-particle strength of IPM orbits are highly fragmented. For the orbits close to the Fermi energy, the majority of the strength

is in the vicinity of the IPM level, but still a portion of the overall strength is distributed over a broad energy range.

This reduction in the single-particle strength near the Fermi energy clearly establishes the importance of correlations due to nuclear interactions beyond the IPM. These correlations are mainly of two types. Short-range correlations (SRC) play an important role at higher excitation energies. If two nucleons approach within 1 fm or less, they are considered as a pair influenced by SRC. Their correlation is associated with high relative momenta of the interacting nucleons. Studying SRCs can reveal the nature of short-range nucleon-nucleon interaction and also the contributions of high-momentum nucleons to the nuclear ground state and excited-state wave functions. The SRCs describe two major effects: 1) removing strength from the mean-field orbits and 2) mixing high-momenta into the ground-state. The long-range correlations (LRC) involve interactions of nucleons with low relative momenta and are typically associated with low-energy physics near the Fermi energy.

By allowing the self-energy to be complex, the flux removed by all the channels from the elastic one can be taken into account at positive energy. In this case solving the Schrödinger equation with the complex potential generates the elastic scattering amplitude and therefore all relevant observables. This method is identified with the optical model in analogy to scattering of light that is governed by a complex index of refraction which incorporates both reflection and absorption of light in the medium. Unlike the optical model, in the shell model or IPM the interaction is described by a real potential. Both shell model and optical model play an important role in describing nuclear structure and nuclear reactions. One of the significant properties of the dispersive optical model (DOM) [2] is its ability to establish the link between positive and negative energies. The imaginary and real part of the self-energy are related through a Kramers-Kronig dispersion integral. This dispersion relation therefore connects the nucleons propagating at positive energies to the ones at negative energies. The

link between reaction and structure is therefore created and cross sections as well as bound-state properties are forced to be described simultaneously.

In order to determine the nucleon propagator below the Fermi energy with access to the expectation value of one-body operators (like the charge density), the one-body density matrix with associated natural orbits, and complete spectral functions for removal strength, introducing a generalized "nonlocal" HF potential to the DOM formalism is necessary. This extension was accomplished in Ref. [3]. This extension of the DOM still does not generate the proton charge density in agreement with experimental data. An appropriate convergence could also not be achieved for the total proton numbers when including higher partial waves. These results suggest the introduction of a fully nonlocal self-energy for volume, surface and HF terms. The present nonlocal DOM self-energy allows us to reproduce the bound-state properties (including charge density) as well as scattering data within reasonable errors [4, 5].

One of the questions in nuclear astrophysics is what determines the size of neutron stars. For the so-called Schwarzschild stars the equation of state of the neutron-rich matter determines the size of the neutron star [6]. The skin of a heavy nucleus with $N > Z$ is also composed of neutron-rich matter although at a much lower density [7]. Measuring the neutron skin of heavy nuclei such as ^{208}Pb may therefore have important applications in neutron star properties [8]. A well constrained self-energy that can describe scattering data as well as bound-state properties of the desired nucleus, can be used to extract the neutron skin of that nucleus. This is a very important motivation to apply the nonlocal DOM for heavier nuclei and study their structure.

Investigating the effect of the nonlocal DOM on transfer reactions is of both experimental and theoretical interest. One of the effects of nonlocal DOM ingredients on the description of transfer reactions is studied in [9]. The study shows that the overall effect on the transfer

cross section is very significant when employing the nonlocal DOM. This study clearly motivates further investigation of the consequences of the nonlocal DOM in analyses of transfer reactions. In the future it may therefore be possible to generate a simultaneous description of the bound-state and scattering aspects of transfer reactions thereby clarifying the nuclear structure of target nuclei.

Most of the results presented in Secs. 3.5.1, 3.5.6 and 3.5.4 are published in Ref. [4]. Part of the material in Sec. 2.8 as well as the corresponding results presented in Secs. 3.5.3 and 3.6 were published in Ref. [5].

2 Formalism

2.1 Introduction

In this chapter we introduce the single-nucleon Green's function and the physical quantities that can be derived from this propagator. To understand the precise behavior of a many-body system it is important to have access to the exact propagator which in practice is not possible. In other words, just knowing how to calculate the propagator in a theoretical framework is not sufficient, instead we may attempt to find a way to describe our system as accurately as possible by either finding acceptable approximations or using constraints provided by experimental data. The former procedure needs a detailed insight about the many-body system. The latter is provided by the dispersive optical model (DOM) which will be described in detail in this chapter. Derived from the propagator, spectral functions are useful quantities to analyze the system and gain physical insight. These functions tell us about the single-particle strength distribution in nuclei for example. The DOM, unlike the traditional optical model, enables us to describe and predict nuclear correlations so we can find spectral functions both below and above the Fermi energy to develop a complete understanding of the system.

2.2 Single-particle propagator in a many-body system

The time evolution of a single-particle state and the concept of a propagator can be studied in the case of a quantum-mechanical treatment of a single particle. Consider the quantum state of a particle $|\alpha, t_0\rangle$ at time t_0. At a later time t, the evolved state $|\alpha, t_0, t\rangle$ will be :

$$|\alpha, t_0, t\rangle = e^{-\frac{i}{\hbar}H(t-t_0)}|\alpha, t_0\rangle \tag{2.1}$$

for the time-independent Hamiltonian H. The above equation satisfies the Schrödinger equation:

$$i\hbar\, \partial_t|\alpha, t_0, t\rangle = H|\alpha, t_0, t\rangle \tag{2.2}$$

where ∂_t is partial derivative $\partial/\partial t$. The projection of Eq. (2.1) in coordinate space generates the wave function which can be written as:

$$\begin{aligned} \psi(\boldsymbol{r}, t) &= \langle \boldsymbol{r}|\alpha, t_0; t\rangle = \langle \boldsymbol{r}|e^{-\frac{i}{\hbar}H(t-t_0)}|\alpha, t_0\rangle \\ &= \int d\boldsymbol{r}'\langle \boldsymbol{r}|e^{-\frac{i}{\hbar}H(t-t_0)}|\boldsymbol{r}'\rangle\langle \boldsymbol{r}'|\alpha, t_0\rangle \\ &= i\hbar \int d\boldsymbol{r}'\, G(\boldsymbol{r}, \boldsymbol{r}'; t-t_0)\psi(\boldsymbol{r}', t_0), \end{aligned} \tag{2.3}$$

where G is the propagator or Green's function:

$$G(\boldsymbol{r}, \boldsymbol{r}'; t-t_0) = -\frac{i}{\hbar}\langle \boldsymbol{r}|e^{-\frac{i}{\hbar}H(t-t_0)}|\boldsymbol{r}'\rangle. \tag{2.4}$$

Consider $|\Psi_0^N\rangle$ to be the normalized Heisenberg ground state of the N-body system and E_0^N the corresponding eigenvalue:

$$\hat{H}|\Psi_0^N\rangle = E_0^N|\Psi_0^N\rangle \tag{2.5}$$

with

$$\hat{H} = \hat{T} + \hat{V} = \sum_{\alpha,\beta} \langle \alpha|T|\beta\rangle a^\dagger_\alpha a_\beta + \frac{1}{4} \sum_{\alpha,\beta,\gamma,\delta} \langle \alpha\beta|V|\gamma\delta\rangle a^\dagger_\alpha a^\dagger_\beta a_\delta a_\gamma \tag{2.6}$$

representing the Hamiltonian of the the system using the definition $\langle \alpha\beta|V|\gamma\delta\rangle \equiv (\alpha\beta|V|\gamma\delta) - (\alpha\beta|V|\delta\gamma)$. The single-particle (SP) propagator in the many-body system is defined as [10]:

$$G(\alpha,\beta;t-t') = -\frac{i}{\hbar}\langle \Psi^N_0|\mathcal{T}[a_{\alpha H}(t)a^\dagger_{\beta H}(t')]|\Psi^N_0\rangle \tag{2.7}$$

where $a_{\alpha H}(t)$ and $a^\dagger_{\beta H}(t)$ are the particle removal and addition operators of the α and β SP states, respectively in the Heisenberg picture:

$$a_{\alpha H}(t) = e^{\frac{i}{\hbar}\hat{H}t}\ a_\alpha\ e^{-\frac{i}{\hbar}\hat{H}t} \tag{2.8}$$

$$a^\dagger_{\alpha H}(t) = e^{\frac{i}{\hbar}\hat{H}t}\ a^\dagger_\alpha\ e^{-\frac{i}{\hbar}\hat{H}t}. \tag{2.9}$$

$\mathcal{T}$ in Eq. (2.7) is the time-ordering operation for fermion operators with reordering including an extra minus sign. It moves the operator with the earlier time to the right of the operator with the later time:

$$\mathcal{T}[a_{\alpha H}(t)a^\dagger_{\beta H}(t')] = \theta(t-t')a_{\alpha H}(t)a^\dagger_{\beta H}(t') - \theta(t'-t)a^\dagger_{\beta H}(t')a_{\alpha H}(t), \tag{2.10}$$

where $\theta(x)$ is the step function which is zero for $x < 0$ and $+1$ for $x > 0$. Using the time-ordering expansion Eq. (2.10) and the Heisenberg transformation for creation and annihilation operators, Eq. (2.8), one can rewrite Eq. (2.7) as:

$$\begin{aligned} G(\alpha,\beta;t,t') = &-\frac{i}{\hbar}\theta(t-t')\sum_m e^{\frac{i}{\hbar}(E^N_0 - E^{N+1}_m)(t-t')}\ \langle \Psi^N_0|a_\alpha|\Psi^{N+1}_m\rangle\langle \Psi^{N+1}_m|a^\dagger_\beta|\Psi^N_0\rangle \\ &+\frac{i}{\hbar}\theta(t'-t)\sum_m e^{\frac{i}{\hbar}(E^N_0 - E^{N-1}_m)(t'-t)}\ \langle \Psi^N_0|a^\dagger_\beta|\Psi^{N-1}_m\rangle\langle \Psi^{N-1}_m|a_\alpha|\Psi^N_0\rangle \end{aligned} \tag{2.11}$$

by introducing complete sets of states and corresponding eigevalues of $\hat{H}$ for the $N \pm 1$ systems. There are two contributions in Eq. (2.11). The first term is the so-called "particle" term where first a particle is added to the many-body ground state and it is removed after this state is evolved. The second contribution on the other hand is called a "hole" term as first the particle is removed and the propagation of the "hole" is studied. The states $|\Psi_m^{N+1}\rangle$ and $|\Psi_n^{N-1}\rangle$ are the exact states of the $N+1$ and $N-1$ systems, respectively:

$$\hat{H}|\Psi_m^{N+1}\rangle = E_m^{N+1}|\Psi_m^{N+1}\rangle \tag{2.12}$$

$$\hat{H}|\Psi_n^{N-1}\rangle = E_n^{N-1}|\Psi_n^{N-1}\rangle \tag{2.13}$$

with corresponding eigenvalues E_m^{N+1} and E_n^{N-1}. Equation (2.11) is the t domain representation of the propagator. It turns out that the E domain form of the propagator provides even more physical and practical insight. This is so because it makes the spectrum and the transition amplitudes appear explicitly. It corresponds to the Fourier transform of (2.11):

$$G(\alpha,\beta;E) = \int_{-\infty}^{+\infty} d\tau\; e^{\frac{i}{\hbar}E\,\tau}\; G(\alpha,\beta;\tau) \qquad \tau = t - t'. \tag{2.14}$$

We will employ the integral representation of step function:

$$\theta(\tau) = -\frac{1}{2\pi i}\int \frac{e^{-iE\,\tau/\hbar}}{E+i\epsilon} \qquad \epsilon \to 0. \tag{2.15}$$

We note that the derivative of the step function is the Dirac delta function:

$$\frac{d}{dt}\,\theta(\tau) = \delta(\tau). \tag{2.16}$$

Using Eq. (2.15) the Fourier transform of the Green's function to the E domain yields:

$$\begin{aligned} G(\alpha,\beta;E) &= \sum_m \frac{\langle\Psi_0^N|a_\alpha|\Psi_m^{N+1}\rangle\langle\Psi_m^{N+1}|a_\beta^\dagger|\Psi_0^N\rangle}{E-(E_m^{N+1}-E_0^N)+i\eta} \\ &+ \sum_n \frac{\langle\Psi_0^N|a_\beta^\dagger|\Psi_n^{N-1}\rangle\langle\Psi_n^{N-1}|a_\alpha|\Psi_0^N\rangle}{E-(E_0^N-E_n^{N-1})-i\eta}, \end{aligned} \tag{2.17}$$

where the completeness relation for the $N\pm1$ system is used. Equation (2.17) is referred to as the Lehmann representation [10, 11]. The $\pm i\eta$ term comes from the Fourier transform of the step function and its existence is necessary to ensure the convergence of the integral over $t-t'$. The $+i\eta$ term in the denominator of the first term in Eq. (2.17) is a consequence of the condition that $t>t'$, *i.e.* the particle travels forward in time. Similarly, the $(-i\eta)$ term is a consequence of the condition $t<t'$, which can be interpreted to mean that a particle travels backward in time. For the case of a finite nucleus, it is convenient to define the hole Fermi energy ε_F^- and the particle Fermi energy ε_F^+ :

$$\varepsilon_F^- = E_0^N - E_0^{N-1} \tag{2.18}$$

$$\varepsilon_F^+ = E_0^{N+1} - E_0^N. \tag{2.19}$$

The former corresponds to the energy required to remove a particle from the N system and leaving the $N-1$ system in its ground state, while the latter corresponds to the binding energy associated with adding a particle to the N system and leaving the $N+1$ system in its ground state. The average Fermi energy ε_F is defined by

$$\varepsilon_F = \frac{1}{2}[\varepsilon_F^+ + \varepsilon_F^-]. \tag{2.20}$$

We note that the poles of G as a function of E correspond to the exact excitation energies of the interacting system. In the IPM only a single state connects to the ground state by

either particle addition or removal (in the appropriate SP basis). On the contrary in the interacting system many states can connect to the ground-state of the $N \pm 1$ system by particle addition or removal [12]. It is also clear that the Green's function G is not analytic in upper and lower E-plane. Although the above form is giving a better physical insight as to its contents related to experimental quantities, to evaluate the propagator theoretically we need to apply perturbation theory. We note that the one-body density matrix $n_{\alpha\beta}$ can be obtained from the SP propagator using the Lehmann representation

$$\begin{aligned} n_{\alpha\beta} &= \frac{1}{2\pi i}\int dE e^{iE\eta}\sum_n \frac{\langle\Psi_0^N|a_\alpha^\dagger|\Psi_n^{N-1}\rangle\langle\Psi_n^{N-1}|a_\beta|\Psi_0^N\rangle}{E-(E_0^N-E_n^{N-1})-i\eta} \\ &= \sum_n \langle\Psi_0^N|a_\alpha^\dagger|\Psi_n^{N-1}\rangle\langle\Psi_n^{N-1}|a_\beta|\Psi_0^N\rangle = \langle\Psi_0^N|a_\alpha^\dagger a_\beta|\Psi_0^N\rangle \end{aligned} \tag{2.21}$$

and the expectation value of any one-body operator in the ground state:

$$\langle\Psi_0^N|\hat{O}|\Psi_0^N\rangle = \sum_{\alpha,\beta}\langle\alpha|O|\beta\rangle = \langle\Psi_0^N|a_\alpha^\dagger a_\beta|\Psi_0^N\rangle = \sum_{\alpha\beta}\langle\alpha|O|\beta\rangle\ n_{\alpha\beta} \tag{2.22}$$

can therefore be calculated. An example is provided by the charge density of a nucleus.

2.3 Perturbation expansion

The Lehmann representation is derived by using fundamental quantum mechanical principles. Although it gives us a useful physical insight, in practice we have to calculate G by using perturbation theory for example in order to solve non-trivial many-body problems. Wick's theorem provides a practical way to evaluate the terms in the perturbation expansion of the full propagator. G can then be expressed in terms of the non-interacting propagator G^0 and the two-body interaction V. The procedure employs the Interaction picture instead of the Heisenberg picture. For an arbitrary operator $\hat{O}$ the time dependence in the Interaction

picture is given by:

$$O_I(t) = e^{i\hat{H}_0 t/\hbar} O e^{-i\hat{H}_0 t/\hbar}. \tag{2.23}$$

Normally the full Hamiltonian H is written as:

$$\hat{H} = \hat{H}_0 + \hat{H}_1 \tag{2.24}$$

with the non-interacting Hamiltonian $\hat{H}_0 = \hat{T} + \hat{U}$. Here $\hat{H}_1 = \hat{V} - \hat{U}$ is the residual interaction and $\hat{U}$ is a possible one-body auxiliary potential. The unperturbed propagator is given by

$$G^0(\alpha, \beta; t - t') = -\frac{i}{\hbar}\langle \Phi_0^A | \mathcal{T}[a_{\alpha I}(t) a^\dagger_{\beta I}(t')] | \Phi_0^A \rangle \tag{2.25}$$

where Φ_0^A is the ground-state associated with H_0. Starting from the time-dependent Schrödinger equation, one can show that the exact propagator is given by [10]

$$\begin{aligned} G(\alpha, \beta; t - t') &= -\frac{i}{\hbar} \sum_n^\infty \left(\frac{i}{\hbar}\right)^n \frac{1}{n!} \int dt_1 ... \int dt_n \\ &\times \langle \Phi_0^A | \mathcal{T}\left[\hat{H}_1(t_1) ... \hat{H}_1(t_n) a_\alpha(t) a^\dagger_\beta(t)\right] | \Phi_0^A \rangle_{\text{connected}}. \end{aligned} \tag{2.26}$$

The subscript "connected" indicates that only connected Feynman diagrams should be included in the calculations. All the operators are in the Interaction picture and Wick's theorem can be used to evaluate all terms in Eq. (2.26) [10]. The zeroth-order term, $n = 0$, is just the non-interacting propagator. In the Feynman diagram language a dashed line represents the interaction $\hat{V}$. Figure 2.1 shows examples of low-order diagram contributions to the propagator. Figure 2.1a represents the Hartree-Fock (HF) approximation if summed to all orders and calculated with a HF propagator in the loop. The HF method therefore includes a self-consistent treatment of the internal loop and leads to a self-energy that does not depend on the energy. The diagram in Fig. 2.1b represents the coupling of a particle to

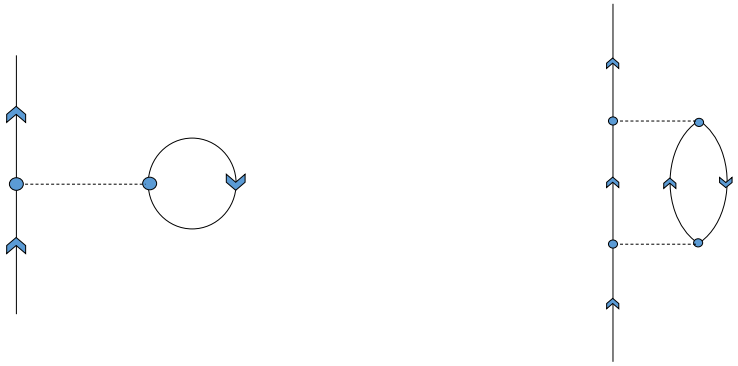

(a) Example of a first-order diagram. (b) Example of a second-order diagram.

Figure 2.1: Some lowest order contributions to the propagator in the perturbation expansion.

either two-particle-one-hole states (2p1h) or two-hole-one-particle states (2h1p) which leads to an energy dependent self-energy.

2.4 Dyson Equation

The Dyson equation is a particularly compact form for the exact propagator which summarizes the Feynman-Dyson perturbation theory. Classifying different contributions of arbitrary Feynman diagrams yields Dyson's equation. Graphical analysis makes it clear that the full propagator can be written in terms of the contribution of the free propagator plus a term which connects the free and full propagator with a self-energy contribution which contains all connected diagrams, as shown in Fig. 2.2 (see Refs. [10] and [12]). The bubble represents the self-energy contribution and consists of all connected diagrams which cannot be cut in to two separate parts by cutting a non-interacting SP propagator. This self-energy is called the *proper* or *irreducible* self-energy Σ^*. One can think of the dressed propagator as representing a particle being influenced by its average interaction with the nucleons in the system which will depend on the energy with which it propagates. In practice only approximations can be made in theoretical calculations that start from the interaction. The mathematical form of

Fig. 2.2 or the Dyson equation can be expressed as:

$$G(\alpha,\beta;E) = G^0(\alpha,\beta;E) + \sum_{\gamma,\delta} G^0(\alpha,\gamma;E)\ \Sigma^*(\gamma,\delta,E)\ G(\delta,\beta;E). \tag{2.27}$$

The double line in Fig. 2.2 represents the dressed propagator and the single line the non-interacting one. To start using the Dyson equation a certain approximation for the self-energy is required by including certain diagrams. Inserting this self-energy into the Eq. (2.27) yields the corresponding Green's function. The power of Dyson's equation is that for an approximation for Σ^* that fulfills the dispersion relation, an infinite-order approximation for the propagator is generated. So Dyson's equation makes it possible to sum an infinite class of perturbation diagrams in a compact form. The solution of the Dyson equation generates all discrete poles corresponding to bound $N \pm 1$ states explicitly given by Eq. (2.17). In addition relevant continuum solutions are generated for example describing elastic scattering of nucleons from the target nucleus represented by its ground-state.

In the DOM formalism the self-energy is parametrized and the parameters are constrained by fitting to data. The self-energy in general is a complex quantity. It is nonlocal and has an energy dependence as well [10]. Schematically it can be written as:

$$\Sigma^*(\alpha,\beta;E) = -i\int \frac{dE'}{2\pi} \sum_{\gamma\delta} \langle\alpha\gamma|V|\beta\gamma\rangle G(\gamma,\delta;E') + \text{Higher Order terms}(E). \tag{2.28}$$

The first term in Eq. (2.28) contains an integral over energy and therefore does not depend on the energy. This energy independent term is the HF contribution to the irreducible self-energy. It is also referred to as the static contribution Σ_s. The higher-order terms explicitly depend on the energy and represent the dynamic contributions of the self-energy and are denoted by Σ_d. This complex dynamic part of the self-energy explains the absorptive properties of the many-body system and is required to be negative at least in the domain of

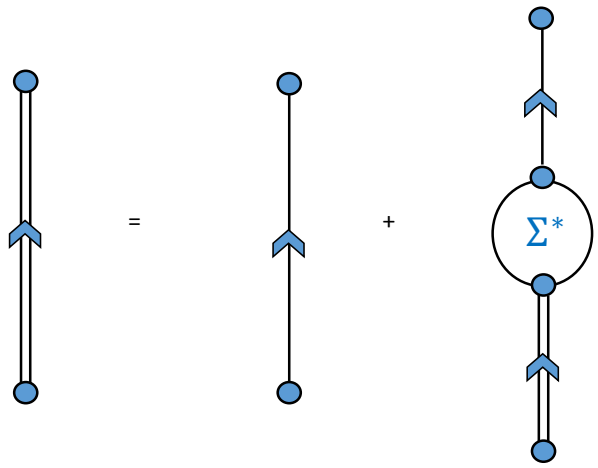

Figure 2.2: Graphical representation of the Dyson equation for the dressed SP propagator in terms of the noninteracting one and the irreducible self-energy.

coupling to the excitations in the $N+1$ system. It leads to a loss of flux from the elastic channel in that domain and the removal of SP strength from below the Fermi energy to that domain. On the other hand it is positive for the coupling to the $N-1$ system excitations [10]. The real and imaginary part of the complex function Σ_d are related through the dispersion relation since Σ_d is an analytic complex function

$$\mathfrak{Re}\ \Sigma_d(\alpha,\beta;E) = -\mathcal{P}\int_{\varepsilon_T^+}^{\infty}\frac{dE'}{\pi}\frac{\mathfrak{Im}\Sigma_d(\alpha,\beta;E')}{E-E'} + \mathcal{P}\int_{-\infty}^{\varepsilon_T^-}\frac{dE'}{\pi}\frac{\mathfrak{Im}\Sigma_d(\alpha,\beta;E')}{E-E'}, \tag{2.29}$$

where $\mathcal{P}$ represents the principal value and applies when E occurs in the interval of integration. The dynamic parts start and end at corresponding thresholds in the $N\pm1$ systems that have a larger separation than the corresponding difference between the Fermi energies for addition and removal of a particle, given by Eqs. (2.18) and (2.19). This feature is particular to a finite system and generates possibly several discrete quasi-particle and hole-like solutions of the Dyson equation in the domain where the imaginary part of the self-energy vanishes. With Eq. (2.29), the total real part of the irreducible self-energy can be written

as

$$\mathfrak{Re}\ \Sigma^*(\alpha,\beta;E) = \Sigma_s(\alpha,\beta) + \mathfrak{Re}\ \Sigma_d(\alpha,\beta;E). \tag{2.30}$$

In some cases it is useful to write the above equation in terms of some reference energy like $E = E_0$. If we choose E_0 to be Fermi energy ε_F we have:

$$\begin{aligned}\mathfrak{Re}\ \Sigma(\alpha,\beta;E) = \Sigma_s(\alpha,\beta) &- \mathcal{P}\int_{\varepsilon_T^+}^{\infty}\frac{dE'}{\pi}\frac{\mathfrak{Im}\Sigma(\alpha,\beta;E')}{E-E'} \\ &+\mathcal{P}\int_{-\infty}^{\varepsilon_T^-}\frac{dE'}{\pi}\frac{\mathfrak{Im}\Sigma(\alpha,\beta;E')}{E-E'}\end{aligned} \tag{2.31}$$

$$\begin{aligned}\mathfrak{Re}\ \Sigma(\alpha,\beta;\varepsilon_F) = \Sigma_s(\alpha,\beta) &- \mathcal{P}\int_{\varepsilon_T^+}^{\infty}\frac{dE'}{\pi}\frac{\mathfrak{Im}\Sigma(\alpha,\beta;E')}{\varepsilon_F-E'} \\ &+\mathcal{P}\int_{-\infty}^{\varepsilon_T^-}\frac{dE'}{\pi}\frac{\mathfrak{Im}\Sigma(\alpha,\beta;E')}{\varepsilon_F-E'}.\end{aligned} \tag{2.32}$$

Subtracting Eq. (2.32) from Eq. (2.31) we find:

$$\begin{aligned}\mathfrak{Re}\ \Sigma(\alpha,\beta;E) &= \mathfrak{Re}\ \Sigma(\alpha,\beta;\varepsilon_F) - \mathcal{P}\int_{\varepsilon_T^+}^{\infty}\frac{dE'}{\pi}\mathfrak{Im}\Sigma(\alpha,\beta;E')\left[\frac{1}{E-E'}-\frac{1}{\varepsilon_F-E'}\right] \\ &- \mathcal{P}\int_{-\infty}^{\varepsilon_T^-}\frac{dE'}{\pi}\mathfrak{Im}\Sigma(\alpha,\beta;E')\left[\frac{1}{E-E'}-\frac{1}{\varepsilon_F-E'}\right].\end{aligned} \tag{2.33}$$

This form of the dispersion relation is known as the subtracted dispersion relation, and it is in this form that it is used in the DOM.

2.5 Titchmarsh's theorem

The Titchmarsh theorem establishes a connection between the properties of an analytic function in the complex plane and causality. Consider a function u can be expressed as:

$$u(E) = \frac{1}{\pi}\mathcal{P}\int_{-\infty}^{+\infty} dE' \, \frac{v(E')}{E - E'}. \tag{2.34}$$

This implies that:

$$v(E) = -\frac{1}{\pi}\mathcal{P}\int_{-\infty}^{+\infty} dE' \, \frac{u(E')}{E - E'}. \tag{2.35}$$

Equations (2.34) and (2.35) are the (inverse) Hilbert transforms and the result can be proved by employing the properties of analytic functions in the complex plane. If the functions u and v are both square integrable on the real axis then Titchmarsh's theorem states that if each of the following properties will automatically satisfy the other two:

First

The function $w(E) = u(E) + iv(E)$ is analytic for $E > 0$ in the complex plane and the quantity

$$\int_{-\infty}^{+\infty} |w(z)|^2 dx \quad z = x + i\, y \tag{2.36}$$

is uniformly bound for all positive values of y.

Second

The functions u and v be the Hilbert transform of each other:

$$u(E) = \frac{1}{\pi}\mathcal{P}\int_{-\infty}^{+\infty} dE' \, \frac{v(E')}{E - E'} \qquad v(E) = -\frac{1}{\pi}\mathcal{P}\int_{-\infty}^{+\infty} dE' \, \frac{u(E')}{E - E'}. \tag{2.37}$$

Third

The Fourier transform

$$\omega(t) = \frac{1}{2\pi} \int_{-\infty}^{+\infty} dE\ w(E)\ e^{-iEt} \tag{2.38}$$

vanishes for negative t values. This property is called the "causal" property of functions. Consequently one can write:

$$\omega(t) = \Theta(t)\mathcal{G}(t) \tag{2.39}$$

where $\Theta(t)$ is the step function. The function $\mathcal{G}$ is also defined in Eq. (2.39). The Titchmarsh theorem provides more physical insight to the dispersion relationship, analyticity and causality [13].

2.6 Propagator in r-space

Mostly due to the presence of the Coulomb potential, the DOM potential is presented in coordinate space. The corresponding integral-differential equation is then also solved in r-space for positive energy by matching the interior wave functions with asymptotic solutions. Then the S matrix and phase-shifts are calculated using the latter solutions of the Schrödinger equation. Writing down the equations allows to visualize how the actual problem is solved numerically. In a basis with good radial position r, orbital angular momentum (parity), and total angular momentum j, the sum in Eq. (2.27) becomes an integral and the Dyson equation takes on the following form

$$G_{\ell j}(r, r'; E) = G^0_{\ell j}(r, r'; E) + \int dx x^2 \int y^2 dy G^0_{\ell j}(r, x; E)\Sigma^*_{\ell j}(x, y, ; E)G_{\ell j}(y, r'; E). \tag{2.40}$$

The isospin and the projection of total angular momentum quantum numbers have been suppressed. Beginning with the Dyson equation, one can show that for discrete states the overlap function obeys a Schrödinger-like equation [10]. Introducing the notation

$$\psi^n_{\ell j}(r) = \langle \Psi^{A-1}_n | a_{r\ell j} | \Psi^A_0 \rangle \tag{2.41}$$

the overlap function for the removal of a nucleon at r with discrete quantum numbers n, ℓ and j will be obtained solving:

$$\left(\frac{p_r^2}{2m} + \frac{\hbar^2 \ell(\ell+1)}{2mr^2} \right) \psi^n_{\ell j}(r) + \int dr' r'^2 \Sigma^*_{\ell j}(r, r'; \varepsilon^-_n) \psi^n_{\ell j}(r') = \varepsilon^-_n \psi^n_{\ell j}(r). \tag{2.42}$$

In coordinate space the radial momentum operator is given by $p_r = -i\hbar(\frac{\partial}{\partial r} + \frac{1}{r})$. Equation (2.42) is employed for discrete states in the $N-1$ system. The solutions exist where the imaginary part of the self-energy vanishes. By using the inhomogeneous term in the Dyson equation, the solutions of the Schrödinger-like equation (2.42) are called the "quasihole" states and are labeled by α_{qh}. The normalization or the spectroscopic factor of these states is given by Ref. [10] and reads:

$$S^n_{\ell j} = \left(1 - \frac{\partial}{\partial E} \Sigma^*_{\ell j}(\alpha_{qh}, \alpha_{qh}; E) \Big|_{\varepsilon^-_n} \right)^{-1}. \tag{2.43}$$

For continuum energies the spectral density can be obtained from Eq. (2.40) as follows:

$$S^{\ell j}_h(r, r'; E) = \frac{1}{\pi} \mathfrak{Im} G_{\ell j}(r, r'; E), \tag{2.44}$$

after G is obtained from a complex matrix inversion. For positive energy Eq. (2.42) is solved using the iterative method outlined in Ref. [14]. At these energies we incorporate relativistic effects in lowest order following Ref. [15] as was also utilized in earlier local DOM

calculations [16].

2.7 Reducible Self-Energy and the R-matrix

In this section we develop the formalism necessary to generate the spectral density at positive energy. This is most easily accomplished by studying the solution of the Dyson equation in momentum space in terms of reducible self-energies. The reducible self-energy satisfies the corresponding Dyson equation:

$$\Sigma = \Sigma^* + \Sigma^* G^0 \Sigma \tag{2.45}$$

where Σ^* is the irreducible self-energy (or optical potential). Explicitly, in momentum space but supressing spin degree of freedom:

$$\Sigma(\boldsymbol{k}, \boldsymbol{k}', E) = \Sigma^*(\boldsymbol{k}, \boldsymbol{k}', E) + \int \mathrm{d}\boldsymbol{q}\, \Sigma^*(\boldsymbol{k}, \boldsymbol{q}, E)\, G^0(\boldsymbol{q}, E)\, \Sigma(\boldsymbol{q}, \boldsymbol{k}', E) \tag{2.46}$$

where G^0 is:

$$G^0(k, E) = \frac{1}{E - \varepsilon_k \pm i\eta} = \frac{\mathcal{P}}{E - \varepsilon_k} \mp i\pi\delta(E - \varepsilon_k). \tag{2.47}$$

If the irreducible self-energy has spherical symmetry, we can integrate the angular degrees of freedom, hence write the Dyson equation in partial waves including a coupling to total SP angular momentum:

$$\Sigma_{\ell j}(k, k', E) = \Sigma^*_{\ell j}(k, k', E) + \int q^2 \mathrm{d}q\, \Sigma^*_{\ell j}(k, q, E)\, G^0(q, E)\, \Sigma_{\ell j}(q, k' E). \tag{2.48}$$

The full propagator can also obtained from the Dyson equation in the following form [10]:

$$G_{\ell j}(k, k'; E) = \frac{\delta(k - k')}{k^2} G^{(0)}(k; E) + G^0(k; E) \Sigma_{\ell j}(k, k'; E) G^0(k; E). \tag{2.49}$$

The on-shell matrix elements of the reducible self-energy in Eq. (2.48) are sufficient to describe all aspects of nucleon elastic scattering like differential, reaction, and total cross sections as well as polarization data [17]. We separately write the Dyson equation above or below the real axis, according to:

$$\begin{aligned}\Sigma_{\ell j}(k,k';E+i\eta) &= \Sigma^{*}_{\ell j}(k,k';E+i\eta) \\ &+ \mathcal{P}\int q^2\mathrm{d}q\ \Sigma^{*}_{\ell j}(k,q;E+i\eta)\frac{1}{E-\varepsilon_q}\Sigma^{\ell j}(q,k';E+i\eta) \\ &- i\pi\mu k_0\ \Sigma^{*}_{\ell j}(k,k_0;E+i\eta)\ \Sigma_{\ell j}(k_0,k',E+i\eta)\end{aligned} \tag{2.50}$$

and

$$\begin{aligned}\Sigma_{\ell j}(k,k';E-i\eta) &= \Sigma^{*}_{\ell j}(k,k';E-i\eta) \\ &+ \mathcal{P}\int q^2\mathrm{d}q\ \Sigma^{*}_{\ell j}(k,q;E-i\eta)\frac{1}{E-\varepsilon_q}\Sigma^{\ell j}(q,k';E-i\eta) \\ &- i\pi\mu k_0\ \Sigma^{*}_{\ell j}(k,k_0;E-i\eta)\ \Sigma_{\ell j}(k_0,k',E-i\eta)\end{aligned} \tag{2.51}$$

where $k_0=\sqrt{2\mu E}$ will represent the implied dependence on the energy E. Due to causality (or analyticity) the irreducible self-energy satisfies the dispersion relations:

$$\begin{aligned}\mathfrak{Re}(\Sigma^{*}(E+i\eta)) &= -\frac{1}{\pi}\mathcal{P}\int_{-\infty}^{\infty}\mathrm{d}\omega\frac{\mathfrak{Im}(\Sigma^{*}(\omega))}{E-\omega} \\ \mathfrak{Im}(\Sigma^{*}(E+i\eta)) &= \frac{1}{\pi}\mathcal{P}\int_{-\infty}^{\infty}\mathrm{d}\omega\frac{\mathfrak{Re}(\Sigma^{*}(\omega))}{E-\omega}\end{aligned}$$

and

$$\begin{aligned}\mathfrak{Re}(\Sigma^{*}(E-i\eta)) &= \frac{1}{\pi}\mathcal{P}\int_{-\infty}^{\infty}\mathrm{d}\omega\frac{\mathfrak{Im}(\Sigma^{*}(\omega))}{E-\omega} \\ \mathfrak{Im}(\Sigma^{*}(E-i\eta)) &= -\frac{1}{\pi}\mathcal{P}\int_{-\infty}^{\infty}\mathrm{d}\omega\frac{\mathfrak{Re}(\Sigma^{*}(\omega))}{E-\omega}.\end{aligned}$$

In addition if the real part of Σ^* is the same below and above the real axes, then:

$$\mathfrak{Im}(\Sigma^*(E+i\eta)) = -\mathfrak{Im}(\Sigma^*(E-i\eta)). \tag{2.52}$$

In order to solve the integral equation for the reducible self-energy, it is usual to define an auxiliary matrix R called the reaction matrix (or R-matrix) which satisfies:

$$\begin{aligned} R_{\ell j}(k,k';E\pm i\eta) &= \Sigma^*_{\ell j}(k,k',E\pm i\eta) \\ &+ \mathcal{P}\int q^2\mathrm{d}q\ \Sigma^*_{\ell j}(k,q;E\pm i\eta)\ \frac{1}{E-\varepsilon_q}\ R_{\ell j}(q,k';E\pm i\eta). \end{aligned} \tag{2.53}$$

We rewrite this equation as :

$$\begin{aligned} \Sigma^*_{\ell j}(k,k',E\pm i\eta) &= R_{\ell j}(k,k';E\pm i\eta) \\ &- \mathcal{P}\int q^2\mathrm{d}q\ \Sigma^*_{\ell j}(k,q;E\pm i\eta)\ \frac{1}{E-\varepsilon_q}\ R_{\ell j}(q,k';E\pm i\eta). \end{aligned} \tag{2.54}$$

Here we note that the reaction matrix is different below and above the real axis because of the difference in sign, (2.52), of the imaginary part of the potential Σ^*. When the potential is not absorptive, the R-matrix integrated either above or below the real axes is the same. Equation (2.54) can be considered as :

$$\Sigma^* = \mathcal{A}R \tag{2.55}$$

where $\mathcal{A}$ is the integral operator acting on R, and the integral equation has the formal solution:

$$R = \mathcal{A}^{-1}\Sigma^* \tag{2.56}$$

provided $\mathcal{A}^{-1}$ exists. If we now compare the integral equation for R with the one that Σ satisfies we notice that schematically :

$$\mathcal{A}\Sigma = \Sigma^* \mp i\pi\mu k_0 \Sigma^*\Sigma$$

and if we multiply both sides by $\mathcal{A}^{-1}$ we find:

$$\Sigma = \left(\mathcal{A}^{-1}\Sigma^*\right) \mp i\pi\mu k_0 \left(\mathcal{A}^{-1}\Sigma^*\right)\Sigma \tag{2.57}$$

or in terms of the reaction matrix:

$$\Sigma = R \mp i\pi\mu k_0 R\Sigma. \tag{2.58}$$

More explicitly we can write:

$$\Sigma_{\ell j}(k,k';E+i\eta) = R_{\ell j}(k,k';E+i\eta) - i\pi\mu k_0 R_{\ell j}(k,k_0;E+i\eta)\Sigma_{\ell j}(k_0,k';E+i\eta) \tag{2.59}$$

$$\Sigma_{\ell j}(k,k';E-i\eta) = R_{\ell j}(k,k';E-i\eta) - i\pi\mu k_0 R_{\ell j}(k,k_0;E-i\eta)\Sigma_{\ell j}(k_0,k';E-i\eta) \tag{2.60}$$

whose solutions are:

$$\Sigma_{\ell j}(k,k';E+i\eta) = R_{\ell j}(k,k';E+i\eta) - i\pi\mu k_0 \frac{R_{\ell j}(k,k_0;E+i\eta)R_{\ell j}(k_0,k';E+i\eta)}{1+i\pi\mu k_0 R_{\ell j}(k_0,k_0;E+i\eta)} \tag{2.61}$$

$$\Sigma_{\ell j}(k,k';E-i\eta) = R_{\ell j}(k,k';E-i\eta) + i\pi\mu k_0 \frac{R_{\ell j}(k,k_0;E-i\eta)R_{\ell j}(k_0,k';E-i\eta)}{1-i\pi\mu k_0 R_{\ell j}(k_0,k_0;E-i\eta)}. \tag{2.62}$$

The reducible self-energy is the equivalent to the transition matrix in scattering theory. The

scattering amplitude is given in terms of the on-shell elements of Σ:

$$\mathcal{S}_{\ell j}(E) = 1 - 2i\pi\mu k_0 \, \Sigma_{\ell j}(k_0, k_0; E + i\eta) \tag{2.63}$$

from where we can find all the observables, the differential cross section, analyzing power and spin rotation of the scattering in the nucleon-nucleus collision.

2.8 Spectral functions

Spectral functions tell us about the SP strength distribution of nucleons. There is a probability of finding a particle with a specific ℓj at a position in r-space at a specific energy (it can be any space, such as momentum space; it does not need to be just position space). After obtaining the propagator it is straightforward to find the spectral functions below the Fermi energy. For positive energies it is not very straightforward and requires some special considerations. A beautiful aspect of these calculations generating the spectral functions is that they satisfy an important sum rule. It is also a very practical test for our method and calculations. This section is mostly devoted to the method which is used to obtain the particle spectral functions.

The formal definition of the spectral function is given by:

$$S_{\ell j}(k, k'; E) = \frac{i}{2\pi} \left[G_{\ell j}(k, k'; E + i\eta) - G_{\ell j}(k, k'; E - i\eta) \right]. \tag{2.64}$$

Explicitly we require the evaluation of the difference in parenthesis between the retarded and advanced propagators. The full propagator has the following form [10]:

$$G_{\ell j}(k, k'; E) = \frac{\delta(k - k')}{k^2} G^0_{\ell j}(k; E) + G^0_{\ell j}(k; E) \Sigma_{\ell j}(k, k'; E) G^0_{\ell j}(k; E). \tag{2.65}$$

We first define the free spectral function by:

$$S^0_{\ell j}(k,k';E) = \frac{i}{2\pi}\left[G^0_{\ell j}(k,k';E+i\eta) - G^0_{\ell j}(k,k';E-i\eta)\right]. \tag{2.66}$$

The free propagator here is given by:

$$G^0_{\ell j}(k,k',;E^{\pm}) = \frac{\delta(k-k')}{k^2}\frac{1}{E-\varepsilon_k \pm i\eta}. \tag{2.67}$$

We therefore find explicitly:

$$\begin{aligned} S^0_{\ell j}(k,k';E) &= \frac{i}{2\pi}\frac{\delta(k-k')}{k^2}\left[\left(\frac{\mathcal{P}}{E-\varepsilon_k} - i\pi\delta(E-\varepsilon_k)\right) - \left(\frac{\mathcal{P}}{E-\varepsilon_k} + i\pi\delta(E-\varepsilon_k)\right)\right] \\ &= \frac{i}{2\pi}\left(-2i\pi\delta(E-\varepsilon_k)\frac{\delta(k-k')}{k^2}\right) \\ &= \delta(E-\varepsilon_k)\frac{\delta(k-k')}{k^2}. \end{aligned} \tag{2.68}$$

Now we calculate the full spectral function in Eq. (2.64). Using the definition for the free propagator, the full propagator can be written as:

$$\begin{aligned} G_{\ell j}(k,k';E\pm i\eta) &= \frac{\delta(k-k')}{k^2}\frac{1}{E-\varepsilon_k \pm i\eta} \\ &+ \frac{1}{E-\varepsilon_k \pm i\eta}\Sigma^{\pm}_{\ell j}(k,k';E)\frac{1}{E-\varepsilon_{k'} \pm i\eta}. \end{aligned} \tag{2.69}$$

Here the energy $\varepsilon_k = k^2/(2\mu)$. The correlated terms in Eq. (2.69) for $E+i\eta$ can be written

as:

$$\begin{aligned}
&\frac{1}{E-\varepsilon_k+i\eta}\Sigma_{\ell j}(k,k';E+i\eta)\frac{1}{E-\varepsilon_{k'}+i\eta}\\
=&\left(\frac{\mathcal{P}}{E-\varepsilon_k}-i\pi\delta(E-\varepsilon_k)\right)\times\Sigma_{\ell j}(k,k';E+i\eta)\times\left(\frac{\mathcal{P}}{E-\varepsilon_{k'}}-i\pi\delta(E-\varepsilon_{k'})\right)\\
=&\frac{\mathcal{P}}{E-\varepsilon_k}\Sigma_{\ell j}(k,k';E+i\eta)\frac{\mathcal{P}}{E-\varepsilon_{k'}}-i\pi\delta(E-\varepsilon_k)\Sigma_{\ell j}(k,k';E+i\eta)\frac{\mathcal{P}}{E-\varepsilon_{k'}}\\
+&\frac{\mathcal{P}}{E-\varepsilon_k}\Sigma_{\ell j}(k,k';E+i\eta)(-i\pi)\delta(E-\varepsilon_{k'})\\
+&(-i\pi)\delta(E-\varepsilon_k)\Sigma_{\ell j}(k,k';E+i\eta)(-i\pi)\delta(E-\varepsilon_{k'}).
\end{aligned}\tag{2.70}$$

Similarly, for the $E-i\eta$ we find:

$$\begin{aligned}
&\frac{1}{E-\varepsilon_k-i\eta}\Sigma_{\ell j}(k,k';E-i\eta)\frac{1}{E-\varepsilon_{k'}-i\eta}\\
&\qquad=\frac{\mathcal{P}}{E-\varepsilon_k}\Sigma_{\ell j}(k,k';E-i\eta)\frac{\mathcal{P}}{E-\varepsilon_{k'}} &(2.71)\\
&\qquad+\pi\delta(E-\varepsilon_k)\Sigma_{\ell j}(k,k';E-i\eta)\frac{\mathcal{P}}{E-\varepsilon_{k'}}\\
&\qquad+\frac{\mathcal{P}}{E-\varepsilon_k}\Sigma_{\ell j}(k,k';E-i\eta)(i\pi)\delta(E-\varepsilon_{k'})\\
&\qquad+\pi\delta(E-\varepsilon_k)\Sigma_{\ell j}(k,k';E+i\eta)(i\pi)\delta(E-\varepsilon_{k'}) &(2.72)
\end{aligned}$$

then carry the difference in Eq. (2.64) and find:

$$\begin{aligned}
S_{\ell j}(k,k';E)=&S^0_{\ell j}(k,k';E)+\\
&\frac{i}{2\pi}\Bigg\{\frac{\mathcal{P}}{E-\varepsilon_k}\left[\Sigma_{\ell j}(k,k',E+i\eta)-\Sigma_{\ell j}(k,k',E-i\eta)\right]\frac{\mathcal{P}}{E-\varepsilon_{k'}}\\
&-i\pi\delta(E-\varepsilon_k)\left[\Sigma_{\ell j}(k,k',E+i\eta)+\Sigma_{\ell j}(k,k',E-i\eta)\right]\frac{\mathcal{P}}{E-\varepsilon_{k'}}\\
&-\frac{\mathcal{P}}{E-\varepsilon_k}\left[\Sigma_{\ell j}(k,k',E+i\eta)+\Sigma_{\ell j}(k,k',E-i\eta)\right]i\pi\delta(E-\varepsilon_{k'})\\
&+i\pi\delta(E-\varepsilon_k)\left[\Sigma_{\ell j}(k,k',E+i\eta)-\Sigma_{\ell j}(k,k',E-i\eta)\right]i\pi\delta(E-\varepsilon_{k'})\Bigg\}.
\end{aligned}\tag{2.73}$$

2.8.1 Hole Spectral Function

For below the Fermi energy it is much easier to calculate the spectral function. Once we have obtained the propagator the hole spectral function will be given by:

$$S^h_{\ell j}(r;E) = \frac{1}{\pi}\mathfrak{Im}\left[G_{\ell j}(r,r;E)\right]. \tag{2.74}$$

The occupation number of a bound orbit is given by an integral over a corresponding folding of the hole spectral density

$$S^{n-}_{\ell j}(E) = \int dr r^2 \int dr' r'^2 \phi^{n-}_{\ell j}(r) S^h_{\ell j}(r,r';E)\phi^{n-}_{\ell j}(r'), \tag{2.75}$$

where $S^h_{\ell j}(r,r';E)$ provides equivalent information below the Fermi energy as $S^p_{\ell j}(r,r';E)$ above.

2.8.2 Particle spectral function

The spectral representation of the particle part of the propagator, referring to the $N+1$ system, appropriate for a treatment of the continuum and possible open channels is given by [2]

$$G^p_{\ell j}(k,k';E) = \sum_n \frac{\phi^{n+}_{\ell j}(k)\left[\phi^{n+}_{\ell j}(k')\right]^*}{E - E^{*N+1}_n + i\eta} + \sum_c \int_{T_c}^{\infty} dE' \, \frac{\chi^{cE'}_{\ell j}(k)\left[\chi^{cE'}_{\ell j}(k')\right]^*}{E - E' + i\eta}. \tag{2.76}$$

Overlap functions for bound $N+1$ states are given by $\phi^{n+}_{\ell j}(k) = \langle \Psi^N_0 | a_{k\ell j} | \Psi^{N+1}_n \rangle$, whereas those in the continuum are given by $\chi^{cE}_{\ell j}(k) = \langle \Psi^N_0 | a_{k\ell j} | \Psi^{N+1}_{cE} \rangle$ indicating the relevant channel by c and the energy by E. Excitation energies in the $N+1$ system are with respect to the N-body ground state $E^{*N+1}_n = E^{N+1}_n - E^N_0$. Each channel c has an appropriate threshold

indicated by T_c which is the experimental threshold with respect to the ground-state energy of the N-body system. The overlap function for the elastic channel can be explicitly calculated by solving the Dyson equation while it is also possible to obtain the complete spectral density for $E > 0$

$$S^p_{\ell j}(k,k';E) = \sum_c \chi^{cE}_{\ell j}(k) \left[\chi^{cE}_{\ell j}(k')\right]^* . \tag{2.77}$$

Unlike the hole spectral function, to find the spectral function for particle states, in practice, this requires solving the scattering problem twice at each energy so that one may employ

$$S^p_{\ell j}(k,k';E) = \frac{i}{2\pi}\left[G^p_{\ell j}(k,k';E^+) - G^p_{\ell j}(k,k';E^-)\right] \tag{2.78}$$

with $E^\pm = E \pm i\eta$, and only the elastic-channel contribution to Eq. (2.77) is explicitly known. Equivalent expressions pertain to the hole part of the propagator $G^h_{\ell j}$ [2].

The calculations are performed in momentum space according to Eq. (2.48) to generate the off-shell reducible self-energy and thus the spectral density by employing Eqs. (2.65) and (2.78). Because the momentum-space spectral density contains a delta-function associated with the free propagator, it is convenient for visualization purposes to consider a Fourier transform to coordinate space (see Sec. 2.8.3)

$$S^p_{\ell j}(r,r';E) \;=\; \frac{2}{\pi}\int \mathrm{d}k k^2 \int \mathrm{d}k' k'^2 j_\ell(kr) S^p_{\ell j}(k,k';E) j_\ell(k'r'), \tag{2.79}$$

which has the physical interpretation for $r = r'$ as the probability density $S_{\ell j}(r;E)$ for adding a nucleon with energy E at a distance r from the origin for a given ℓj combination. By employing the asymptotic analysis to the propagator in coordinate space following *e.g.* Ref. [10], one may express the elastic-scattering wave function that contributes to Eq. (2.77)

in terms of the half on-shell reducible self-energy obtained according to

$$\chi^{elE}_{\ell j}(r) = \left[\frac{2mk_0}{\pi\hbar^2}\right]^{1/2} \left\{ j_\ell(k_0 r) + \int \mathrm{d}k k^2 j_\ell(kr) G^{(0)}(k;E) \Sigma_{\ell j}(k,k_0;E) \right\}, \tag{2.80}$$

where k_0 is related to the scattering energy in the usual way.

The presence of strength in the continuum associated with mostly-occupied orbits (or mostly empty but $E<0$ orbits) is obtained by double folding the spectral density in Eq. (2.79) in the following way

$$S^{n+}_{\ell j}(E) = \int dr r^2 \int dr' r'^2 \phi^{n-}_{\ell j}(r) S^{p}_{\ell j}(r,r';E) \phi^{n-}_{\ell j}(r'), \tag{2.81}$$

using an overlap function

$$\sqrt{S^{n}_{\ell j}} \phi^{n-}_{\ell j}(r) = \langle \Psi^{N-1}_{n} | a_{r\ell j} | \Psi^{N}_{0} \rangle, \tag{2.82}$$

corresponding to a bound orbit with $S^n_{\ell j}$ the relevant spectroscopic factor and $\phi^{n-}_{\ell j}(r)$ normalized to 1 [17]. The corresponding strength below the Fermi energy is obtained from

$$S^{n-}_{\ell j}(E) = \int dr r^2 \int dr' r'^2 \phi^{n-}_{\ell j}(r) S^{h}_{\ell j}(r,r';E) \phi^{n-}_{\ell j}(r'), \tag{2.83}$$

More specifically the wave functions $\phi^n_{\ell j}(k)$ are the solution of the eigen-value problem:

$$\frac{k^2}{2\mu}\phi^n_{\ell j}(k) + \int k'^2 \mathrm{d}k' \mathfrak{Re}\left(\Sigma_{\ell j}(k,k';\varepsilon)\right) \phi^n_{\ell j}(k') = \varepsilon \phi^n_{\ell j}(k) \tag{2.84}$$

which we solve for the bound states ($\varepsilon<0$) self-consistently. Their normalization condition is:

$$\int k^2 \mathrm{d}k \ \phi^n_{\ell j}(k) \phi^n_{\ell j}(k) = 1. \tag{2.85}$$

Using the free (uncorrelated) contribution to the spectral function, we find:

$$\begin{aligned} S^{n0}_{\ell j}(E) &= \int k^2 \mathrm{d}k \phi^n_{\ell j}(k) \int k'^2 \mathrm{d}k' S^{n0}_{\ell j}(k,k',E) \phi^n_{\ell j}(k') \\ &= \mu k_0 |\phi^n_{\ell j}(k_0)|^2. \end{aligned} \tag{2.86}$$

Integrals involving delta functions can be simplified yielding the following result:

$$\begin{aligned} & S^n_{\ell j}(E) = S^{n0}_{\ell j}(E) \\ + \;& \frac{i}{2\pi} \mathcal{P} \int k^2 \mathrm{d}k \frac{\phi^n_{\ell j}(k)}{E-\varepsilon_k} \mathcal{P} \int k'^2 \mathrm{d}k' \left[\Sigma_{\ell j}(k,k';E+i\eta) - \Sigma_{\ell j}(k,k';E-i\eta) \right] \frac{\phi^n_{\ell j}(k')}{E-\varepsilon_{k'}} \\ + \;& \frac{1}{2} \mu k_0 \phi^n_{\ell j}(k_0) \mathcal{P} \int k^2 \mathrm{d}k \left[\Sigma_{\ell j}(k,k_0;E+i\eta) + \Sigma_{\ell j}(k,k_0;E-i\eta) \right] \frac{\phi^n_{\ell j}(k)}{E-\varepsilon_k} \\ - \;& \frac{1}{2} \mu k_0 \phi^n_{\ell j}(k_0) \mathcal{P} \int k^2 \mathrm{d}k \left[\Sigma_{\ell j}(k_0,k;E+i\eta) + \Sigma_{\ell j}(k_0,k;E-i\eta) \right] \frac{\phi^n_{\ell j}(k)}{E-\varepsilon_k} \\ - \;& i\frac{\pi}{2} \left(\mu k_0\right)^2 |\phi^n_{\ell j}(k_0)|^2 \left[\Sigma_{\ell j}(k_0,k_0;E+i\eta) - \Sigma_{\ell j}(k_0,k_0;E-i\eta) \right]. \end{aligned} \tag{2.87}$$

2.8.3 Fourier-Bessel transformation to position space

To visualise correlations we can transform to position space:

$$S_{\ell j}(r,r';E) = \frac{2}{\pi} \int k^2 \mathrm{d}k j_\ell(kr) \int k'^2 \mathrm{d}k' S_{\ell j}(k,k';E) j_\ell(k'r'). \tag{2.88}$$

Let us transform the free spectral function first:

$$\begin{aligned} S^0_{\ell j}(r,r';E) &= \frac{2}{\pi} \int k^2 \mathrm{d}k j_\ell(kr) \int k'^2 \mathrm{d}k' \delta(E-\varepsilon_k) \frac{\delta(k-k')}{k^2} j_\ell(k'r') \\ &= \frac{2}{\pi} \int k^2 \mathrm{d}k j_\ell(kr) \delta(E-\varepsilon_k) j_\ell(kr') \\ &= \frac{2}{\pi} \mu k_0 j_\ell(k_0 r) j_\ell(k_0 r') \end{aligned} \tag{2.89}$$

here $k_0 = \sqrt{2\mu E}$. Then write:

$$S_{\ell j}(r, r'; E) = S^0_{\ell j}(r\ r'\ E) + \Delta S_{\ell j}(r\ r'\ E). \tag{2.90}$$

To save writing we are putting $2/\pi$ on the other side so that the correlated part ($\times\pi/2$) is:

$$\begin{aligned}
&\frac{\pi}{2}\Delta S_{\ell j}(r\ r'\ E) = \\
&\frac{i}{2\pi}\mathcal{P}\int k^2\mathrm{d}p\frac{j_\ell(kr)}{E-\varepsilon_k}\mathcal{P}\int k'^2\mathrm{d}k'\left(\Sigma_{\ell j}(k,k';E+i\eta)-\Sigma_{\ell j}(k,k';E-i\eta)\right)\frac{j_\ell(k'r')}{E-\varepsilon_{k'}} \\
+\ &\frac{1}{2}\int k^2\mathrm{d}k j_\ell(kr)\delta(E-\varepsilon_k)\mathcal{P}\int k'^2\mathrm{d}k'\left(\Sigma_{\ell j}(k,k';E+i\eta)+\Sigma_{\ell j}(k,k';E-i\eta)\right)\frac{j_\ell(k'r')}{E-\varepsilon_{k'}} \\
+\ &\frac{1}{2}\mathcal{P}\int k^2\mathrm{d}k\frac{j_\ell(kr)}{E-\varepsilon_k}\int k'^2\mathrm{d}k'\left(\Sigma_{\ell j}(k,k';E+i\eta)+\Sigma_{\ell j}(k,k';E-i\eta)\right)\delta(E-\varepsilon_{k'})j_\ell(k'r') \\
-\ &\frac{i\pi}{2}\int k^2\mathrm{d}k j_\ell(kr)\delta(E-\varepsilon_k)\int k'^2\mathrm{d}k'\left(\Sigma_{\ell j}(k,k';E+i\eta)-\Sigma_{\ell j}(k,k';E-i\eta)\right) \\
&\qquad\qquad\times\delta(E-\varepsilon_{k'})j_\ell(k'r').
\end{aligned} \tag{2.91}$$

Performing the integrals involving delta-function yields:

$$\begin{aligned}
&\Delta S_{\ell j}(r, r'; E) = \\
&\frac{i}{\pi^2}\mathcal{P}\int k^2\mathrm{d}k\frac{j_\ell(kr)}{E-\varepsilon_k}\mathcal{P}\int k'^2\mathrm{d}k'\left(\Sigma_{\ell j}(k,k';E+i\eta)-\Sigma_{\ell j}(k,k';E-i\eta)\right)\frac{j_\ell(k'r')}{E-\varepsilon_{k'}} \\
+\ &\frac{\mu k_0}{\pi}j_\ell(k_0r)\mathcal{P}\int k'^2\mathrm{d}k'\left(\Sigma_{\ell j}(k_0,k';E+i\eta)+\Sigma_{\ell j}(k_0,k';E-i\eta)\right)\frac{j_\ell(k'r')}{E-\varepsilon_{k'}} \\
+\ &\frac{\mu k_0}{\pi}j_\ell(k_0r')\mathcal{P}\int k^2\mathrm{d}k\left(\Sigma_{\ell j}(k,k_0;E+i\eta)+\Sigma_{\ell j}(k,k_0;E-i\eta)\right)\frac{j_\ell(kr)}{E-\varepsilon_k} \\
-\ &i\left(2\mu k_0\right)^2 j_\ell(k_0r)\left(\Sigma_{\ell j}(k_0,k_0;E+i\eta)-\Sigma_{\ell j}(k_0,k_0;E-i\eta)\right)j_\ell(p_0r'),
\end{aligned} \tag{2.92}$$

involving similar principle value integrals as used in the solution of the reducible self-energy.

2.9 Connection to the Scattering

In the language of many-body theory, the elastic nucleon-nucleus scattering is determined by the on-shell matrix element of the reducible self-energy $\Sigma_{\ell j}(k, k'; E)$, since it is directly related to the $\mathcal{S}$-matrix by [10]

$$\begin{aligned} \langle k_0|\mathcal{S}_{\ell j}(E)|k_0\rangle &\equiv e^{2i\delta_{\ell j}} \\ &= 1 - 2\pi i \left(\frac{mk_0}{\hbar^2}\right) \langle k_0|\Sigma_{\ell j}(E)|k_0\rangle, \end{aligned} \tag{2.93}$$

where $k_0 = \sqrt{2mE}/\hbar$, m is the nucleon mass, and E is the energy relative to the center-of-mass. The phase shift, $\delta_{\ell j}$, defined by Eq. (2.93) is in general a complex number. Its real part yields the usual phase shift and its imaginary part is associated with the inelasticity of the scattering process and denoted by

$$\eta_{\ell j} = e^{-2\Im\mathfrak{m}(\delta_{\ell j})}. \tag{2.94}$$

In general, the coupling to more complicated excitations in the self-energy implies a complex potential responsible for the loss of flux in the elastic channel, characterized by the inelasticities $\eta_{\ell j}$.

For completeness we include some relevant results in terms of the phase shifts $\delta_{\ell j}$ for the quantities that will be discussed later. The scattering amplitude is given by

$$f_{m'_s,m_s}(\theta,\phi) = -\frac{4m\pi^2}{\hbar^2}\langle \boldsymbol{k}' m'_s|\Sigma(E)|\boldsymbol{k} m_s\rangle, \tag{2.95}$$

with wave vectors of magnitude k_0. The matrix structure is usually represented by

$$[f(\theta,\phi)] = \mathcal{F}(\theta)I + \sigma\cdot\hat{\mathbf{n}}\mathcal{G}(\theta), \tag{2.96}$$

based on rotational invariance and parity conservation. The unit vector is given by $\hat{\mathbf{n}} = \mathbf{k} \times \mathbf{k}'/|\mathbf{k} \times \mathbf{k}'|$, and σ is formed by the Pauli spin matrices. The relation between $\mathcal{F}$ and $\mathcal{G}$ and the phase shifts determined by Eq. (2.93), can now be worked out yielding

$$\begin{aligned} \mathcal{F}(\theta) &= \frac{1}{2ik}\sum_{\ell=0}^{\infty}\Big[(\ell+1)\left\{e^{2i\delta_{\ell+}}-1\right\} \\ &+ \ell\left\{e^{2i\delta_{\ell-}}-1\right\}\Big]P_\ell(\cos\theta) \end{aligned} \tag{2.97}$$

and

$$\mathcal{G}(\theta) = \frac{\sin\theta}{2k}\sum_{\ell=1}^{\infty}\left[e^{2i\delta_{\ell+}} - e^{2i\delta_{\ell-}}\right]P'_\ell(\cos\theta). \tag{2.98}$$

We employ the notation $\delta_{\ell\pm} \equiv \delta_{\ell j=\ell\pm\frac{1}{2}}$ and P'_ℓ denotes the derivative of the Legendre polynomial with respect to $\cos\theta$. The unpolarized cross section reads

$$\left(\frac{d\sigma}{d\Omega}\right)_{unpol} = |\mathcal{F}|^2 + |\mathcal{G}|^2. \tag{2.99}$$

Employing the partial wave expansions Eqs. (2.97) and (2.98) and the orthogonality of the Legendre polynomials, we find

$$\begin{aligned} \sigma_{tot}^{el} &= \frac{\pi}{k^2}\sum_{\ell=0}^{\infty}\frac{\left|(\ell+1)\left\{e^{2i\delta_{\ell+}}-1\right\}+\ell\left\{e^{2i\delta_{\ell-}}-1\right\}\right|^2}{2\ell+1} \\ &+ \frac{\pi}{k^2}\sum_{\ell=0}^{\infty}\frac{\ell(\ell+1)\left|e^{2i\delta_{\ell+}}-e^{2i\delta_{\ell-}}\right|^2}{2\ell+1}. \end{aligned} \tag{2.100}$$

We can define partial elastic cross sections such that

$$\sigma_{tot}^{el} = \sum_{\ell=0}^{\infty}\sigma_\ell^{el}, \tag{2.101}$$

which for a given ℓ reads

$$\sigma_\ell^{el} = \frac{\pi}{k^2}\left[(\ell+1)\left|e^{2i\delta_{\ell+}}-1\right|^2 + \ell\left|e^{2i\delta_{\ell-}}-1\right|^2\right]. \tag{2.102}$$

With complex potentials, and therefore complex phase shifts, it is possible to calculate the total reaction cross section

$$\sigma_{tot}^r = \sum_{\ell=0}^{\infty}\sigma_\ell^r, \tag{2.103}$$

with

$$\sigma_\ell^r = \frac{\pi}{k^2}\left[(2\ell+1)-(\ell+1)\left|e^{2i\delta_{\ell+}}\right|^2 - \ell\left|e^{2i\delta_{\ell-}}\right|^2\right]. \tag{2.104}$$

These results are derived by using the optical theorem that yields the total cross section from the imaginary part of the forward scattering amplitude.

$$\sigma_T = \sigma_{tot}^{el} + \sigma_{tot}^r. \tag{2.105}$$

The results presented here refer to neutron scattering when the self-energy has a finite range.

Therefore, it is clear that at positive energies the problem is completely reduced to solving the integral equation for the reducible self-energy given in Eq. (2.48). It should be noted that the solution in momentum space automatically treats the non-locality of the reducible self-energy in coordinate space. In practice, the integral equation is solved in two steps. First the integral equation is solved by only including the principal value part of the noninteracting propagator. Subsequently, it is straightforward to employ the resulting reaction matrix to take into account the contribution of the δ-function associated with the imaginary part of the noninteracting propagator.

2.10 Aspects of optical potentials

In a nuclear reaction where a nucleon heads into a nucleus (target), there is a chance that the target is excited and the initial quantum numbers such as energy, orbital and total angular momentum of the incident nucleon are altered. This is referred to by Bethe as an "absorption" process of the incoming nucleon [18]. The average effect of the absorption can be incorporated by including an imaginary term in the mean field. The imaginary part of the potential, W, is the main feature and building block of the optical potentials [19]. This imaginary term will lead to a subtraction of the total probability current when writing the continuity equation for the single-particle Schrödinger wave equation:

$$\nabla \cdot \boldsymbol{j} + \frac{\partial \rho}{\partial t} = \frac{W_\rho}{\hbar}, \tag{2.106}$$

where $\boldsymbol{j}$ is the probability current density and ρ is the probability density. Since ρ is approximately proportional to $e^{2W/\hbar}$, the lifetime of the system with the nucleon added to the target is given by $\tau = -\hbar/2\tilde{W}$. Here $\tilde{W}$ denotes the average of $W(r)$. In general W can be a function of energy as well. Moreover, the size of the energy interval or width of the domain where the single-particle strength is spread is given by $\Gamma = -2\tilde{W}$. The single-particle equation to be solved for an optical potential is the same as the Schrödinger equation where the real potential is supplemented with an imaginary potential.

There is a lot more empirical information on the mean field available at positive than at negative energies since data can be obtained for many incident energies and scattering angles. Analyzing the scattering cross sections demonstrates that the real and imaginary parts of the mean field both depend upon energy. As discussed in Sec. 2.4, the HF term of a microscopic self-energy does not depend on the energy. The phenomenological mean field is usually

assumed to be local and written in the following form:

$$U(r;E) = V(r;E) + iW(r;E). \tag{2.107}$$

The experimental data require that $W(r;E)$ be surface-peaked at low energy. The real part of the potential $V(r;E)$ can be expressed in terms of a Wood-Saxon form given by:

$$f(r,R,a) = \frac{1}{1+\exp\left(\frac{r-R}{a}\right)}, \tag{2.108}$$

where R is the radius and a is the diffuseness of the Wood-Saxon potential. One often uses the following parametrization:

$$V(r;E) = V^0(E) f(r,R_v,a_v), \tag{2.109}$$

$$W(r;E) = W_V(E) f(r,R_W,a_W) - 4a_W W(E)\frac{d}{dr} f(r,R_W,a_W), \tag{2.110}$$

where the radius and diffuseness parameters are not necessarily the same for different potential terms. Phenomenological optical-model analyses of the experimental scattering data then involve nine adjustable parameters at each energy. In practice, the data cannot accurately determine all these parameters. Nevertheless the volume integrals of these potentials appear to be more uniquely determined. These volume integrals are given by:

$$\begin{aligned} J_V(E) &= \int V(r;E)\; d^3r \\ J_W(E) &= \int W(r;E)\; d^3r. \end{aligned} \tag{2.111}$$

Local optical potentials with an energy dependent depth and energy independent form factor have proved able to give differential cross sections in good accord with the experimental data

for many nuclei. Some of the parameters are almost independent of the target nucleus [20]. Several global potentials have been proposed and have been extensively compared with experimental data [21, 22, 23]. The prediction of even the best global potentials shows definite discrepancies with experimental data and these can be attributed to nuclear structure effects. It is possible to improve the fits by adjusting the parameters for each nucleus, but thereby the predictive advantage of the "global" potentials is lost. Mahaux and Sartor realized that optical potentials could be used to extrapolate to negative energies by using the appropriate dispersion relation which in principle connects the real and imaginary parts of the potential. Phenomenological optical potentials in general do not fulfill this dispersion relation. Mahaux and Sartor proposed to employ optical potentials that fulfill this dispersion relation thereby linking positive energy and negative energy data. The resulting DOM is extensively reviewed in Ref. [2]. Further confirmation of this approach is provided by the analysis of single-particle energies; the gap between low-lying particle and hole states is smaller than can be obtained with a static potential suggesting the need of dispersive correction to the real part of the potential [2].

As discussed in Sec. 2.4, the self-energy has two terms, the static term does not explicitly depend on the energy and the dynamic part that depend on the energy. The latter takes into account the higher-order corrections to the self-energy (or Green's function). The static term is usually referred as the HF term. Both the static and dynamic part are in principle nonlocal. In earlier DOM implementations the nonlocal HF term has been replaced by an equivalent energy-dependent potential. This can have undesired consequences. In particular the solutions to the Dyson equation, when the optical potential is interpreted as the self-energy, suffer from a distortion of the normalization which can only be corrected properly near the Fermi energy and plays no role at positive energies where only the real and imaginary parts of the phase shift are required. We will see in Chs. 3 and 4 that a nonlocal version of self-energy is necessary in particular for the description of data below the Fermi energy.

A typical form to describe the nonlocality of the potential was proposed by Perey and Buck [24]. An example is given for the energy independent contribution by:

$$V_{NL}(\boldsymbol{r}, \boldsymbol{r'}) = U\left(\frac{|\boldsymbol{r} + \boldsymbol{r'}|}{2}\right) H(|\boldsymbol{r} - \boldsymbol{r'}|). \tag{2.112}$$

The factor U is parametrized with a Woods-Saxon potential. Using the approximation:

$$\tilde{r} = \frac{|\boldsymbol{r} + \boldsymbol{r'}|}{2} \approx \frac{r + r'}{2} \tag{2.113}$$

U can be written as:

$$U(\tilde{r}) = V_0 f(\tilde{r}) \tag{2.114}$$

where V_0 is the potential depth and f represents a Woods-Saxon shape with the dependence on the radius and diffuseness parameters implied. The factor H is a Gaussian function:

$$H(\boldsymbol{r} - \boldsymbol{r'}) = \frac{1}{\pi^{3/2}\beta^3} \exp\left[\frac{|\boldsymbol{r} - \boldsymbol{r'}|^2}{\beta^2}\right]. \tag{2.115}$$

The parameter β controls the degree of nonlocality of V_{NL}, and empirically has been determined to be on the order of 1 fm [2]. The projection of H has an analytical solution due to the relationship between the spherical Bessel functions j_ℓ and the Legendre polynomials P_ℓ

$$j_\ell(z) = \frac{1}{2\,i} \int_{-1}^{+1} e^{izx}\, P_\ell(x)\, dx. \tag{2.116}$$

Using this result one finds:

$$V_{NL}^{\ell}(r, r') = U(r, r') \frac{1}{\pi^{1/2}\beta} \exp\left[-\frac{r^2 + r'^2}{\beta^2}\right] \mathcal{K}_\ell(\frac{2rr'}{\beta^2}) \tag{2.117}$$

where

$$\mathcal{K}_\ell(t) = 2(-i)^\ell \; t \; j_\ell(it). \tag{2.118}$$

This type of nonlocality is employed in the next chapters to describe the real and imaginary part of the self-energy for ^{40}Ca and ^{48}Ca.

3 Calcium Forty

3.1 Introduction

Previous implementations of the dispersive optical model have mostly relied on employing local potentials. When describing the properties of the ground-state of closed-shell nuclei it is necessary to abandon this tradition. The energy dependence of the real HF term in the local implementation of the DOM was used to represent its nonlocal character. Since this energy dependence is not associated with the dispersion relation it distorts the normalization of the solutions of the Dyson equation. Nonlocality was restored in Ref. [3] in a study of ^{40}Ca. Nevertheless, properties like particle number and the charge density cannot be described when only the HF term is made nonlocal. Further evidence to support the introduction of nonlocal imaginary potentials is provided by the work of Refs. [25, 17] for ^{40}Ca. Inclusion of long-range correlations in the self-energy using the FRPA approach clearly shows strong ℓ-dependence of the imaginary part of the nucleon self-energy [25] which implies the presence of a substantial nonlocality. Even inclusion of short-range correlations in the self-energy leads to nonnegligible ℓ-dependence in the imaginary part of the self-energy as it is shown in Ref. [17].

In this chapter we introduce a comprehensive description of all SP properties associated with the nucleus ^{40}Ca employing a nonlocal representation of both real and imaginary part of the self-energy which obey the relevant dispersion relation. Employing DOM potentials (as fully described in previous chapters), all the relevant data below and above the Fermi energy can be reproduced simultaneously. The connection between the potential below and above Fermi energy is carried through using the dispersion relation.

3.2 Procedure

In order to build a fully nonlocal self-energy the appropriate starting point is to employ the local DOM form which can describe available scattering data [20, 26, 16] and extend it to a nonlocal version. Instead of the radial r-dependence of the local DOM used in Ref. [20] we require a dependence of the potential on the vectors $\boldsymbol{r}$ and $\boldsymbol{r}'$. Rotational invariance implies this dependence only involves the magnitudes r and r' and the angle between these two vectors. This angular dependence leads to an ℓ-dependent DOM potential. Including this nonlocality makes the computation more expensive but allows us to evaluate properties such as spectral functions that were not available in local DOM versions. The parametrized nonlocal potential is then employed in the Schrödinger-like equation to generate bound-state properties allowing us to constrain the self-energy. Further constraints on the self-energy parameters are obtained by solving Dyson's equation at negative energies. From the resulting propagator, one can generate the charge density that can be compared to the experimental data. The bound-state properties provided by the particle numbers, proton charge density, energy levels and high missing momenta can then be included in the total chi-squared analysis. At positive energies the elastic scattering cross sections for protons and neutrons, the total cross section for neutrons and the reaction cross section for protons and neutrons were generated from the self-energy to complete the remaining chi-squared

ingredients. Since there are less data at negative energies we started the fit by considering just bound-state properties. After these properties were generated in good agreement with available data, within the assigned errors, the same procedure was repeated to obtain a good representation of the scattering data at positive energies. A refit of the bound-state properties was then necessary on account of the dependence on the properties of the self-energy at positive energies associated with the dispersion relation. The link between the self-energy at positive and negative energy, as well as the reduced number of available data at negative energies, present a difficulty in constraining the self-energy and this process has to be repeated several times.

3.3 Parametrization of the potentials

We provide a detailed description of the DOM functionals in order for the resulting potential to yield a realistic description of the single-particle properties below and above the Fermi energy. We use a simple Gaussian nonlocality in all instances. We restrict the nonlocal contributions to the HF term and the volume and surface contributions of the imaginary part of the potential. We write the HF self-energy term in the following form

$$\Sigma_{HF}(\boldsymbol{r},\boldsymbol{r}') = \Sigma^{nl}_{HF}(\boldsymbol{r},\boldsymbol{r}') + \delta(\boldsymbol{r}-\boldsymbol{r}')\left[V_C(r) + V^{so}(r)\right],$$

with the Coulomb and local spin-orbit contributions. The nonlocal term is split into a volume and a wine-bottle shape generating contribution

$$\Sigma^{nl}_{HF}(\boldsymbol{r},\boldsymbol{r}') = -V^{vol}_{HF}(\boldsymbol{r},\boldsymbol{r}') + V^{wb}_{HF}(\boldsymbol{r},\boldsymbol{r}'),$$

where the volume term is given by

$$V_{HF}^{vol}\left(\boldsymbol{r},\boldsymbol{r'}\right)=V_{HF}^{0}\,f\left(\tilde{r},r^{HF},a^{HF}\right)\times\left[x_{1}H\left(\boldsymbol{s};\beta_{vol_{1}}\right)+\left(1-x_{1}\right)H\left(\boldsymbol{s};\beta_{vol_{2}}\right)\right], \tag{3.1}$$

allowing for two different nonlocalities with different weight ($0 \leq x_1 \leq 1$). We use the notation $\tilde{r} = (r + r')/2$ and $\boldsymbol{s} = \boldsymbol{r} - \boldsymbol{r'}$. The wine bottle ($wb$) shape producing Gaussian replaces the surface term of Ref. [16]

$$V_{HF}^{wb}(\boldsymbol{r},\boldsymbol{r'})=V_{wb}^{0}\exp\left(-\tilde{r}^{2}/\rho_{wb}^{2}\right)H\left(\boldsymbol{s};\beta_{wb}\right). \tag{3.2}$$

and is motivated by the work of [27]. Non-locality is represented by a Gaussian form

$$H\left(\boldsymbol{s};\beta\right)=\exp\left(-\boldsymbol{s}^{2}/\beta^{2}\right)/(\pi^{3/2}\beta^{3}).$$

As usual we employ Woods-Saxon form factors

$$f(r,r_{i},a_{i})=\left[1+\exp\left(\frac{r-r_{i}A^{1/3}}{a_{i}}\right)\right]^{-1}. \tag{3.3}$$

The Coulomb term is obtained from the calculated charge density and no longer by the potential from a homogeneous sphere as in all previous work (see *e.g.* [16]). The local spin-orbit interaction is given by

$$V^{so}(r)=\left(\frac{\hbar}{m_{\pi}c}\right)^{2}V_{0}^{so}\frac{1}{r}\frac{d}{dr}f(r,r^{so},a^{so})\;\ell\cdot\sigma, \tag{3.4}$$

where $(\hbar/m_\pi c)^2$=2.0 fm^2 as in Ref. [16].

The introduction of nonlocality in the imaginary part of the self-energy is well-founded theoretically both for long-range correlations [25] as well short-range ones [17]. Its implied

ℓ-dependence is essential in reproducing the correct particle number for protons and neutrons. As will be shown below, the assumed imaginary component of the potential has the form

$$\text{Im } \Sigma(\boldsymbol{r}, \boldsymbol{r'}, E) = \text{Im } \Sigma^{nl}(\boldsymbol{r}, \boldsymbol{r'}; E) + \delta(\boldsymbol{r} - \boldsymbol{r'})\mathcal{W}^{so}(r; E). \tag{3.5}$$

The nonlocal contribution is represented by

$$\begin{aligned} \text{Im } \Sigma^{nl}(\boldsymbol{r}, \boldsymbol{r'}; E) = &-W_{0\pm}^{vol}(E) f\left(\tilde{r}; r_{\pm}^{vol}; a_{\pm}^{vol}\right) H\left(\boldsymbol{s}; \beta_{vol}^{\pm}\right) \\ &+4a_{\pm}^{sur} W_{\pm}^{sur}(E) H\left(\boldsymbol{s}; \beta_{sur}^{\pm}\right) \frac{d}{d\tilde{r}} f(\tilde{r}, r_{\pm}^{sur}, a^{sur}), \end{aligned} \tag{3.6}$$

where the $\pm$ notation refers to quantities above $(+)$ and below $(-)$ the Fermi energy. At energies well removed from ε_F, the form of the imaginary volume potential should not be symmetric about ε_F as indicated by the $\pm$ notation [17]. While more symmetric about ε_F, we have allowed a similar option for the surface absorption that is also supported by theoretical work reported in Ref. [25]. We include a local spin-orbit contribution with the same form as in Eq. (3.4)

$$\mathcal{W}^{so}(r, E) = \left(\frac{\hbar}{m_\pi c}\right)^2 W^{so}(E) \frac{1}{r} \frac{d}{dr} f(r, r^{so}, a^{so})\ \ell \cdot \sigma, \tag{3.7}$$

using the same geometry parameters as in Eq. (3.4) following Ref. [16]. Allowing for the aforementioned asymmetry around ε_F the following form was assumed for the depth of volume potential [16]

$$W_{0\pm}^{vol}(E) = \Delta W_{NM}^{\pm}(E) + \begin{cases} 0 & \text{if } |E - \varepsilon_F| < E_{p\pm}^{vol} \\ A_{\pm}^{vol} \frac{\left(|E-\varepsilon_F| - E_{p\pm}^{vol}\right)^4}{\left(|E-\varepsilon_F| - E_{p\pm}^{vol}\right)^4 + (B_{\pm}^{vol})^4} & \text{if } |E - \varepsilon_F| > E_{p\pm}^{vol}, \end{cases} \tag{3.8}$$

where $\Delta W^{\pm}_{NM}(E)$ is the energy-asymmetric correction modeled after nuclear-matter calculations. The asymmetry above and below ε_F is essential to accommodate the Jefferson Lab $(e, e'p)$ data at large missing energy. The energy-asymmetric correction was taken as

$$\Delta W^{\pm}_{NM}(E) = \begin{cases} \alpha A^{vol}_{+} \left[\sqrt{E} + \frac{\left(\varepsilon_F + E^{+}_{a}\right)^{3/2}}{2E} - \frac{3}{2}\sqrt{\varepsilon_F + E^{+}_{a}} \right] & \text{for } E - \varepsilon_F > E^{+}_{a} \\ -A^{vol}_{-} \frac{(\varepsilon_F - E - E^{-}_{a})^2}{(\varepsilon_F - E - E^{-}_{a})^2 + (E^{-}_{a})^2} & \text{for } E - \varepsilon_F < -E^{-}_{a} \\ 0 & \text{otherwise} \end{cases} \tag{3.9}$$

To describe the energy dependence of surface absorption we employed the form of Ref. [20]

$$W^{sur}_{\pm}(E) = \omega_4(E, A^{sur}_{\pm}, B^{sur}_{\pm s1}, 0) - \omega_2(E, A^{sur}_{\pm}, B^{sur}_{\pm s2}, C^{sur}_{\pm}), \tag{3.10}$$

where

$$\omega_n(E, A^{sur}, B^{sur}, C^{sur}) = A^{sur}\ \Theta(X)\ \frac{X^n}{X^n + (B^{sur})^n}, \tag{3.11}$$

and $\Theta(X)$ is Heaviside's step function and $X = |E - \varepsilon_F| - C^{sur}$. As the imaginary spin-orbit component is generally needed only at high energies, we have kept the form employed in Ref. [16]

$$W^{so}(E) = A^{so} \frac{(E - \varepsilon_F)^4}{(E - \varepsilon_F)^4 + (B^{so})^4}. \tag{3.12}$$

All ingredients of the DOM have now been identified and their functional form described. In addition to the HF contribution and the absorptive potentials we also include the dispersive real part from all imaginary contributions according to the corresponding subtracted dispersion relation.

Neutron and proton potentials are kept identical in the fit except for the Coulomb poten-

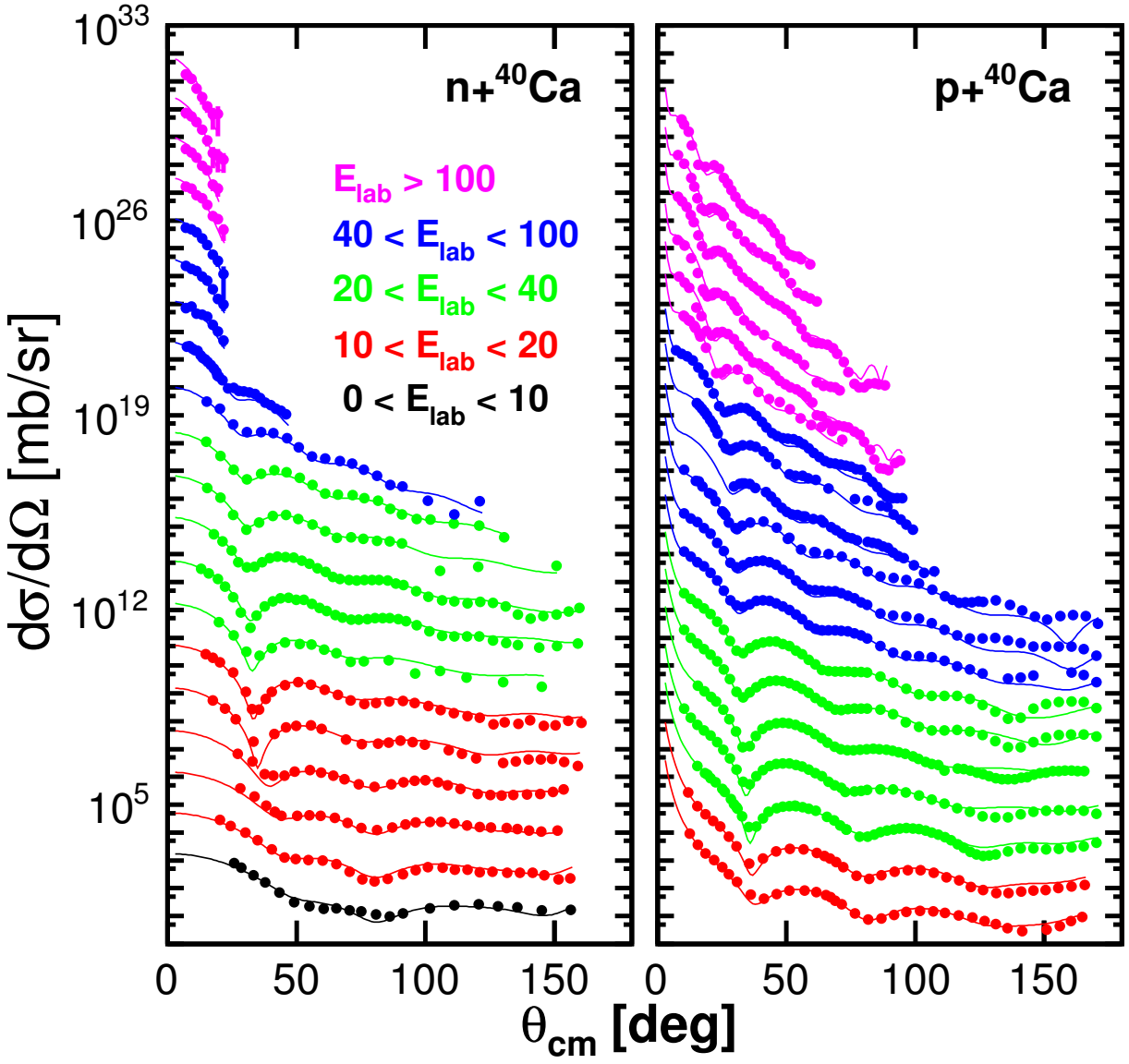

Figure 3.1: Calculated and experimental elastic-scattering angular distributions of the differential cross section. Panels shows results for n+^{40}Ca and p+^{40}Ca. Data for each energy are offset for clarity with the lowest energy at the bottom and highest at the top of each frame. References to the data are given in Ref. [16].

tial. Included in the present fit are the same elastic scattering data and level information considered in Ref. [16]. We refer to that paper for references to these data. In addition, we now include the charge density of ^{40}Ca as given in Ref. [28] by a sum of Gaussians in the determination of the DOM parameters. The calculation of the charge density requires a rescaling of the calculated density matrix from the $A-1$ to the A-body system as in Ref. [29]. From now on we denote with N the total neutron number, Z the proton one and $A = N + Z$ the nucleon number.

3.4 Screened Coulomb Potential

The calculation of the spectral functions for energies greater than zero is formulated in momentum space. The treatment of the Coulomb potential for protons in momentum space is a substantial numerical challenge. A possible solution is to employ a screened Coulomb potential by introducing an exponential factor [30, 31]. The resulting contribution has a finite range and the usual application of scattering theory in momentum space can be applied. In the case of scattering from a Coulomb potential the scattering amplitude consists of two contributions. The first one represents the point Coulomb amplitude and the second includes the effect of the nuclear potential together with the correction due to the finite charge distribution. The effect of the latter contribution can be properly calculated in momentum space as it is of finite range as shown in Refs. [30, 31]. The screened Coulomb potential is chosen to have the following form:

$$\mathcal{S}_R^n(r) = \mathcal{S}(r)\, e^{-\left(\frac{r}{R}\right)^n} \tag{3.13}$$

characterized by two parameters R and n. The Coulomb potential is represented by $\mathcal{S} = Z\alpha/r$ with $\alpha \approx 1/137$ the fine structure constant. The parameter n controls the smoothness

of the exponential term and the radius parameter R determines the range of the screened Coulomb potential and therefore should be larger than the range of the nuclear potential. The parameter n must be chosen large enough to allow a complete representation of the Coulomb potential in the domain where the nuclear potential acts. In Ref. [30] it was shown that $n = 4$ is a practical choice to obtain accurate phase shifts and we have also employed this value. The use of the screened Coulomb potential makes it possible to calculate the spectral functions for protons at $E > 0$ as will be shown in 3.5.3.

3.5 Results

3.5.1 Cross Sections

The final fit to the experimental elastic scattering data is shown in Fig 3.1 while the fits to total and reaction cross sections are shown in Fig. 3.2. In all cases, the quality of the fit is the same as in Refs. [16] or [26]. This statement also holds for the analyzing powers which are shown in Fig. 3.3. It should be emphasized that the number of parameters has not increased substantially compared to previous local calculations in [26] and [16] except for the decoupling of the imaginary volume and surface potential strength below and above Fermi energy as suggested by the theoretical work of Refs. [25, 17].

3.5.2 Spectral information below ε_F

The hole spectral density for energies below the Fermi energy is given by Eq. (2.74) in Sec. 2.8.1. The spectral strength at energy E for a given ℓj is given by

$$S_{\ell j}(E) = \int_0^\infty dr\ r^2\ S_{\ell j}(r; E). \tag{3.14}$$

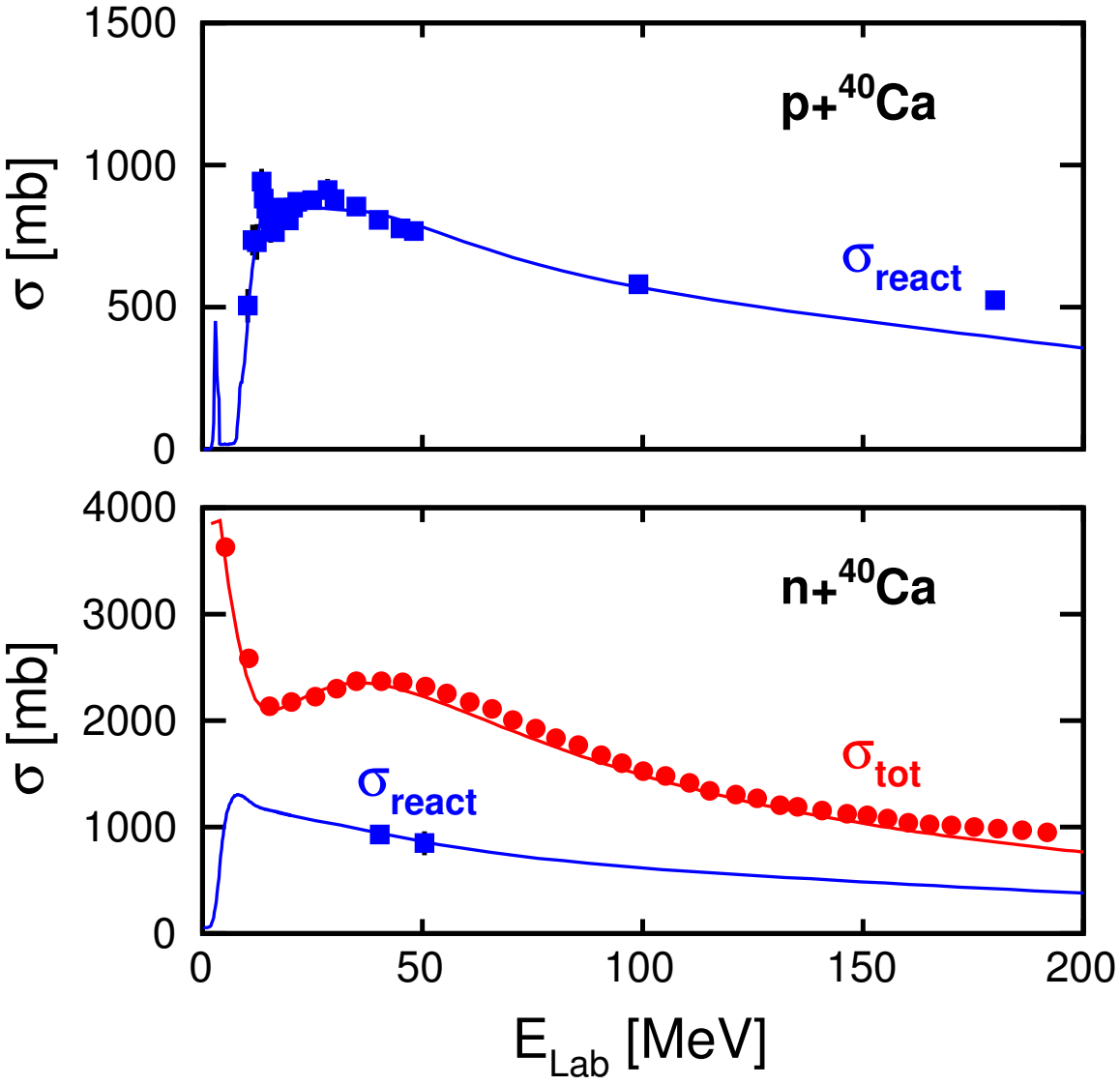

Figure 3.2: Total reaction cross sections are displayed as a function of proton energy while both total and reaction cross sections are shown for neutrons.

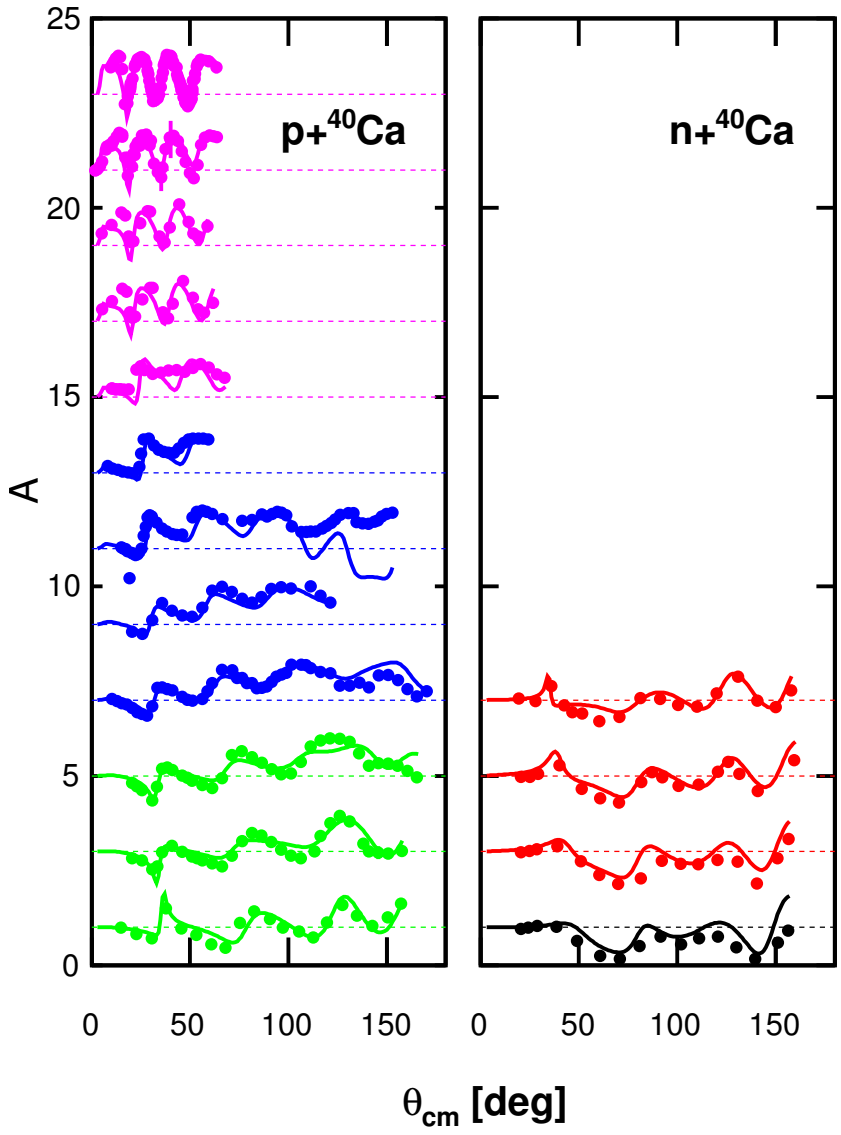

Figure 3.3: Fitted analyzing powers for proton and neutron elastic scattering on ^{40}Ca. For clarity, successively larger energies have been shifted further up along the vertical axis. The dashed lines indicate zero analyzing power for each energy.

In Fig. 3.4 we display the spectral strength given in Eq. (3.14) as a function of energy for the first few levels in the independent-particle model. The downward arrows identify the experimental location of the levels near the Fermi energy while for deeply bound levels they correspond to the peaks obtained from $(p, 2p)$ [32] and $(e, e'p)$ reactions [33]. The DOM strength distributions track the experimental results represented by their peak location and width. For the quasi-hole states we find spectroscopic factors of 0.78 for both the $1s_{1/2}$ and 0.76 for the $0d_{3/2}$ level. The location of the former deviates slightly from the experimental peak which may require additional state dependence of the self-energy as expressed by poles nearby in energy [34]. The analysis of the $(e, e'p)$ reaction in Ref. [35] clarified that the treatment of non-locality in the relativistic approach leads to different distorted proton waves as compared to conventional non-relativistic optical potentials, yielding about 10-15% larger spectroscopic factors. Our current results are also larger by about 10-15% than the numbers extracted in Ref. [36]. It should be noted the traditional extraction of spectroscopic factor from experimental data employs local optical potentials for the outgoing proton in the $(e, e'p)$ reaction. It will be interesting in future to employ our nonlocal optical potential to describe this distorted wave as well as the overlap function for proton removal obtained from the same nonlocal DOM potential at negative energy. Introducing local DOM potentials in the analysis of transfer reactions has been shown to have salutary effects for the extraction of spectroscopic information of neutrons [37] and nonlocal potentials should further improve such analyses [9]. In Table 3.1 the calculated quasihole energies are compared with the experimental data. Except for the $1s_{1/2}$ which shows about a 3 MeV discrepancy with experiment, the other levels are in reasonably good agreement with the experimental result.

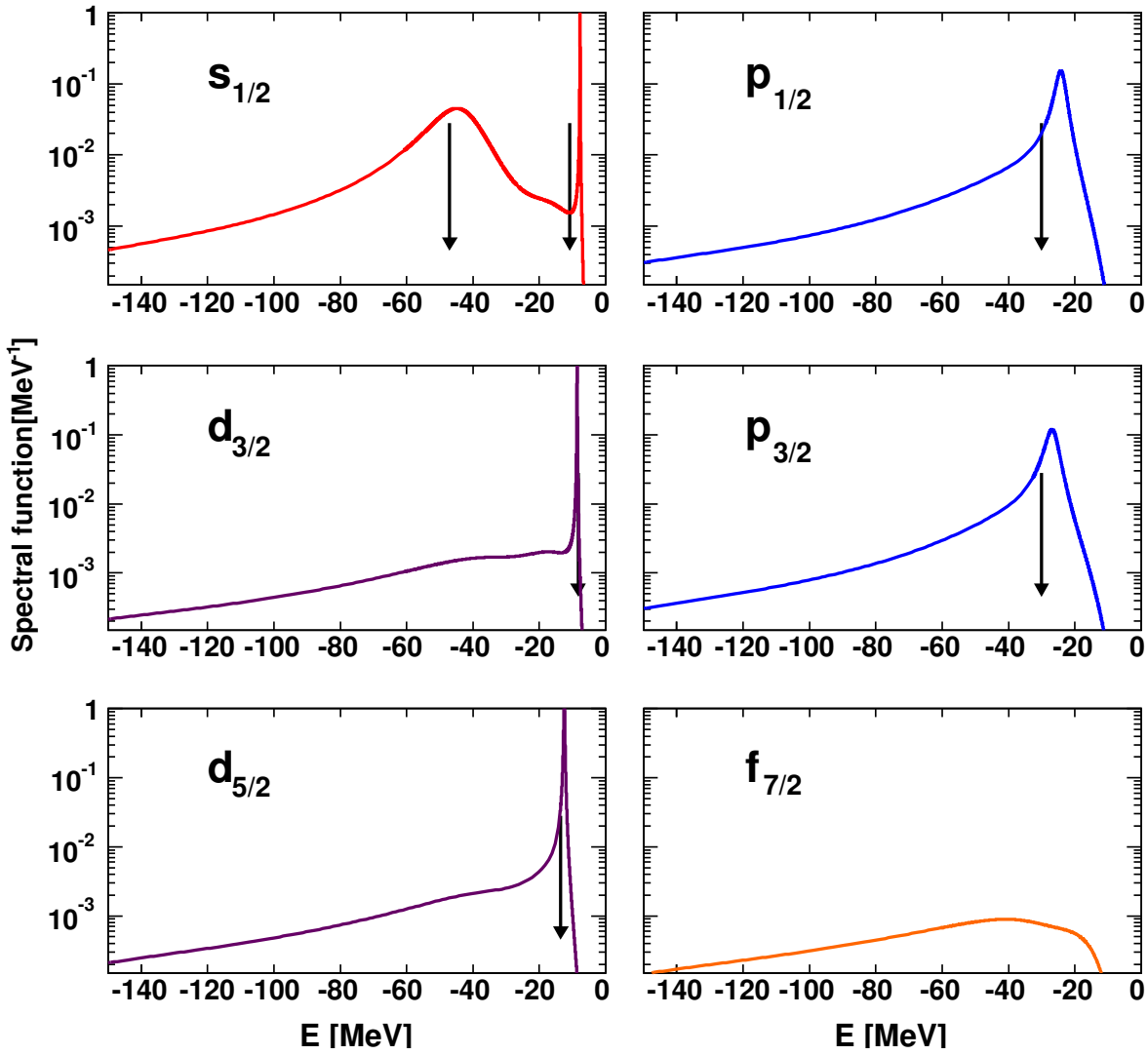

Figure 3.4: Spectral strength for protons in the ℓj orbits which are fully occupied in the independent-particle model as well as the $f_{7/2}$ strength associated with the first empty orbit in this description. The arrows indicate the experimental location of the valence states as well as the peak energies for the distributions of deeply bound ones.

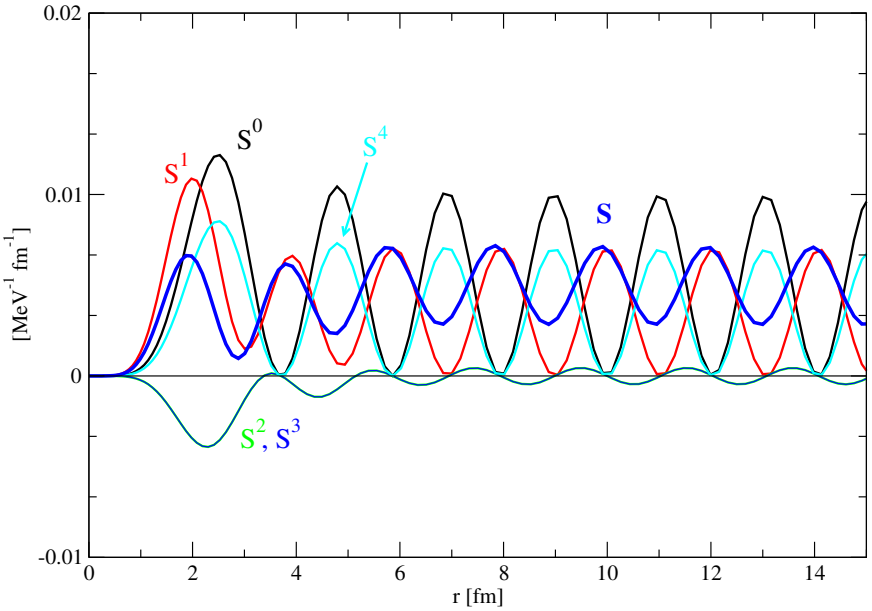

(a) $\ell = 2 \;\; j = 3/2 \;\; E = 30$

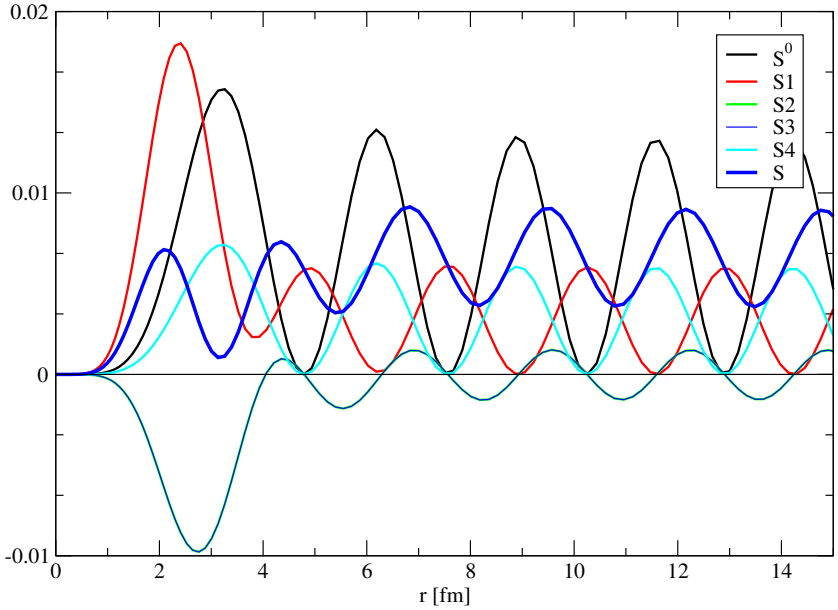

(b) $\ell = 2 \;\; j = 3/2 \;\; E = 50$

Figure 3.5: Different contributions to the $S_{\ell j}(r, r; E)$ which are the four terms in the Eq. (2.92) in addition to the zeroth term, $S^0_{\ell j}(r, r; E)$ (the black curve).

Table 3.1: Quasihole energies in MeV for neutron orbits in ^{40}Ca near the Fermi energy compared with experiment.

orbit	DOM [MeV]	Experiment [MeV]
$1p_{3/2}$	-3.47	-4.20
$1p_{1/2}$	-4.51	-5.86
$0f_{7/2}$	-7.36	-8.36
$0d_{3/2}$	-16.2	-15.6
$1s_{1/2}$	-15.3	-18.3

3.5.3 Spectral information above ε_F

For the energies greater than zero, the spectral density has to be calculated using its formal expression Eq. (2.64). This equation can be expressed in coordinate space as well. The different contributions to the spectral density are calculated according to Eqs. (2.86) and (2.87). The latter represents the contribution due to the presence of the potential. The spectral density function $S_{\ell j}(r, r'; E)$ is positive and real on the diagonal which is also numerically confirmed. The different contributions to diagonal part of $S_{\ell=2,j=3/2}(r, r'; E)$ in Eq. (2.92) are plotted in Fig. 3.5 for two different energies $E = 30$ MeV and $E = 50$ MeV. The two terms S^2 and S^3 contain negative contributions and are identical.

In Fig. 3.6 the total spectral function, its elastic contribution and their difference are plotted in case of $\ell = 0$ for different energies. Asymptotically at large distances, the influence of other open channels is represented by a constant shift, whereas, inside the range of the potential, a pattern related to the absorptive properties of the potential and the orbits that are occupied emerges. To investigate more of the properties of the DOM potential, we plotted the 3-d plots of $S_{\ell j}(r, r; E)$ for several energies and ℓj values. It should be mentioned that in the plots the contribution of elastic channel ($\chi^{elE}_{\ell j}$ in Eq. (2.80)) is subtracted. Figs. 3.7- 3.10 demonstrate that the results for the difference of the spectral function with the elastic contribution as a function of distance r and energy for different orbits exhibits a very characteristic pattern. These patterns suggest that they are dominated by the presence of already occupied states

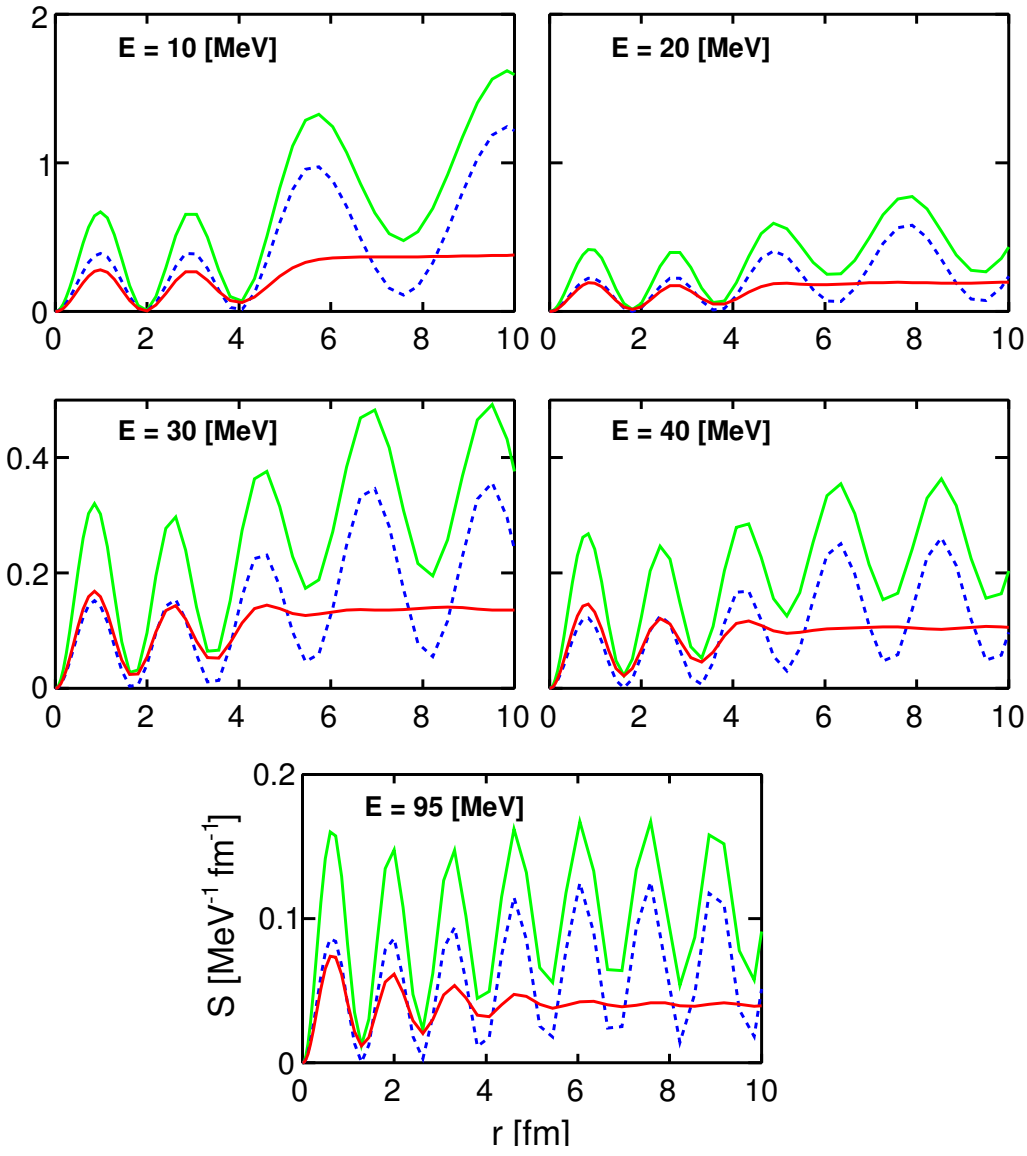

Figure 3.6: The diagonal part of the difference (red curve) between the particle spectral function (green curve) and the contribution of the elastic-scattering wave function multiplied by r^2 (dashed blue curve), for $s_{1/2}$ as a function of position for different energies. Asymptotically with r, this difference is approximately constant and determined only by the inelasticity.

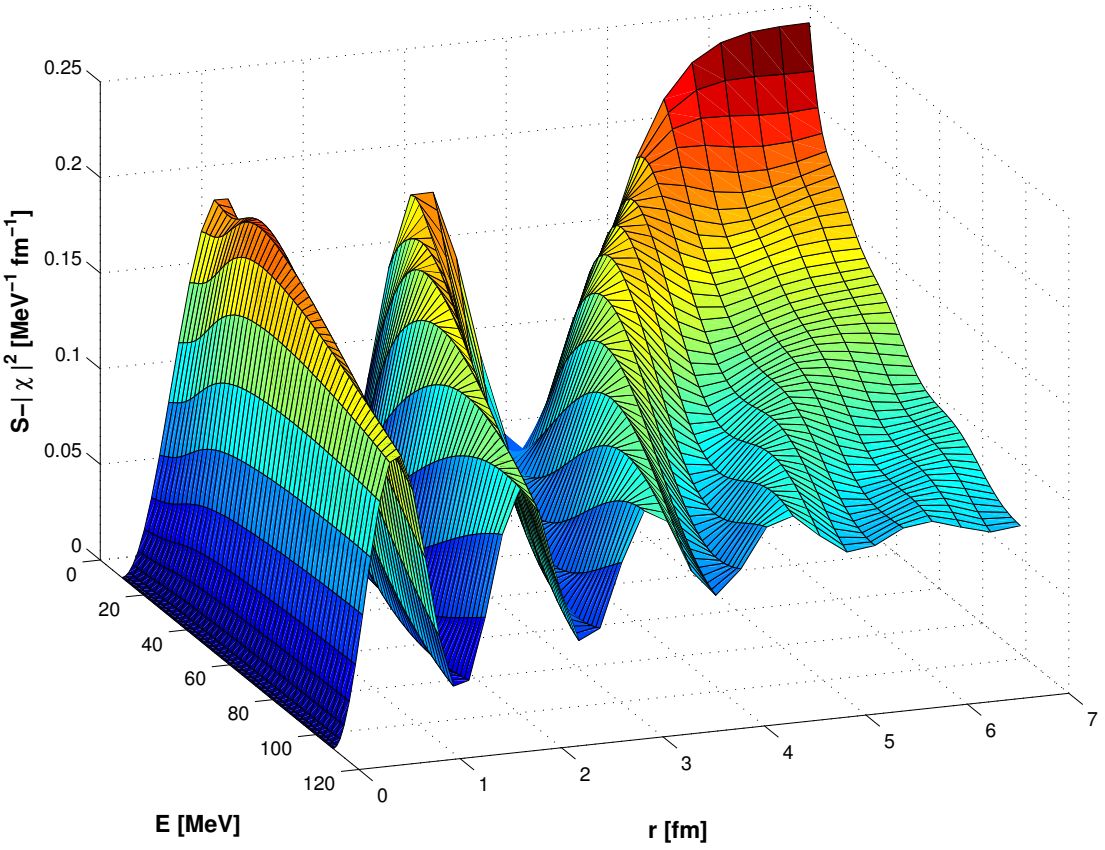

Figure 3.7: Difference between the particle spectral function and the contribution of the elastic-scattering wave function multiplied by r^2, for $s_{1/2}$ as a function of both energy and position. Asymptotically with r, this difference is constant and determined only by the inelasticity.

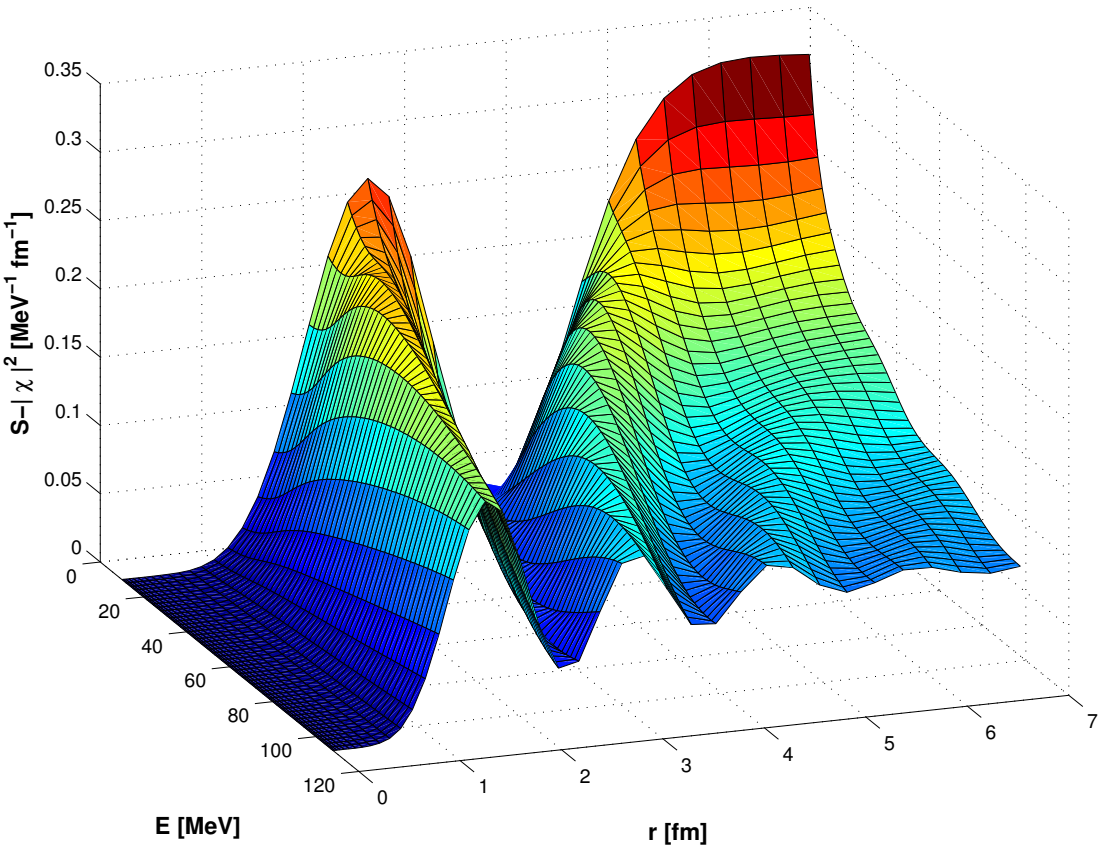

Figure 3.8: Difference between the particle spectral function and the contribution of the elastic-scattering wave function multiplied by r^2, for $d_{3/2}$ as a function of both energy and position. Asymptotically with r, this difference is constant and determined only by the inelasticity.

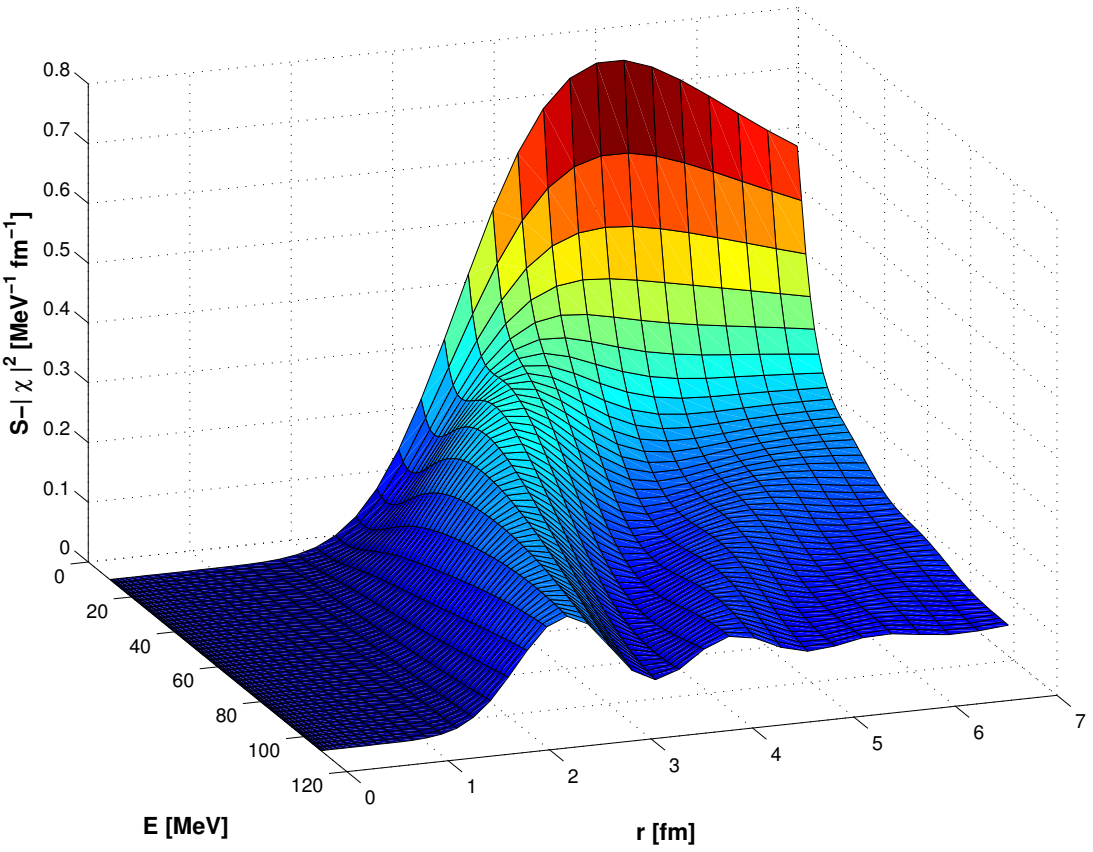

Figure 3.9: Difference between the particle spectral function and the contribution of the elastic-scattering wave function multiplied by r^2, for $f_{5/2}$ as a function of both energy and position.

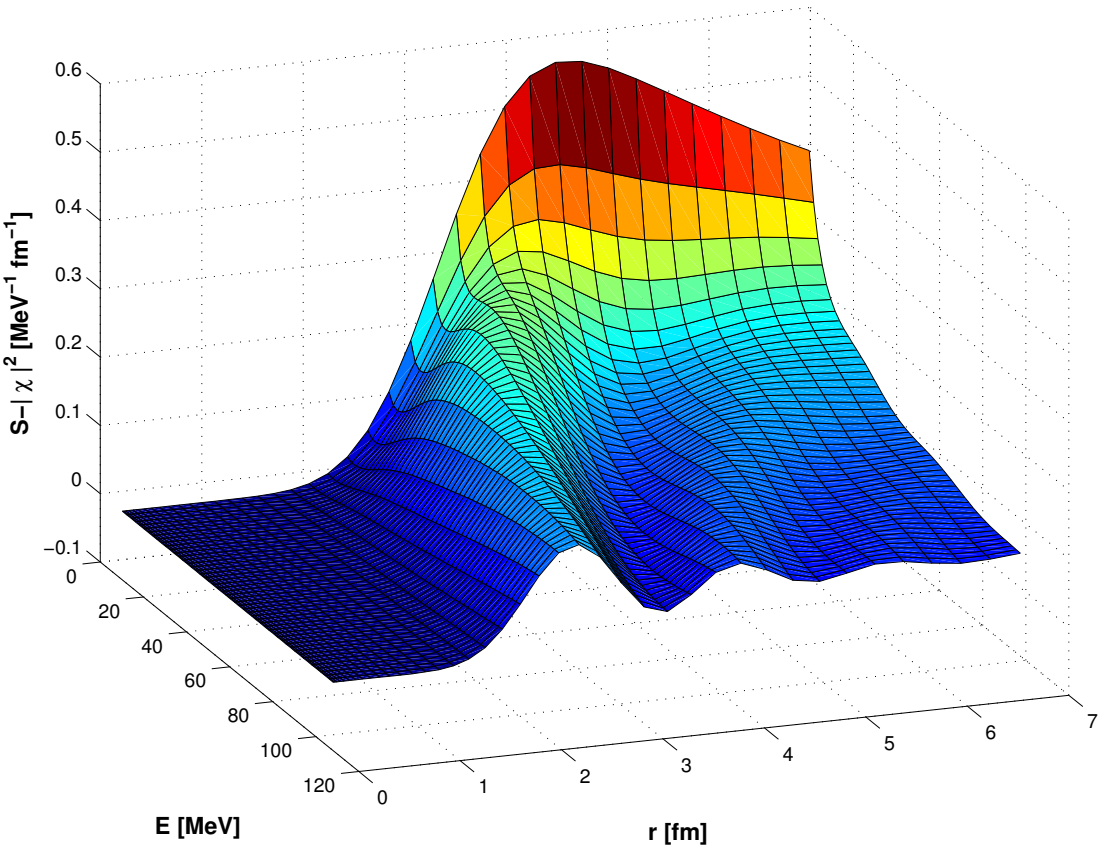

Figure 3.10: Difference between the particle spectral function and the contribution of the elastic-scattering wave function multiplied by r^2, for $g_{7/2}$ as a function of both energy and position.

in the ground state as they illustrate a two-node structure for $s_{1/2}$ at low energy in Fig. 3.7 (two mainly occupied states), one node for $d_{3/2}$ in Fig. 3.8 (one occupied state), and no node for $f_{5/2}$ and $g_{7/2}$ (no occupied states) in Figs. 3.9 and 3.10. All patterns show the presence of more nodes evolving at higher energies.

In Fig 3.11 the spectral function for $\ell = 0$ is plotted for different energies and compared with

Figure 3.11: Spectral function (red curve) and its asymptotic behaviour (blue curve). The green curve is the free propagator spectral function.

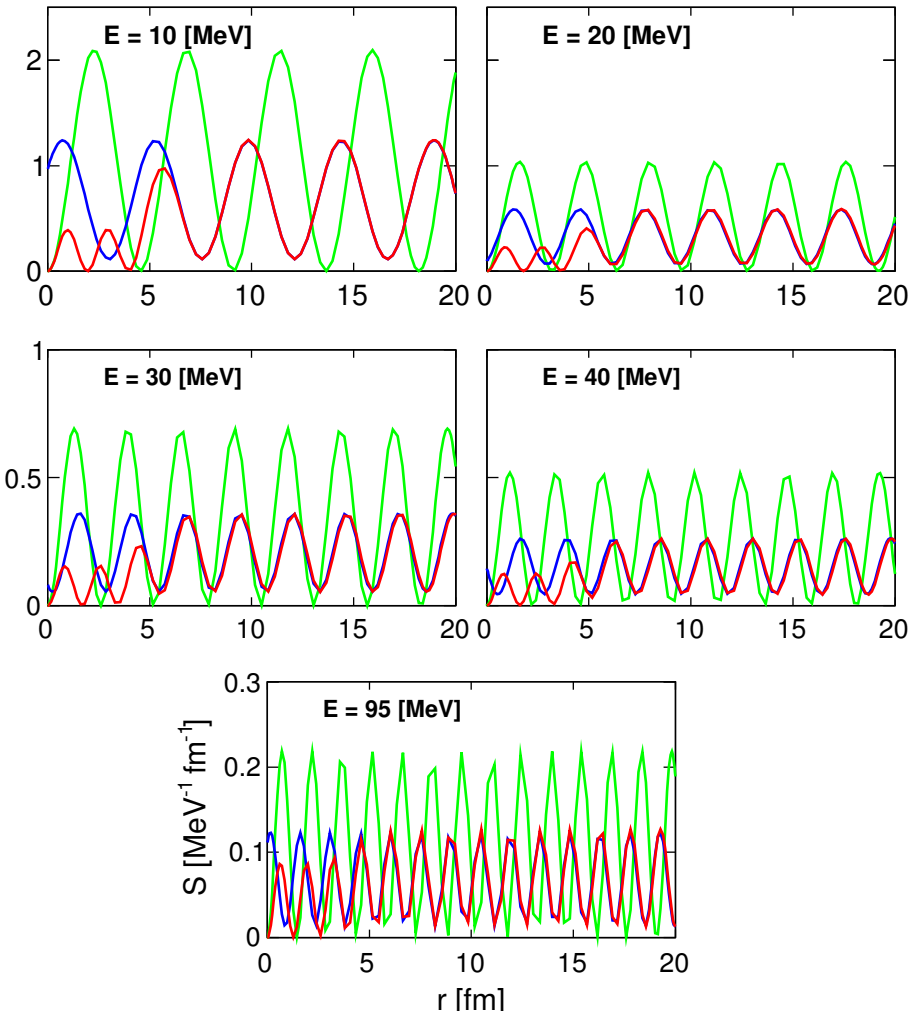

its asymptotic behavior and also the free propagator. As one expects at larger distances the spectral function and its asymptotic form must converge whereas for the interior the nuclear structure accounts for the reduction of the spectral function compared to the asymptotic behavior. This figure is included to illustrate the correct numerical implementation of various solutions of the Dyson equation.

3.5.4 Charge density

In Fig. 3.12 we compare the experimental charge density of ^{40}Ca (thick line representing a 1% error) with the DOM fit. The one-body density matrix can be obtained by integrating the imaginary part of the propagator for a given ℓj up to the Fermi energy:

$$n_{\ell j}(r, r') = \frac{1}{\pi} \int_{-\infty}^{\varepsilon_F} dE \; \mathfrak{Im} G_{\ell j}(r, r'; E). \tag{3.15}$$

For protons the charge density can be calculated using the diagonal elements of the one-body density matrix:

$$\rho_p(r) = \frac{e}{4\pi} \sum_{\ell j} (2j+1) \; n_{\ell j}(r, r). \tag{3.16}$$

While some details could be further improved, it is clear that an excellent description of the charge density is possible in the DOM. The correct particle number is essential for this result, which in turn can only be achieved by including nonlocal absorptive potentials that are also constrained by the high-momentum spectral functions. The resulting proton number is 19.78 which corresponds to about a 1% error that was assigned to this quantity. With a local absorption, we are not capable to either generate a particle number close to 20 or describe the charge density accurately. We reiterate that for local absorptive potential, and the HF term represented in a nonlocal form, it is not possible to obtain a good result for the charge density [3]. We note that the introduction of the gaussian potential that generates a

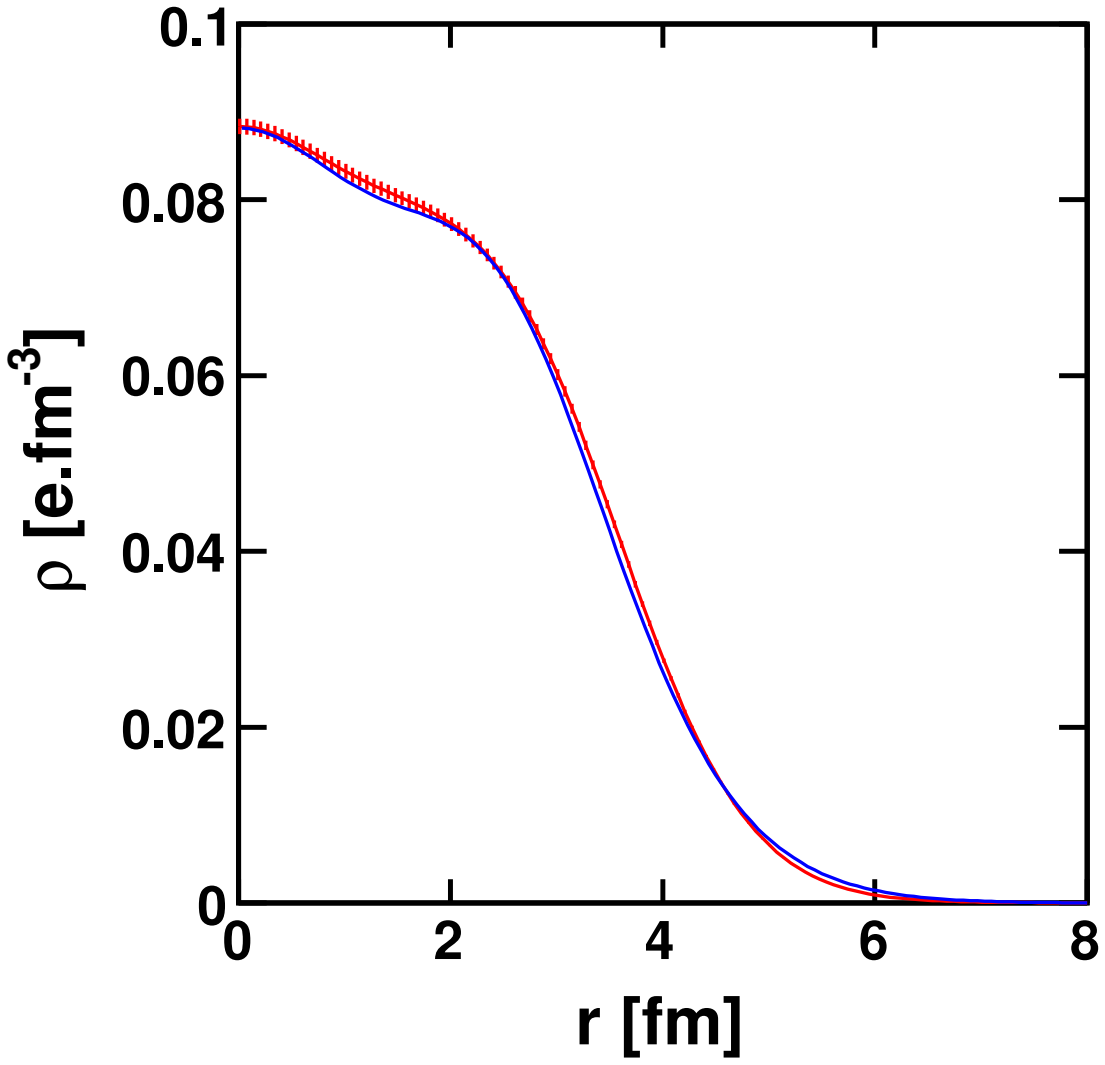

Figure 3.12: Comparison of experimental charge density [28] (thick red hashed line) with the DOM fit (solid blue curve).

wine-bottle shape in the HF term is also helpful in obtaining a correct charge density. This wine-bottle potential was found necessary to describe overlap functions in Ref. [27].

3.5.5 High-momentum components

We compare in Fig. 3.13 the results for the high-momentum removal spectral strength with the Jefferson Lab data [38, 39]. Since the data for Al and Fe per proton are essentially equivalent [39] we have used their average to represent proton removal at high momenta for ^{40}Ca. We note that the high-energy part of the data correspond to intrinsic nucleon excitations and cannot be part of the present analysis. To further improve the description, one would have to introduce an energy dependence of the radial form factors for the potentials. Nevertheless we conclude that an adequate description is generated which corresponds to 10.6 % of the protons having momenta above 1.4 fm^{-1}. The momentum spectral function for a given ℓj is obtained from:

$$S_{\ell j}(k;E) = \frac{2}{\pi^2}\int_0^\infty dr r^2 \int_0^\infty dr' r'^2 \; j_\ell(kr)\; j_\ell(kr')\; \mathfrak{Im}G(r,r';E) \tag{3.17}$$

by employing a double Fourier-Bessel transform of the imaginary part of the propagator expressed in coordinate space. The momentum distribution can be obtained by integrating the momentum spectral function up to the Fermi energy.

$$n_{\ell j}(k) = \int_{-\infty}^{\varepsilon_F} dE\; S_{\ell j}(k;E). \tag{3.18}$$

The total momentum distribution including the degeneracy factors $2j+1$ and weighted by the factor k^2 is plotted in Fig. 3.14 and compared with the momentum distribution of the quasi-hole wave functions of the IPM demonstrating the charactristic tail at high momentum that is not present in the mean-field.

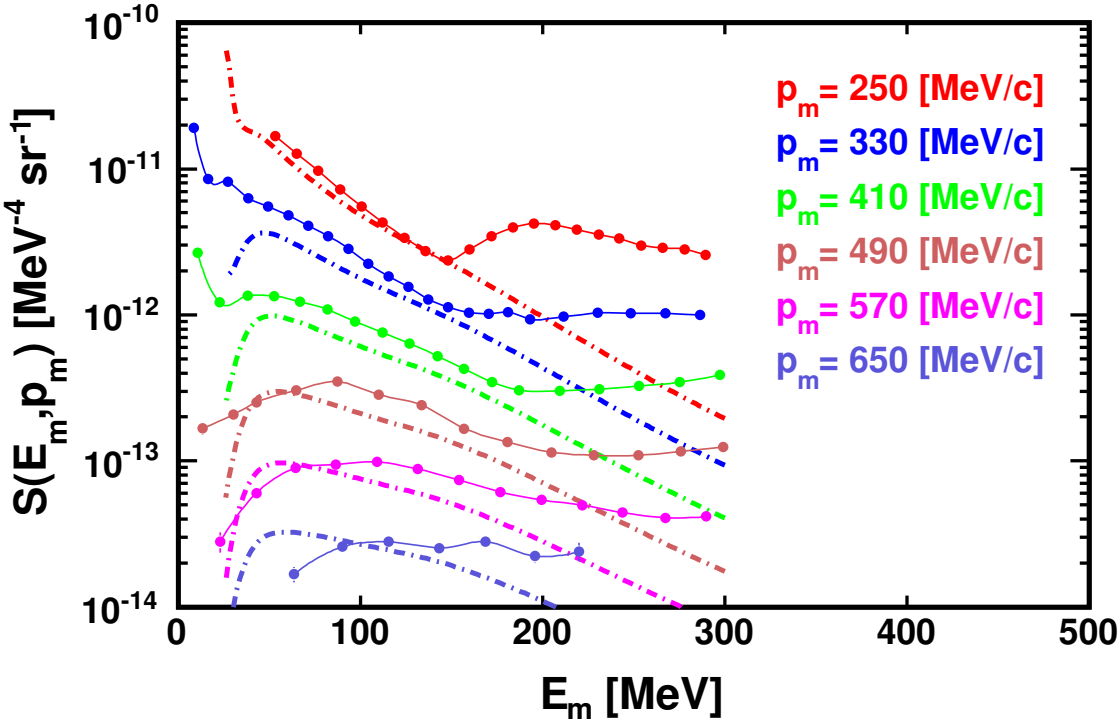

Figure 3.13: Spectral strength as a function of missing energy for different missing momenta as indicated in the figure. The data are the average of the ^{27}Al and ^{56}Fe measurements from Ref. [39] and are represented by solid curves containing full circles. The DOM results are represented by dot-dashed curves.

3.5.6 Binding Energy

The SP propagator allows the calculation of the energy of the ground-state when only two-body interactions are present. Such a calculation using the empirical hole spectral density from the DOM therefore sheds light on the contribution of the three-body interactions to the ground-state energy. It is practical to calculate the energy sum rule in momentum-space. For

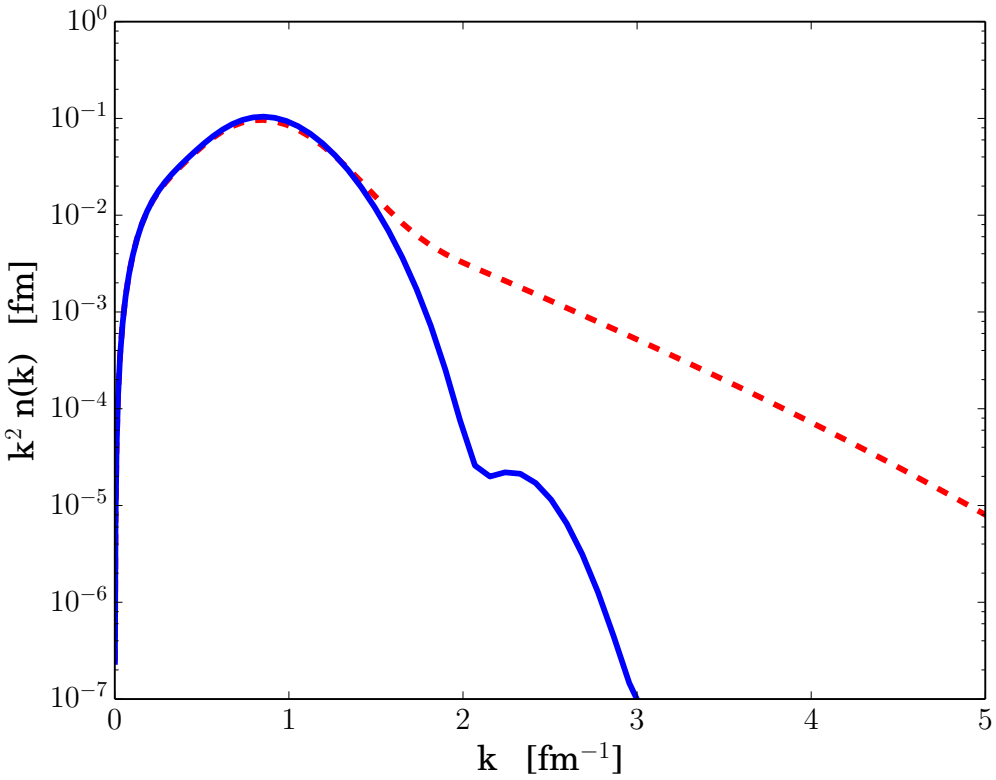

Figure 3.14: Momentum distribution for protons in ^{40}Ca. The red line represents the DOM calculation and the blue line the IPM.

instance the energy per proton of the ground state can be obtained by calculating [10]:

$$\begin{aligned} \frac{E}{Z} &= \frac{1}{2Z}\sum_{\ell j}(2j+1)\int_0^\infty dk\ k^2\frac{k^2}{2m}n_{\ell j}(k) \\ &+ \frac{1}{2Z}\sum_{\ell j}(2j+1)\int_0^\infty dk\ k^2\int_{-\infty}^{\epsilon_F} dE\ E\ S_{\ell j}(k;E). \end{aligned} \tag{3.19}$$

We used the center-of-mass corrected form to evaluate the binding energy per nucleon as in Ref. [40]. This yields a binding energy of 7.91 MeV per nucleon much closer to the experimental 8.55 MeV than the 4.71 MeV found in Ref. [3]. The constrained presence of the high-momentum nucleons is responsible for this change [41]. The 7.91 MeV binding per nucleon obtained here represents the contribution to the ground-state energy from two-body

interactions including a kinetic energy of 22.64 MeV per nucleon and was not part of the fit implying a potential energy contribution of about 30 MeV attraction per particle. This empirical approach therefore leaves about 0.64 MeV per nucleon for higher-body interactions which compares reasonably with the 1.5 MeV per nucleon attraction needed in the Green's function Monte Carlo results of [42] for light nuclei.

3.6 Sum rule

We display in Fig. 3.15 the results of the DOM spectral function as calculated with Eq. (2.81) for the most relevant bound orbits in ^{40}Ca including the hole spectral function of Eq. (2.83). Because the DOM analysis assumes that the imaginary part of the self-energy starts at ε_F, the spectral strength is a continuous function of the energy. The method of solving the Dyson equation for $E < 0$ is very different than that for $E > 0$. The continuity of the curves at $E = 0$ confirms the numerical aspects of both of these calculations. An important sum rule is valid for the sum of the occupation number for the orbit $n_{n\ell j}$ and its depletion number $d_{n\ell j}$ [10]

$$1 = n_{n\ell j} + d_{n\ell j} = \int_{-\infty}^{\varepsilon_F} dE \; S^{n-}_{\ell j}(E) + \int_{\varepsilon_F}^{\infty} dE \; S^{n+}_{\ell j}(E), \tag{3.20}$$

equivalent to $a^\dagger_{n\ell j} a_{n\ell j} + a_{n\ell j} a^\dagger_{n\ell j} = 1$. The average Fermi energy ε_F is given in Eq. (2.20). Strength above ε_F, as expressed by Eq. (2.81), reflects the presence of the imaginary self-energy at positive energies. Without it, the only contribution to the spectral function comes from the elastic channel [42]. The folding in Eq. (2.81) then involves integrals of orthogonal wave functions and yields zero. Because it is essential to describe elastic scattering with an imaginary potential, it automatically ensures that the elastic channel does not exhaust the spectral density and therefore some spectral strength associated with IPM bound orbits

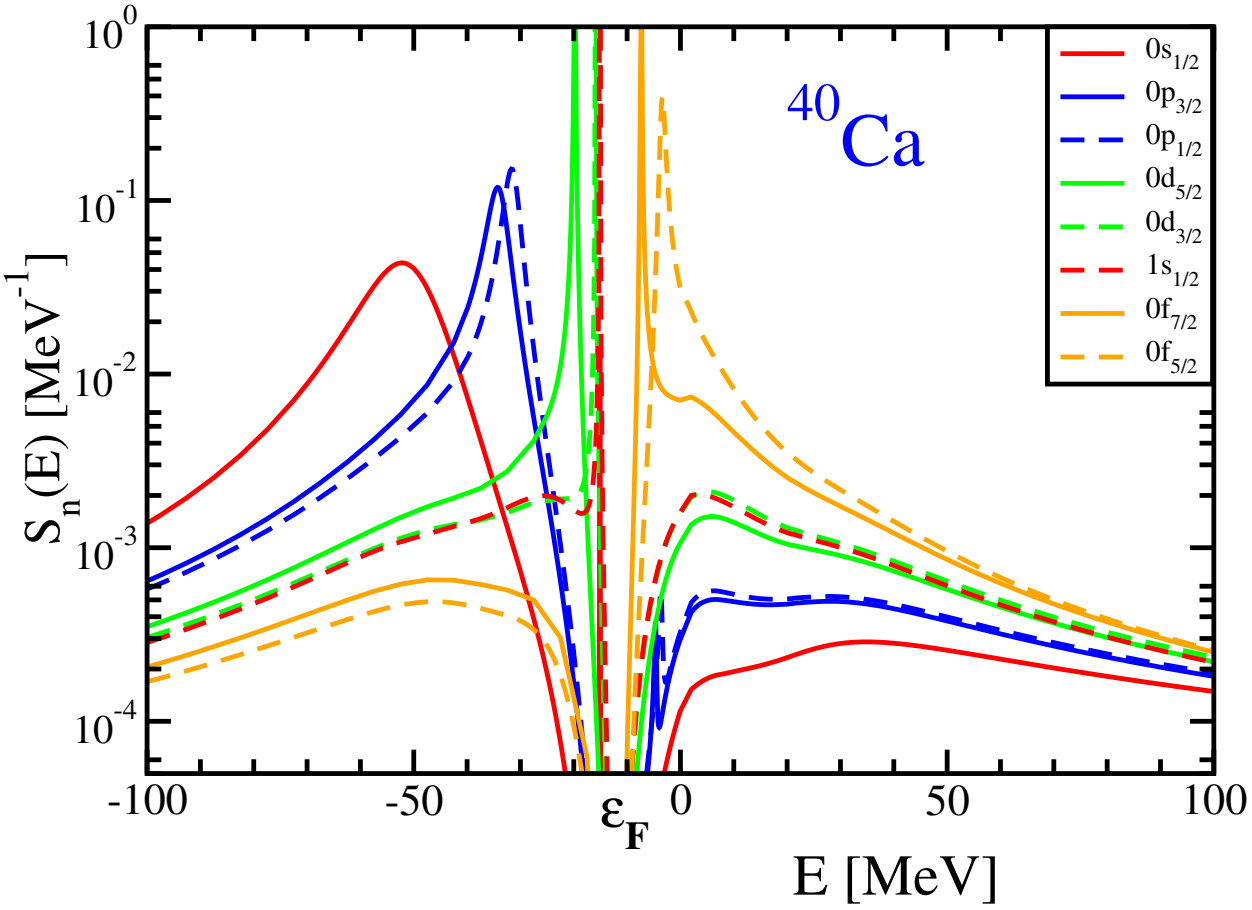

Figure 3.15: Calculated neutron spectral strength, both below and above the Fermi energy, for bound orbits in ^{40}Ca. The spectral strength is constrained by elastic scattering data, level structure, charge density, particle number, and the presence of high-momenta below the Fermi energy [4].

Table 3.2: Occupation and depletion numbers for bound orbits in ^{40}Ca. The $d_{nlj}[0,200]$ depletion numbers have only been integrated from 0 to 200 MeV. The fraction of the sum rule in Eq. (3.20) that is exhausted, is illustrated by $n_{n\ell j} + d_{n\ell j}[\varepsilon_F, 200]$. We also list the $d_{nlj}[0,200]$ depletion numbers for the CDBonn calculation in the last column.

orbit	$n_{n\ell j}$ DOM	$d_{n\ell j}[0,200]$ DOM	$n_{n\ell j} + d_{n\ell j}[\varepsilon_F, 200]$ DOM	$d_{n\ell j}[0,200]$ CDBonn
$0s_{1/2}$	0.926	0.032	0.958	0.035
$0p_{3/2}$	0.914	0.047	0.961	0.036
$1p_{1/2}$	0.906	0.051	0.957	0.038
$0d_{5/2}$	0.883	0.081	0.964	0.040
$1s_{1/2}$	0.871	0.091	0.962	0.038
$0d_{3/2}$	0.859	0.097	0.966	0.041
$0f_{7/2}$	0.046	0.202	0.970	0.034
$0f_{5/2}$	0.036	0.320	0.947	0.036

also occurs in the continuum. Below the Fermi energy, the spectral strength contains peaks associated with the $0s_{1/2}$, $0p_{3/2}, 0p_{1/2}, 0d_{5/2}, 1s_{1/2}$, and $0d_{3/2}$ orbits with narrower peaks for orbits closer to the Fermi energy. Their strength was calculated for the overlap functions associated with the location of the peaks by solving the Dyson equation without the imaginary part but with self-consistency for the energy of the real part [3]. The strength of these orbits above the Fermi energy exhibits systematic features displaying more strength when the IPM energy is closer to the continuum threshold as shown in Fig 3.15 for neutrons and Fig. 3.16 for protons. The proton spectral functions are very similar to those for neutrons except for the shift due to the presence of the Coulomb potential. We make the strength observation quantitative by listing the integrated strength according to the terms of Eq. (3.20) in Table 3.2. For the depletion we integrate from 0 to 200 MeV which corresponds to the energy domain constrained by data in the DOM. We also include the $0f_{7/2}$ and $0f_{5/2}$ spectral functions in Fig. 3.15 and corresponding results in Table 3.2 noting that the strength in the continuum from 0 to 200 MeV further rises to 0.202 and 0.320, respectively. From ε_F to 0

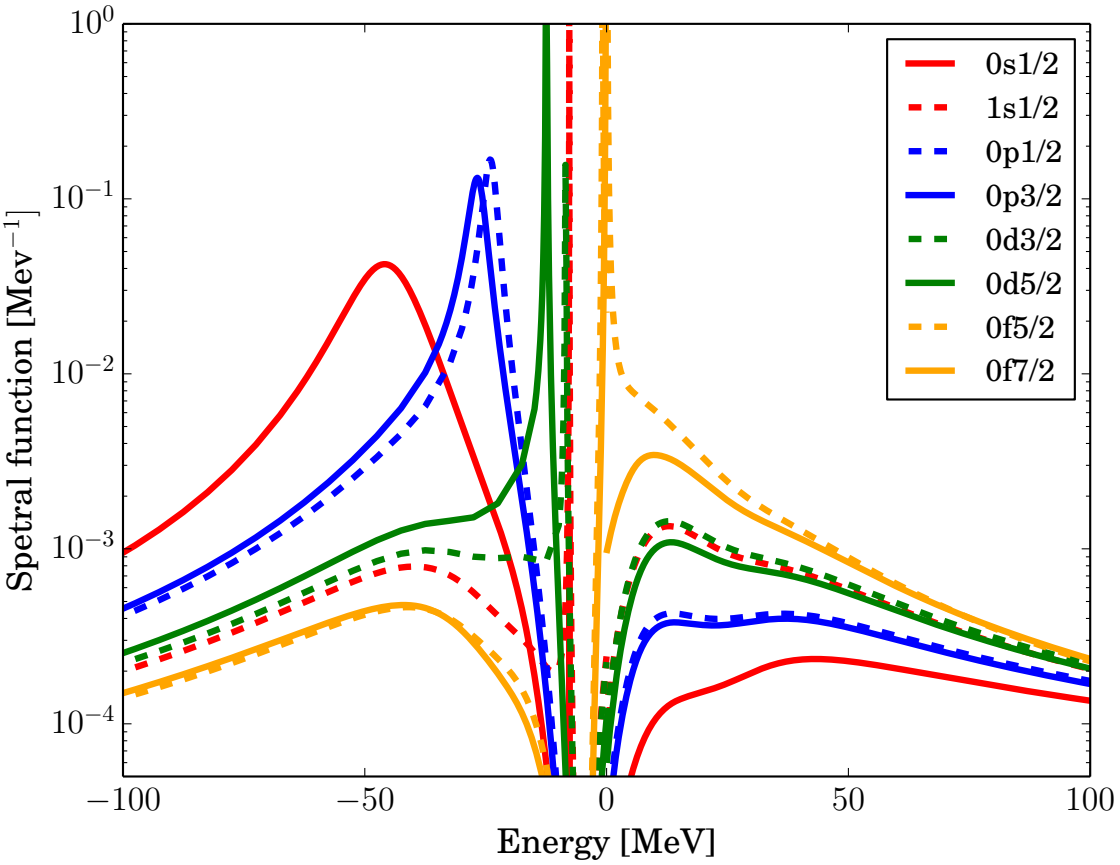

Figure 3.16: Calculated proton spectral strength from a momentum space calculation with a screened Coulomb potential both below and above the Fermi energy, for bound orbits in ^{40}Ca. The spectral strength is constrained the corresponding elastic scattering data as the results in Fig. 3.15.

the strength for these states is also included in the sum and decreases from 0.722 to 0.591, respectively. This illustrates that there is a dramatic increase of strength into the continuum when the IPM energy approaches this threshold. Such orbits correspond to valence states in exotic nuclei [43, 44, 45]. The $1p_{3/2}$ and $1p_{1/2}$ spectral functions are not shown as they mimic the behavior of the $0f_{7/2}$ distribution but their presence causes the wiggles in the $0p_{3/2}$ and $0p_{1/2}$ spectral functions due to slight nonorthogonality. This sensitivity to the separation from the continuum is associated with the pronounced surface absorption necessary to describe the elastic-scattering data in this energy range. At higher energies, volume absorption dominates and the strengths of the different orbits become similar as illustrated in Fig. 3.17 [17]. This figure also includes the CDBonn predictions which highlight the notion that SRC predominantly impact higher energies [46]. While the CDBonn spectral functions are above the DOM results for energies larger than 100 MeV, it is quite likely that a somewhat harder interaction like Argonne V18 [47] would move some of this excess strength to higher energy [48]. The fraction of the sum rule of Eq. (3.20) for the DOM in Table 3.2 indicates that a few percent of the strength occurs at energies higher than 200 MeV [17]. Theoretical work associates such strength with SRC [49]. No surface absorption is present in the microscopic CDBonn results and their depletions in Table 3.2 correspond to a uniform strength distribution for all orbits consistent with the SRC interpretation as illustrated in Fig. 3.17.

3.7 Volume Integrals

In studying optical potentials, investigating the volume integral of real and imaginary potentials is found to be useful. Although there is no unique fit for the self-energy in the standard optical-model description, it turns out that volume integrals of the imaginary potential of good fits are very similar [50]. In the case of the nonlocal DOM, the self-energy depends

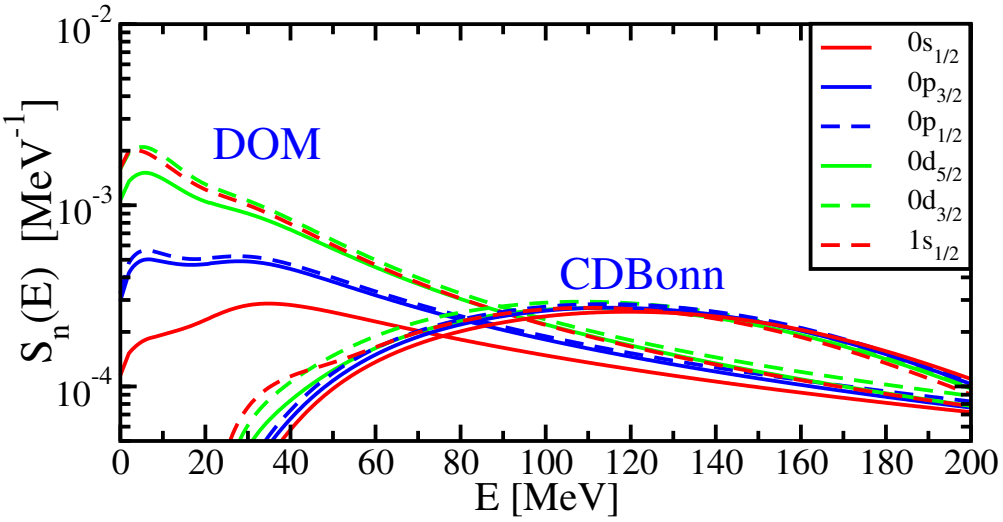

Figure 3.17: Calculated spectral strength for mostly occupied orbits in ^{40}Ca from 0 to 200 MeV. The CDBonn spectral functions exhibit mainly volume absorption.

on the angular momentum ℓ, so the contributions $\Sigma^{\ell j}(r, r')$ can be studied and compared to ab initio calculations such as Faddeev random phase approximation (FRPA) [25] and the treatment of SRCs using the CDBonn interaction [17]. The plots in this section show volume integrals as a function of energy with respect to the relevant Fermi energy.

The FRPA is a microscopic implementation of the Green's function method that incorporates the low-energy or long-range correlations because only a finite size model space can be treated. In this formalism the nucleons couple to low-lying collective states and giant resonances [51, 52, 34]. First we compare the DOM volume integrals with the corresponding FRPA results for ^{40}Ca. We exclude the spin-orbit contribution by averaging it out [25] and present only the volume integrals of the central part, $\Sigma_0^{\ell}(r, r')$ of the self-energy. These

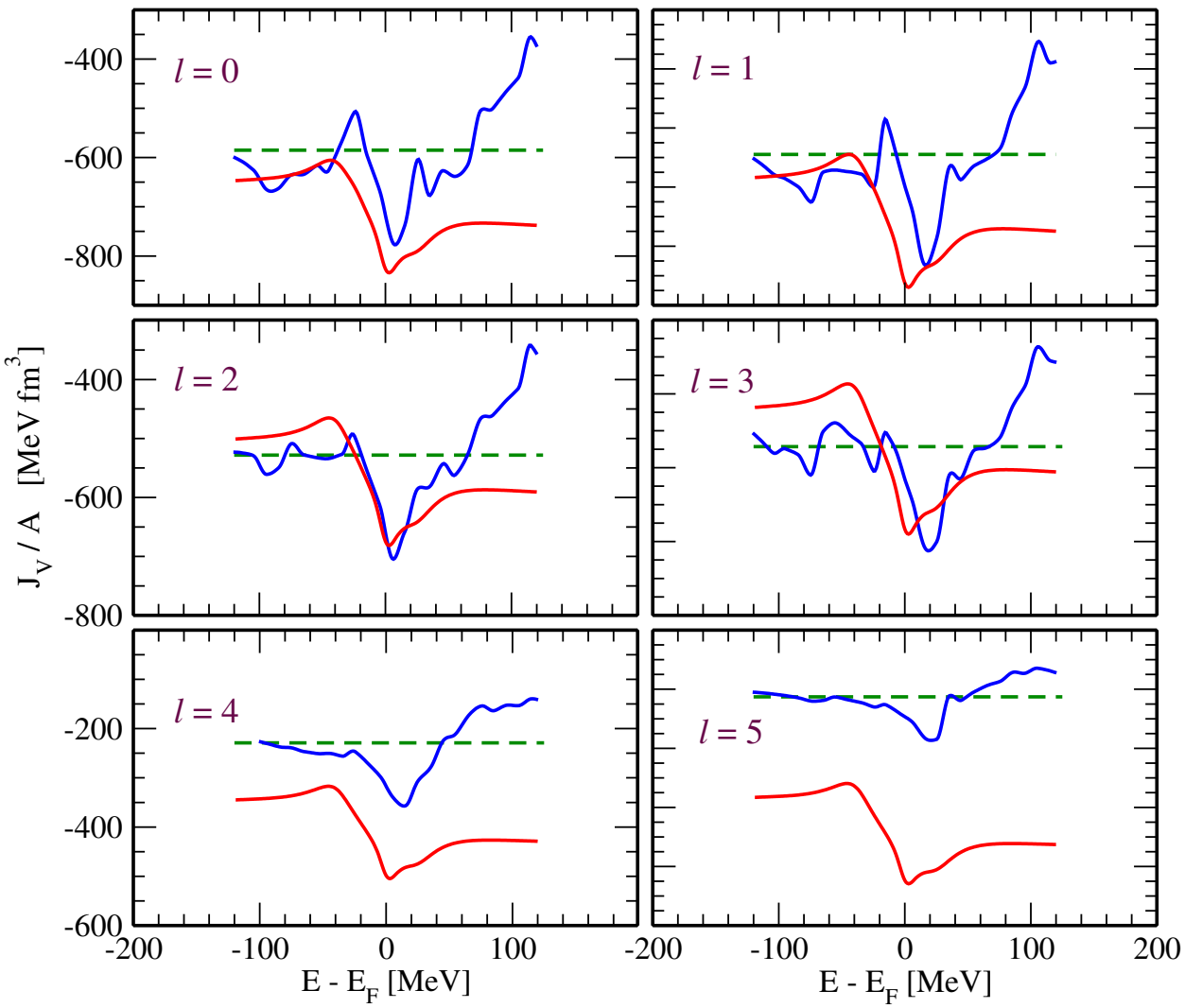

Figure 3.18: Comparison of the real part of the volume integral of the potential for FRPA (blue curves) and nonlocal DOM (red curves) calculations. The horizontal dashed green line represents the static contribution of the FRPA self-energy.

volume integrals are given by:

$$J_W^\ell(E) = 4\pi \int dr r^2 \int dr' r'^2 \, \mathfrak{Im}\Sigma_0^\ell(r, r'; E) \tag{3.21}$$

$$J_V^\ell(E) = 4\pi \int dr r^2 \int dr' r'^2 \, \mathfrak{Re}\Sigma_0^\ell(r, r'; E). \tag{3.22}$$

In Fig. 3.18 the real volume integral for different partial waves up to $\ell = 5$ is plotted. The solid red lines represent the nonlocal DOM results and the blue lines indicate the FRPA results [25]. As indicated in Fig. 3.18 there is a reduction in the magnitude of the real volume integral for higher ℓ's for both calculations. In the case of the FRPA calculations there is a larger reduction of the magnitude for higher partial waves that can be explained by the truncated model space. The agreement for the smaller ℓ values appears to be reasonable for energies near the Fermi energy. The rise of the FRPA calculations with energy is also due to the limited phase space because the accompanying imaginary part has a limited energy domain (see Fig. 3.19). In the DOM calculation this rise takes place at much higher energy because the complete phase space is taken into account. In Fig. 3.19 the volume integral of the imaginary part of the potential is compared for the FRPA and DOM. FRPA microscopic calculations emphasize the coupling to surface excitations and do not include absorption at higher energies associated with volume physics as shown in Fig. 3.19. The negative energy tail of the DOM calculation is attributed to the presence of high momenta which constrain this part of the self-energy and are also not included in FRPA calculations. The volume integral for small ℓ values in Fig. 3.19 compare reasonably well near the Fermi energy while larger differences occur at higher energies and larger values of orbital angular momentum.

In Fig. 3.20 the volume integral of the nonlocal DOM imaginary potentials and CDBonn [17] are compared for different ℓ. The CDBonn calculations emphasize SRCs and do not represents surface absorption as illustrated in Fig. 3.20. At large positive energies CDBonn results

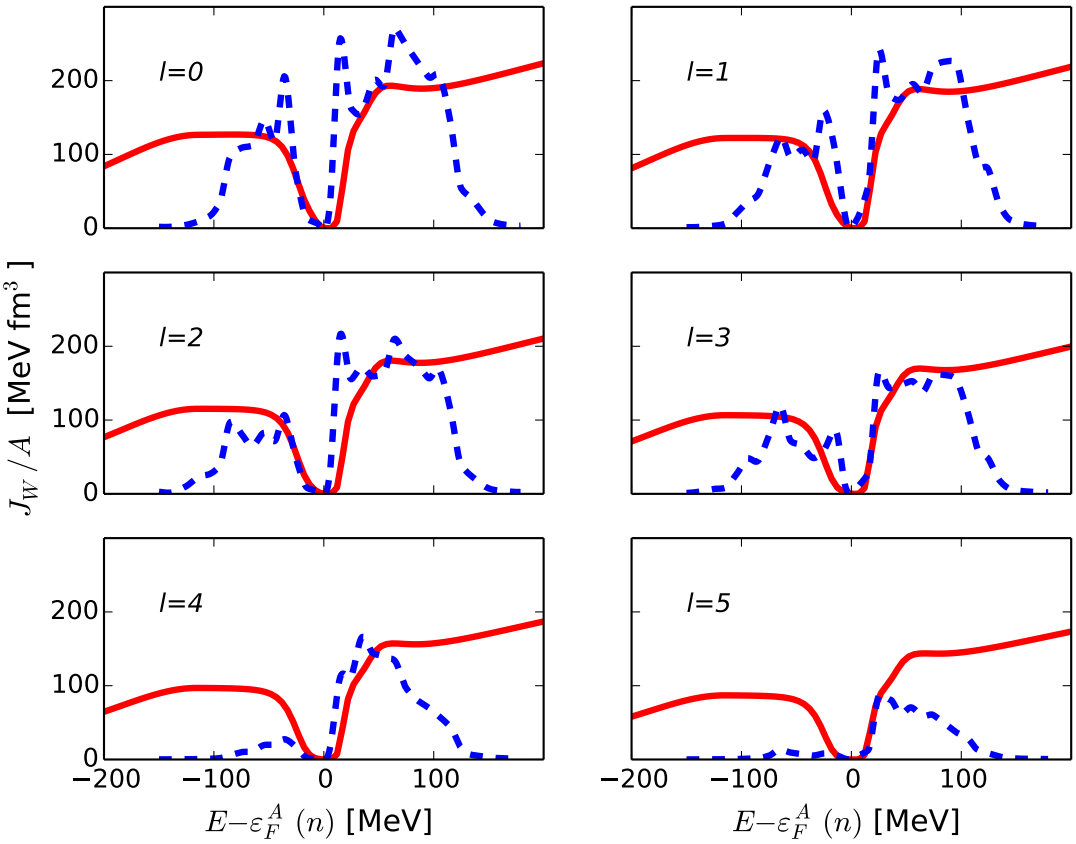

Figure 3.19: Comparison of the imaginary part of the potential volume integral for FRPA (dashed blue curves) and nonlocal DOM (red curves) calculations.

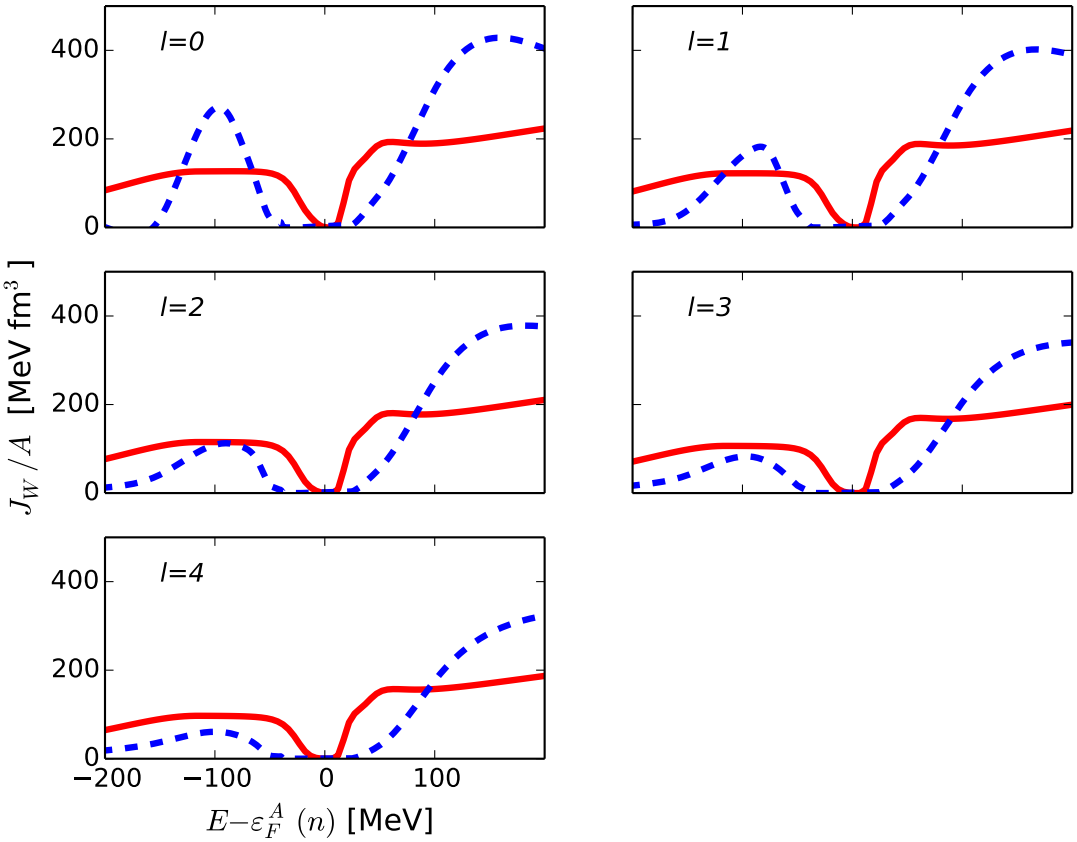

Figure 3.20: Comparison of the imaginary volume integral of the potential for the nonlocal DOM (red curve) and CDBonn (dashed blue curve) calculations.

exhibit more volume absorption than DOM calculations. The latter feature is also reflected in the corresponding spectral strength distribution shown in Fig. 3.17. At negative energies the CDBonn volume integrals vanish more rapidly than the DOM calculations which reflects the naive treatment of the two-hole-one-particle intermediate states in the calculation of the self-energy in Ref. [17].

Unlike the local DOM self-energy the nonlocal DOM implementation generates volume integrals that depend on angular momentum. This is illustrated in Fig. 3.21 for the real and

Fig. 3.22 for the imaginary part where a comparison with ℓ-independent volume integral of Ref. [16] is made. In the local DOM the nonlocality of the HF self-energy is replaced by a spurious linear energy dependence term at negative energies which is reflected in Fig. 3.21. Around the Fermi energy the local DOM appears to represent an average of the nonlocal DOM volume integrals for lower ℓ values. At higher energies a similar result occurs but involves higher ℓ values. In the local DOM prescription the HF term is given by:

$$\mathcal{V}_{HF}(r;E) = V_{HF}(E) f(r, a_{HF}, R_{HF}), \tag{3.23}$$

where the energy dependence mimics the effect of treating nonlocality [2]. The energy derivative of $\mathcal{V}_{HF}$ is a measure of that nonlocality which is related to the momentum-dependent effective mass [2]:

$$\frac{\tilde{m}(r;E)}{m} = 1 - \frac{\partial}{\partial E}\mathcal{V}_{HF}(r;E). \tag{3.24}$$

To compare local DOM potentials with a nonlocal self-energy it is necessary to correct for this treatment of nonlocality [3, 2] by employing the following equation:

$$\mathcal{W} = \frac{\tilde{m}(r;E)}{m}\ \mathfrak{Im}\Sigma. \tag{3.25}$$

In other words, to compare the calculated volume integral in the nonlocal DOM as in Figs. 3.18 and 3.19 with the local version, the factor $m/\tilde{m}$ must be taken into account. For the interior region of nuclei this factor is approximately 2 [26]. In Fig. 3.22 the local imaginary potential volume integral is plotted with and without this effective mass correction. The local DOM calculation below the Fermi energy (the solid yellow curve in Fig. 3.22) shows larger absorption than the nonlocal one which is associated with the assumption of a symmetric treatment of the surface absorption in that calculation [26] which has been abandoned in the nonlocal DOM.

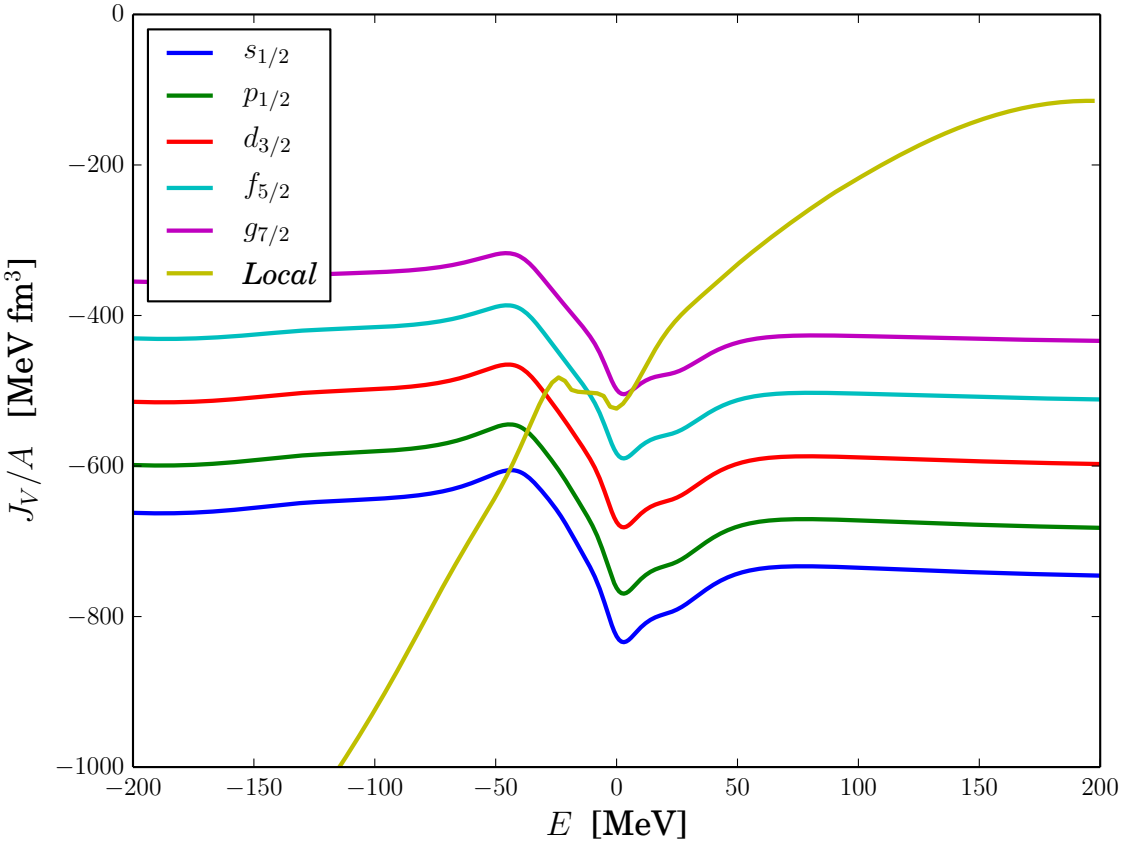

Figure 3.21: Comparing the real part of the potential for local DOM (yellow curve) and nonlocal DOM (colored curves for $\ell = 0$ to 4) calculations.

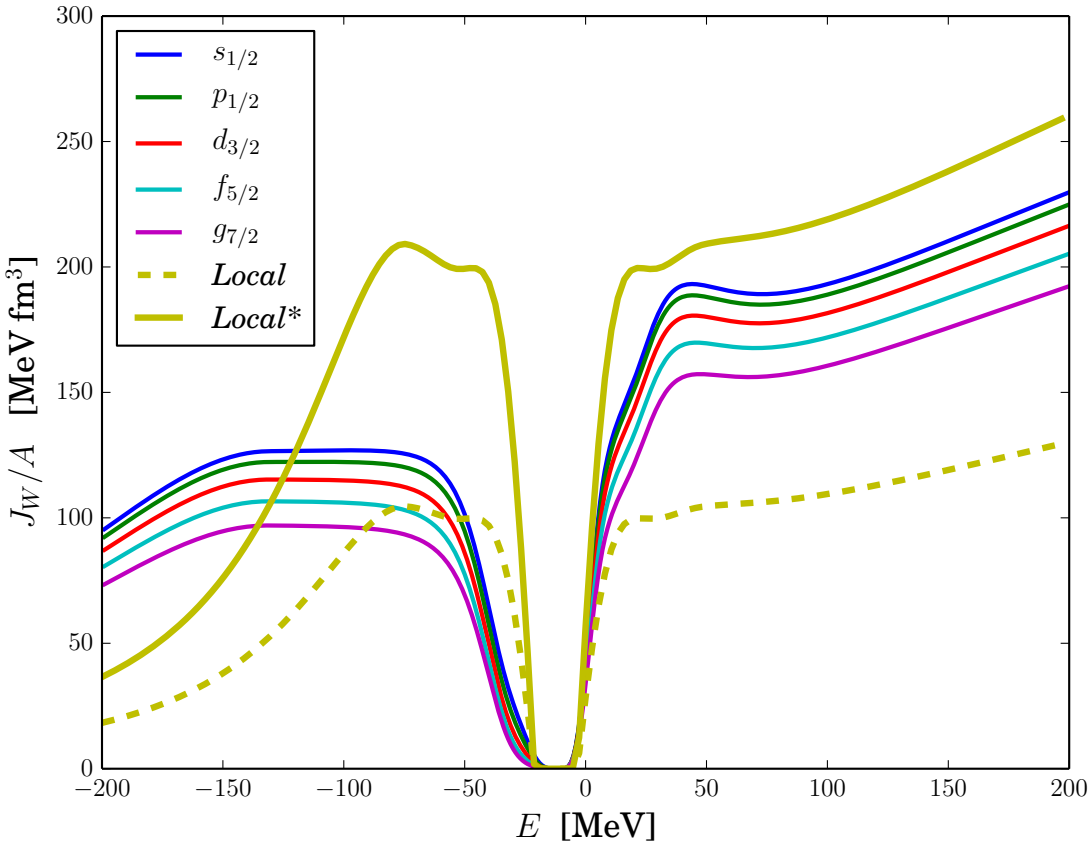

Figure 3.22: Local (dashed yellow and yellow curves, the solid yellow curve calculated including the mass correction) and the nonlocal DOM (for $\ell = 0$ to 4) imaginary potential volume integrals.

The neutron quasi-particle wave functions for $0d_{3/2}$ and $1s_{1/2}$ are compared for the nonlocal and local DOM in Figs. 3.23 and 3.24. As one expects the bound-state wave functions are rather similar especially for the $0d_{3/2}$. The $1s_{1/2}$ with one node exhibits a stronger surface component compared to the local one which was already discussed in the analysis of the transfer reactions in Ref. [37].

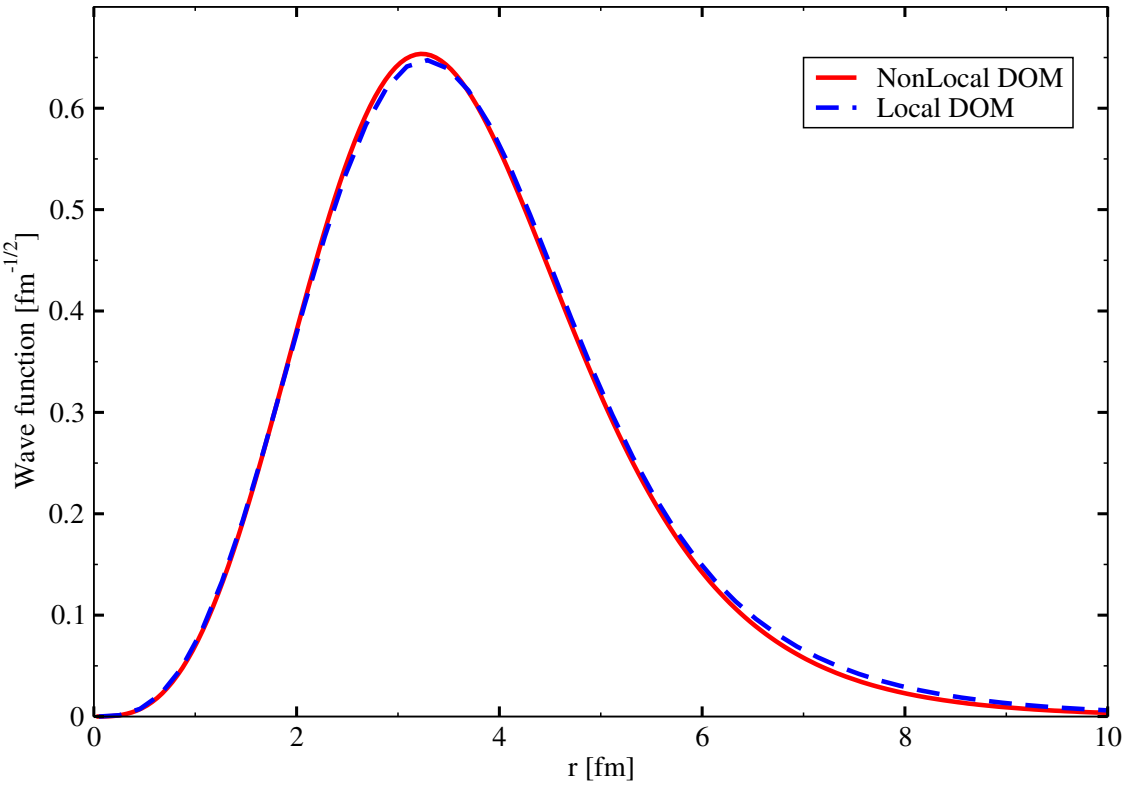

Figure 3.23: Comparison of ^{40}Ca bound-state wave function $d_{3/2}$ multiplied by r for local (dashed blue curve) and nonlocal (red curve) DOM calculations.

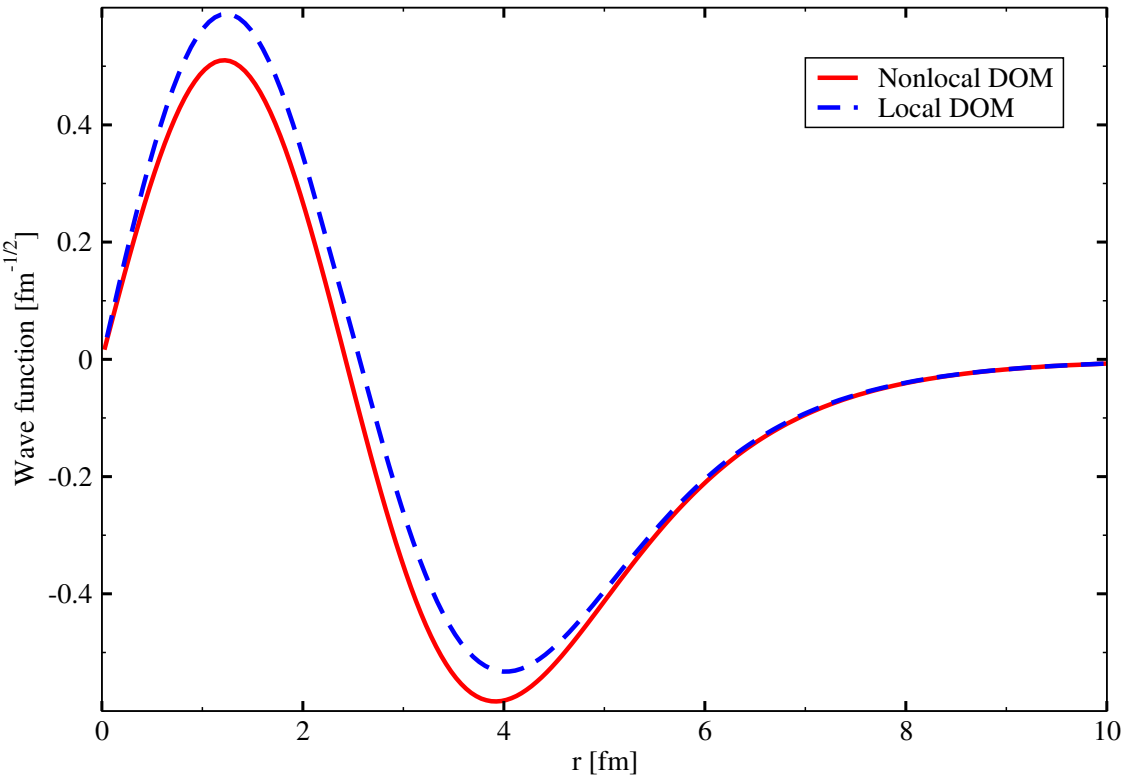

Figure 3.24: Comparison of ^{40}Ca bound-state wavefunction multiplied by r for the second $s_{1/2}$ for local (dashed blue curve) and nonlocal (red curve) DOM calculations.

4 Calcium Forty-eight

4.1 Introduction

There is a considerable interest, some of which is astrophysical, in studying nuclei with a large difference in neutron and proton number. Such nuclei can be studied at rare isotope facilities like FRIB at MSU. In the sequence of calcium isotopes both ^{40}Ca and ^{48}Ca are considered double closed-shell nuclei. It is therefore possible to apply the DOM to both these nuclei simultaneously [20, 26, 16]. Such a fit allows for predictions of nuclei towards the drip line by a suitable extrapolation from the fit to ^{40}Ca and ^{48}Ca. In addition by establishing the $N - Z$ dependency of the potential from the results of ^{48}Ca it becomes possible to make predictions for neutron properties in the ground state of ^{48}Ca including the neutron skin. It is therefore essential to implement a nonlocal version of the DOM for this neutron-rich system. We also note that it has been hard to fit elastic neutron scattering data on ^{48}Ca with the local version of the DOM [16]. One of the most significant consequences of studying and developing the self-energy for ^{48}Ca is therefore extracting information about the neutron distribution by calculating the neutron skin. This distribution impacts the number of nuclei that can exist and the size of neutron stars [53].

In this chapter we apply the nonlocal DOM to ^{48}Ca. Building the self-energy for the new isotope, we started from the ^{40}Ca self-energy and included asymmetry terms in the potential. Although there are eight neutrons added to ^{40}Ca, the charge density radius for protons of ^{48}Ca is the same as for ^{40}Ca [28] (unlike the intermediate isotopes which have slightly larger charge radii). To obtain the appropriate self-energy that can describe the available data, we initiate the procedure by employing the well-constrained self-energy for ^{40}Ca obtained in the previous chapter. All those parameters are kept fixed except the radii for different terms in the self-energy because the increase with $A^{1/3}$ growth in the nuclear radius is not a premise. Moreover the asymmetry term which carries $N-Z$ dependence is included in different terms of the potential. The parametrized self-energy is then constrained to represent the available data at positive and negative energies. At negative energies, particle number, quasi-particle energy levels and charge density were incorporated to constrain the self-energy. At energies above the Fermi energy the available data for the total, elastic scattering cross section and analyzing power for protons and neutrons were adopted to determine the self-energy parameters through a similar fit process as for ^{40}Ca.

4.2 Parametrization of the potentials for ^{48}Ca

In the case of ^{48}Ca the asymmetry factor $(N-Z)/A$ is included as follows for the HF term:

$$\begin{aligned} V_{HF}^{vol}\left(\boldsymbol{r},\boldsymbol{r'}\right) &= V_{HF}^{0} f\left(\tilde{r}, r^{HF}, a^{HF}\right) \times \left[x_1 H\left(\boldsymbol{s};\beta_{vol_1}\right) + (1-x_1) H\left(\boldsymbol{s};\beta_{vol_2}\right)\right] \\ &\pm \alpha_{HF(p,n)}^{asym} \times \frac{N-Z}{A} f\left(\tilde{r}, r_{asym}^{HF(p,n)}, a_{asym}^{HF}\right) \\ &\times \left[x_1 H\left(\boldsymbol{s};\beta_{vol_1(p,n)}^{asym}\right) + (1-x_1) H\left(\boldsymbol{s};\beta_{vol_2(p,n)}^{asym}\right)\right], \end{aligned} \tag{4.1}$$

where the contribution of the first line of Eq. (4.1) is taken from Ref. [4]. The asymmetry parameters $\alpha^{asym}_{HF(p,n)}, r^{HF(p,n)}_{asym}, a^{HF}_{asym}, \beta^{asym}_{vol_1(p,n)}$ and $\beta^{asym}_{vol_2(p,n)}$ are given in B.1 of App. B. For the spin-orbit potential we employ a local form which is similar to what is implemented in [16]:

$$V^{so}(r) = \left(\frac{\hbar}{m_\pi c}\right)^2 \times \left(V_0^{so} \pm V_{NZ}^{so(p,n)} \times \frac{N-Z}{A}\right) \times \frac{1}{r}\frac{d}{dr} f(r, r^{so}, a^{so})\ \vec{\ell}\cdot\vec{\sigma}. \tag{4.2}$$

For the imaginary part of the self-energy we add an asymmetry contribution to the original surface potential with the same form with different parameters that are given in B.2 of App. B:

$$\begin{aligned} W^{sur(p,n)}_{asym\pm}(E) &= \omega_4\left(E, A^{sur(p,n)}_{asym\pm}, B^{sur(p,n)}_{asym\pm s1}, 0\right) \\ &- \omega_2\left(E, A^{sur(p,n)}_{asym\pm}, B^{sur(p,n)}_{asym\pm s2}, C^{sur(p,n)}_{asym\pm}\right) \end{aligned} \tag{4.3}$$

where A^{sur} in Eq. (3.11) is changed to:

$$A^{sur(p,n)}_{asym\pm} \times \frac{N-Z}{A}. \tag{4.4}$$

The imaginary volume part of the potential is modified to:

$$\begin{aligned} W^{vol}_{0\pm}(E) &= \Delta W^{\pm}_{NM}(E) \\ &+ \begin{cases} 0 & \text{if } |E-\varepsilon_F| < E^{vol}_{p\pm} \\ \left(A^{vol}_{\pm} \pm C^{vol(p,n)}_{asym} \times \frac{N-Z}{A}\right) \frac{\left(|E-\varepsilon_F| - E^{vol}_{p\pm}\right)^4}{\left(|E-\varepsilon_F| - E^{vol}_{p\pm}\right)^4 + (B^{vol}_{\pm})^4} & \text{if } |E-\varepsilon_F| > E^{vol}_{p\pm}, \end{cases} \end{aligned} \tag{4.5}$$

with the corresponding change for the Eq. (3.9):

$$\Delta W^{\pm}_{NM}(E) = \tag{4.6}$$

$$\begin{cases} \alpha\left(A^{vol}_{+} \pm C^{vol(p,n)}_{asym} \times \frac{N-Z}{A}\right)\left[\sqrt{E} + \frac{\left(\varepsilon_F + E^{+}_{a}\right)^{3/2}}{2E} - \frac{3}{2}\sqrt{\varepsilon_F + E^{+}_{a}}\right] & \text{for } E - \varepsilon_F > E^{+}_{a} \\ -\left(A^{vol}_{-} \pm C^{vol(p,n)}_{asym} \times \frac{N-Z}{A}\right)\frac{(\varepsilon_F - E - E^{-}_{a})^2}{(\varepsilon_F - E - E^{-}_{a})^2 + (E^{-}_{a})^2} & \text{for } E - \varepsilon_F < -E^{-}_{a} \\ 0 & \text{otherwise.} \end{cases}$$

The imaginary part of the self-energy including the above consideration will have the following form:

$$\begin{aligned} \mathfrak{Im}\ \Sigma^{nl}(\boldsymbol{r}, \boldsymbol{r}'; E) = & - W^{vol}_{0\pm}(E) f\left(\tilde{r}; r^{vol}_{\pm}; a^{vol}_{\pm}\right) H\left(\boldsymbol{s}; \beta^{\pm}_{vol}\right) \\ & + 4a^{sur}_{\pm} W^{sur}_{\pm}(E)\, H\left(\boldsymbol{s}; \beta^{\pm}_{sur}\right) \frac{d}{d\tilde{r}} f(\tilde{r}, r^{sur}_{\pm}, a^{sur}), \\ & + 4a^{sur}_{\pm} W^{sur(p,n)}_{asym\pm}(E)\, H\left(\boldsymbol{s}; \beta^{asym\pm}_{sur(p,n)}\right) \frac{d}{d\tilde{r}} f(\tilde{r}, r^{sur(p,n)}_{asym\pm}, a^{sur}). \end{aligned} \tag{4.7}$$

4.3 Parameters for ^{48}Ca

The constraint of the number of particles was incorporated to include contributions from $\ell = 0$ to 5. Such a range of ℓ-values generates a sensible convergence with ℓ when short-range correlations are included as in Ref. [17]. We obtain a total number of 27.9 neutrons summing from $\ell = 0$ to 5 partial wave terms including $j = \ell \pm \frac{1}{2}$ and 19.8 for the number of protons. This is within the error we assigned to the particle number of about 1%. If in the future higher ℓ-values are included, we expect a slight change in the fitted parameters.

The HF parameters are shown in Table B.1. The corresponding equations where these parameters are introduced have also been listed in this table. The spin-orbit parameters are

also gathered in Table B.1.

The parameters pertaining to volume absorption are displayed in Table B.1. Motivated by the theoretical work of Refs. [25, 17], we allow for different nonlocalities above and below the Fermi energy in the asymmetry terms. While we obtain small differences for the radii parameters other parameters show very minor differences and could have been kept identical above and below the Fermi energy in the fit. Surface absorption parameters are collected in Table B.2.

4.4 Elastic scattering cross sections

Unlike for ^{40}Ca there are few experimental data available for neutron elastic scattering for ^{48}Ca. Two new data sets were recently acquired at the Triangle Universities Nuclear facility [16]. In Fig. 4.1 calculated reaction cross sections for proton and the experimental data are plotted. The nonlocal DOM total and reaction cross sections for neutrons are also plotted in the bottom part of Fig. 4.1. Total neutron cross sections were recently measured and reported in Refs [16, 54]. Employing the nonlocal DOM made it possible to generate the total and elastic scattering cross sections consistent with data. Because ^{40}Ca and ^{48}Ca were not simultaneously fit, we find that the ratio of the difference of the total cross sections to their sum is somewhat overestimated compared to the data of Ref. [54]. Judging from Fig. 3.2 a slight increase of the ^{40}Ca total cross section centered around 50 MeV would lead to a good agreement. In Fig. 4.2 the elastic scattering data for protons and neutrons in ^{48}Ca are shown together with nonlocal DOM fits. In Fig. 4.2 the angular distributions for protons for ^{48}Ca for the nonlocal DOM are of the same quality as the local calculations [20, 26, 16]. The elastic scattering for neutrons fitted using the nonlocal DOM potential exhibits an improved overlap with experimental data as one can see in Fig 4.3. The neutron scattering data

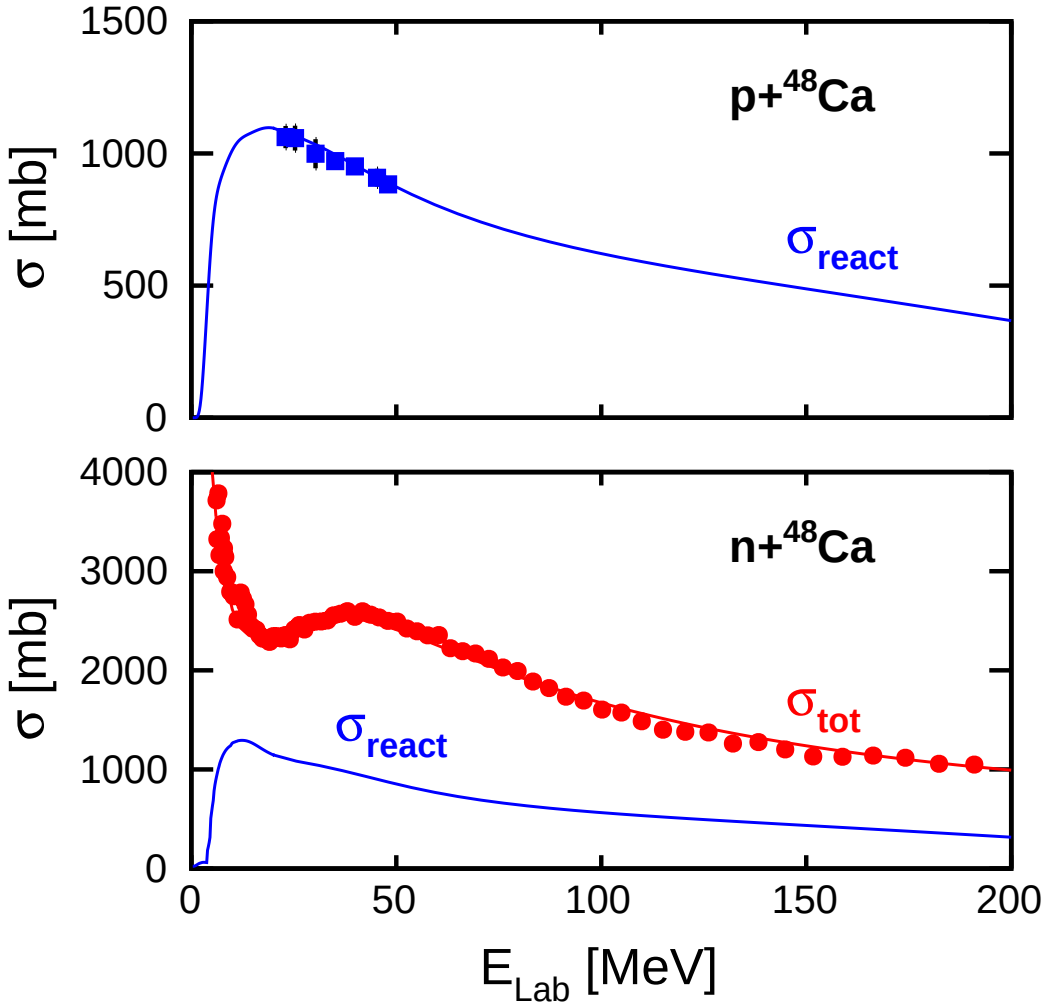

Figure 4.1: Total reaction cross sections are displayed as a function of proton energy while both total and reaction cross sections are shown for neutrons.

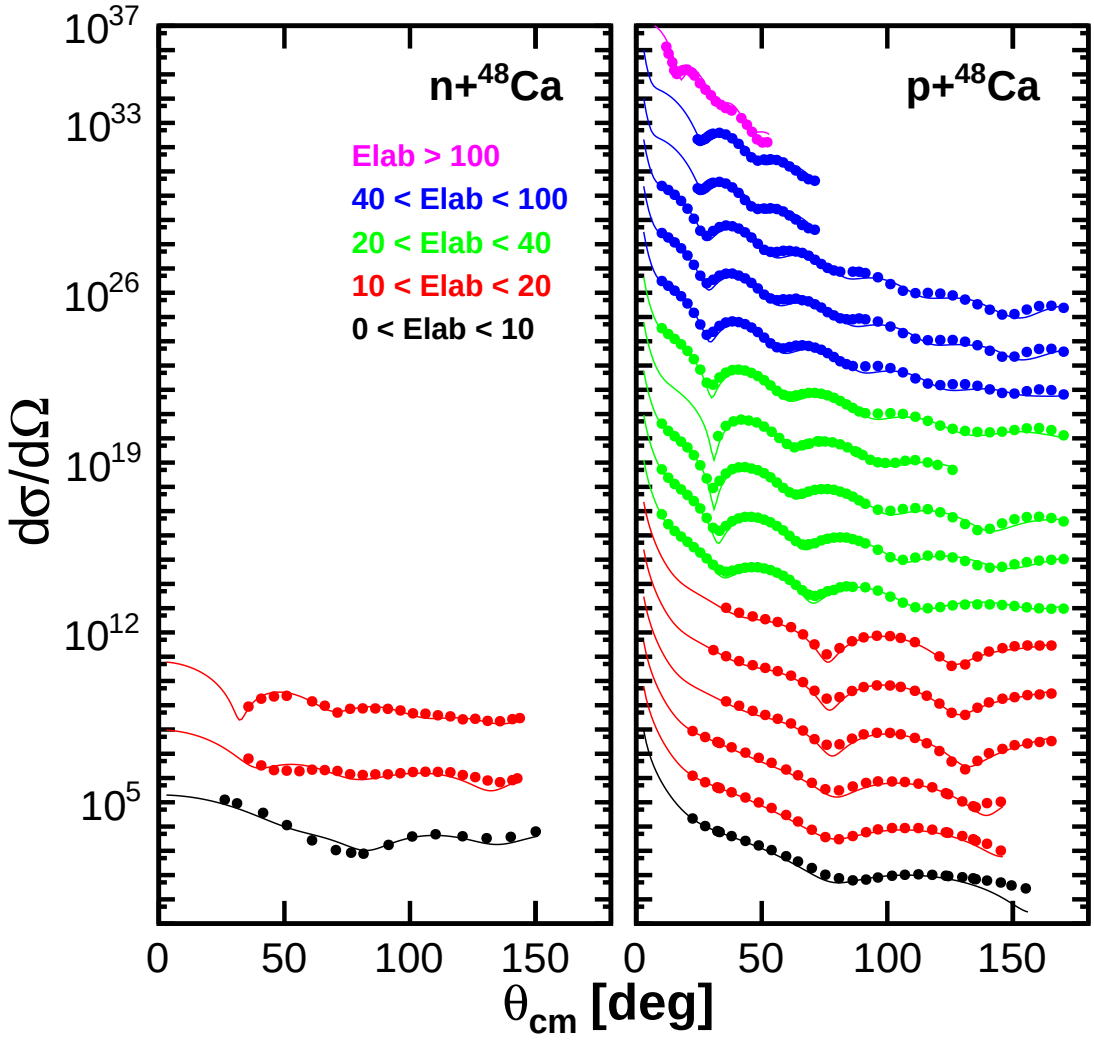

Figure 4.2: Calculated and experimental elastic- scattering angular distributions of the differential cross section. Panels shows results for n+^{48}Ca and p+^{48}Ca. Data for each energy are offset for clarity with the lowest energy at the bottom and highest at the top of each frame. References to the data are given in Ref. [16].

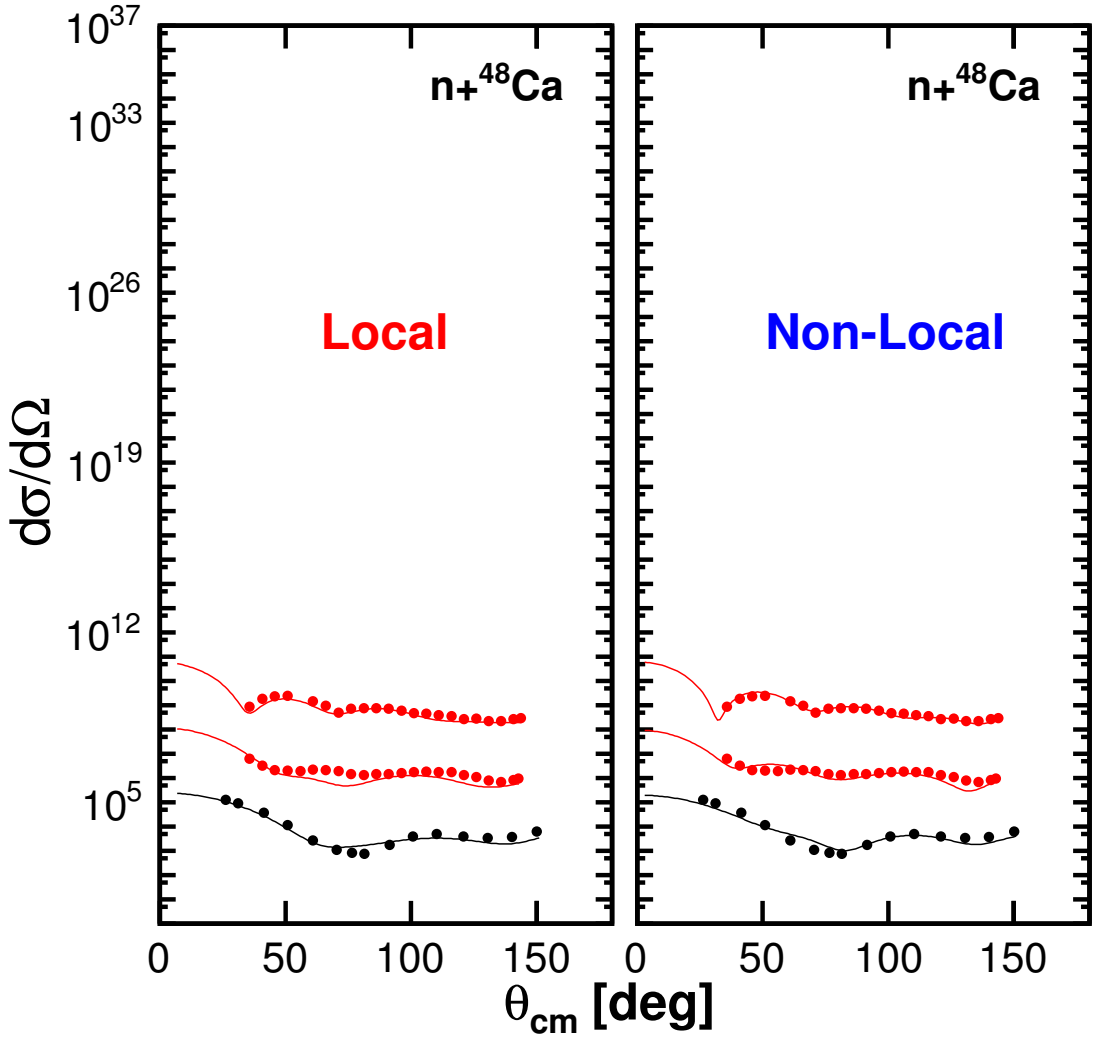

Figure 4.3: Comparison of the local (on the left) and nonlocal (on the right) DOM fit for neutron angular distributions on ^{48}Ca.

were not well represented by local version of DOM, and further flexibility of the nonlocal potential provides a better description of the experimental data. In Fig. 4.4 the nonlocal DOM fit and experimental data for analyzing powers for protons are plotted. The nonlocal DOM fit for proton analyzing power is also of the same quality as the local DOM calculations in [20, 26, 16].

4.5 Charge density of ^{48}Ca

Comparing ^{48}Ca with ^{40}Ca, one realizes that the experimental charge density radius is not obeying the $A^{1/3}$ law. Specifically $(40/48)^{1/3}$ is about 0.94 whereas the experimental charge density ratio 3.48/3.51 is 0.99 [28]. It illustrates the complicated nature of the correlations inside the nucleus. In Fig 4.5 the folded charge density calculated using the nonlocal DOM self-energy, as well as experimental charge density are plotted. As we see the two charge distribution curves are consistent and give rise to the same proton number and charge density radius. The saturation density of nuclear matter ρ_0 is usually inferred from the interior charge distribution of heavier nuclei as obtained from elastic electron scattering. This density corresponds to a Fermi moment of about 1.33 fm^{-1} if the experimental charge distribution at the origin in ^{208}Pb is multiplied by A/Z. For $N \neq Z$ nuclei it is therefore of critical importance to know the neutron distribution which is also shown in Fig. 4.5 together with the weak charge distribution.

One of the important quantities that improves our understanding of the nuclear structure of a heavy nucleus is played by this saturation density of nuclear matter ρ_0 which is closely related to the size of the nucleus. Thus an accurate measurement of the neutron distribution rms radius R_n can give us a better understanding of ρ_0 and the relevant properties. A clean experimental method to determine the distribution of neutrons is by a parity-violating

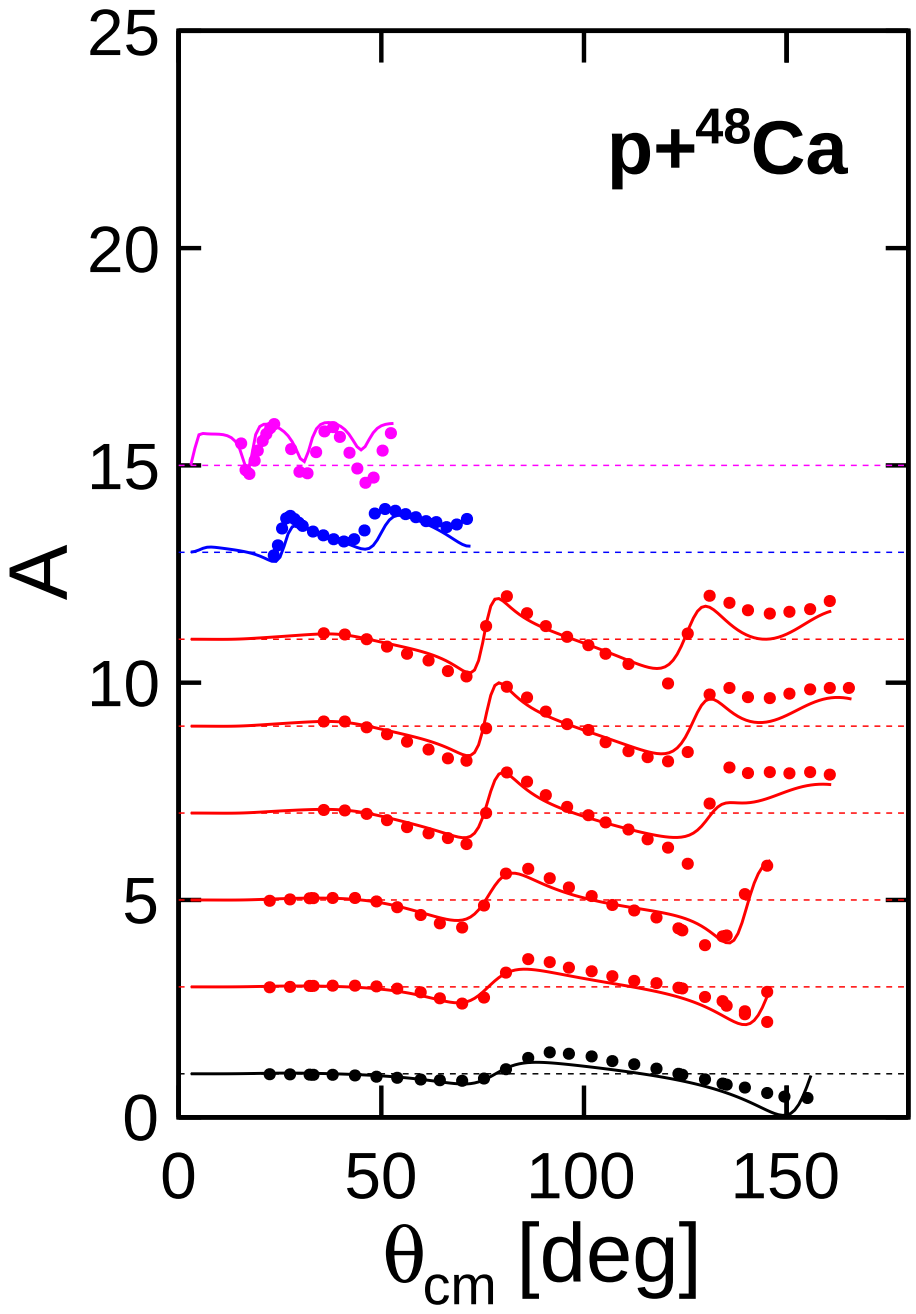

Figure 4.4: Fitted analyzing powers for proton elastic scattering on ^{48}Ca target nuclei. For clarity, successively larger energies have been shifted further up along the vertical axis. The dashed lines indicate zero analyzing power for each energy.

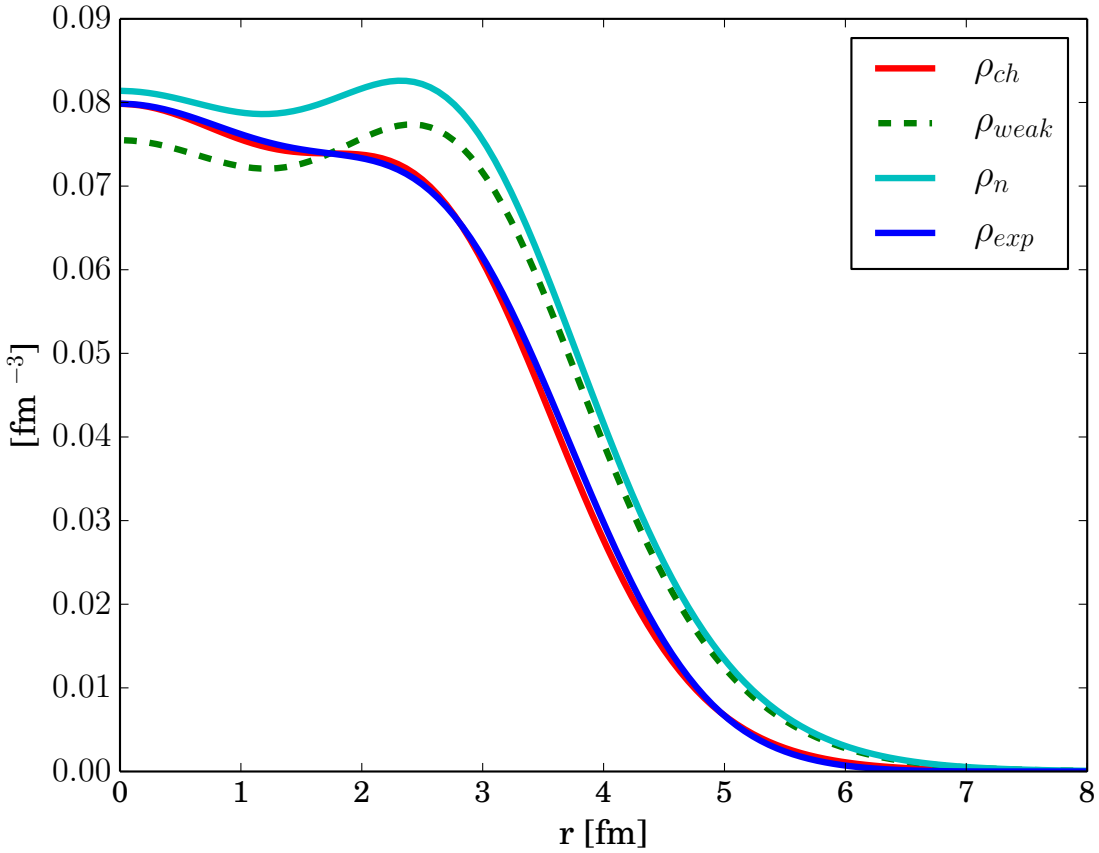

Figure 4.5: Comparison of calculated (red curve) and experimental (blue curve) folded charge density for ^{48}Ca. The calculated weak charge distribution (dashed green line) as well as neutron matter distribution (turquoise curve) are plotted too. The reduction of the weak charge distribution near the origin is the effect of proton accumulation in that region.

elastic electron scattering measurement. At low-energy in parity violating electron-nucleus scattering, the electrons interact primarily with neutrons through the exchange of the Z^0 boson of the standard model [55]. The weak form factor F_W is proportional to the fractional difference in cross section of the positive and negative helicity electron cross section [55]:

$$A_{LR} = \frac{\sigma_R - \sigma_L}{\sigma_R + \sigma_L} \tag{4.8}$$

and the form factor itself is the Fourier transform of the weak charge density which is related to the neutron density

$$F_W(q^2) = \int d^3r \; j_0(qr) \; \rho_W(r). \tag{4.9}$$

This weak form factor calculated from the parameters of the nonlocal DOM is plotted in Fig. 4.6. The projected location of the CREX data ($q^2 = 0.8$ fm^{-1}) for ^{48}Ca is also shown on Fig. 4.6. CREX (Calcium radius experiment) [56] can play an important role in revealing the methods that can be used for calculations of heavier nuclei. It also provides information about the importance of the three-body force and its importance in nuclear structure calculations. The weak charge density distribution in Fig 4.5 is calculated through

$$\rho_W(r) = 4 \int d^3r' \left[G_n^Z(|\boldsymbol{r} - \boldsymbol{r'})\rho_n(r') + G_p^Z(|\boldsymbol{r} - \boldsymbol{r'})\rho_p(r') \right] \tag{4.10}$$

where G_p^Z and G_n^Z are the electric form factors for the coupling of a Z^0 to the proton and neutron respectively:

$$G_p^Z = \frac{1}{g}(G_p - G_n) - \sin^2\theta_W G_p - \frac{1}{4}G_s \quad G_n^Z = \frac{1}{g}(G_n - G_p) - \sin^2\theta_W G_n - \frac{1}{4}G_s, \tag{4.11}$$

where G_p and G_n are the proton and neutron electromagnetic form factors. The strange quark form factor G_s assumed to be the same for protons and neutrons [55]. The weak

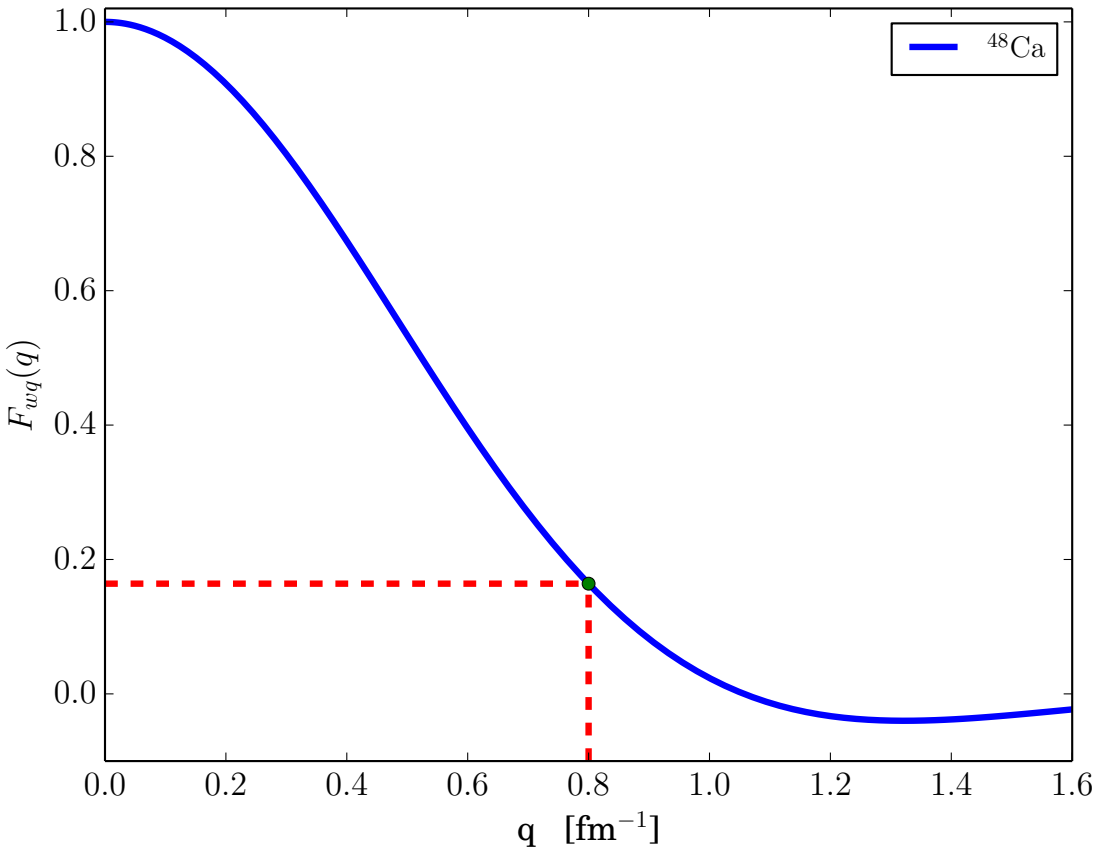

Figure 4.6: Weak form factor as a function of transfered momentum q for ^{48}Ca.

charge attributed to the weak charge density is defined by:

$$Q_W = -N + (1 - 4\sin^2\theta_W)Z, \tag{4.12}$$

for instance $\sin^2\theta_W = 0.23$ is used for ^{208}Pb in Ref. [55]. In our DOM study since all the parameters for both neutrons and protons are well constrained by data and can describe them well in ^{48}Ca, one can extract the neutron matter distribution as well as neutron skin which is the difference of neutron and proton rms radii:

$$\delta R = R_n - R_p. \tag{4.13}$$

The calculated neutron skin using the nonlocal DOM is $\delta R = 0.249 \pm 0.023$ fm. In order to calculate the error, we scramble the available elastic scattering data within the assigned experimental errors. For each energy, the elastic scattering data at different angles were scaled by a random number generated within the errors. A new fit was started using the new randomly generated data sets. This process was done about 95 times to obtain a reasonable and fairly reliable value for neutron skin error. In a recent study employing an ab initio calculation, a prediction for the neutron distribution in the neutron-rich nucleus ^{48}Ca was generated [53]. The calculated neutron skin of 0.12-0.15 fm is smaller than most mean-field calculations and our DOM result. In Fig. 4.7 the results of many mean-field calculation both relativistic and non-relativistic, for the neutron skin in ^{208}Pb and ^{48}Ca are collected following Ref. [57]. There is a significant difference between the recent coupled-cluster calculations [53] and the current nonlocal DOM result for the neutron skin in ^{48}Ca. The next task in studying the nonlocal DOM is to calculate the neutron skin for ^{208}Pb after fitting the relevant data and constructing the corresponding self-energy. The yellow line in Fig. 4.7 represents the DOM calculation. A point for ^{208}Pb will be added in the future when a corresponding fit has been generated.

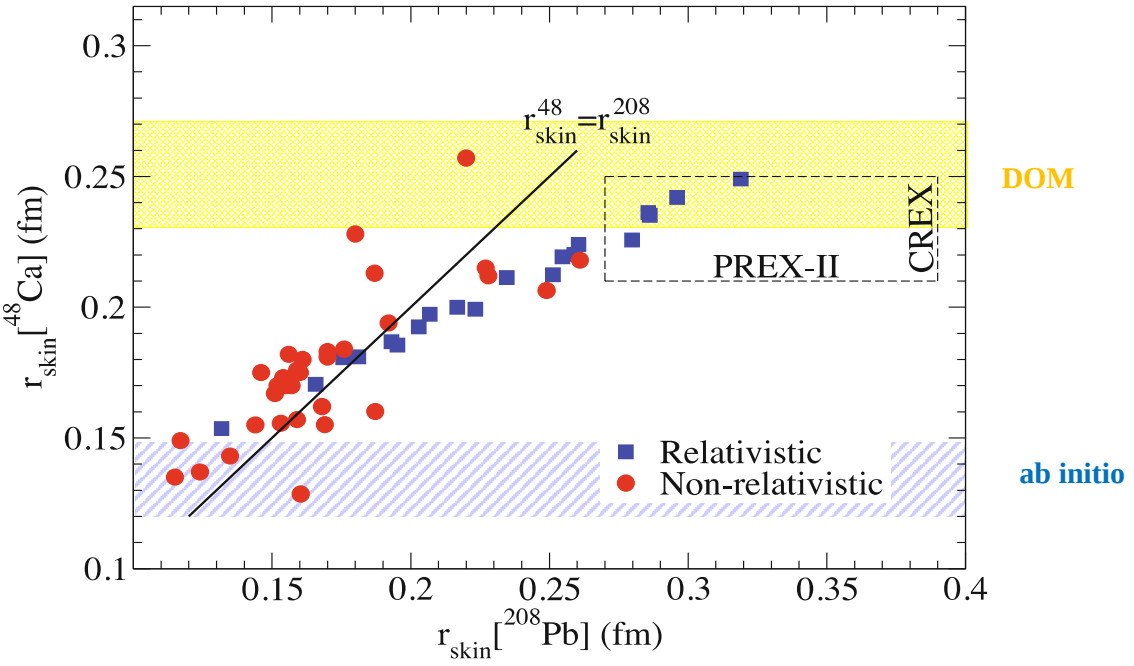

Figure 4.7: Different model calculations and predictions for ^{48}Ca and ^{208}Pb. Figure is adapted from Ref. [58] and the DOM results and the ab initio result of Ref. [53] are added. The nonlocal DOM calculation for ^{48}Ca skin is represented by the horizontal yellow bar and the calculation of Ref. [53] by the blue stripped area. The dashed box is associated with the PREX-II experiment [59] and centered at the present value for ^{208}Pb [60] but with the expected error of PREX-II. The CREX error [56] represents the vertical width of the box and its central value is arbitrarily chosen.

4.6 Comparing ^{40}Ca and ^{48}Ca properties

4.6.1 Potentials

Studying potentials obtained from the fits to both ^{40}Ca and ^{48}Ca can reveal many properties of interest, for instance the asymmetry dependence of the imaginary potential influences the asymmetry dependence of occupation numbers and spectroscopic factors. The evolution of the potential in different nuclei determines how correlations are changing by adding or removing protons or neutrons. In this work the asymmetry dependence is incorporated by employing the $N - Z$ factor, starting from ^{40}Ca. Traditionally the asymmetry term has a positive sign for neutrons and a negative one for protons with the same absolute value, however we allow these quantities to be different for protons and neutrons at both negative and positive energies. In Fig. 4.8 the energy dependence of the proton volume terms of the imaginary potential for ^{48}Ca and ^{40}Ca are compared. The presence of the additional eight neutrons leads to more volume absorption for protons in ^{48}Ca. A similar comparison of surface part of the proton potential is plotted in Fig. 4.9. Comparing Figs. 4.1 and 3.2 for protons, we note the data demand more absorption for positive energy ^{48}Ca than ^{40}Ca in the surface domain which corresponds to the results shown in Fig. 4.9. Part of this increase in asymmetry appears to be related to the tensor force which has a more significant effect for the protons in ^{48}Ca [25]. The surface absorption in ^{48}Ca exhibits a little difference below and above the Fermi energy as in the local DOM work [26, 20]. Comparison with the result for ^{40}Ca shows that the surface absorption at lower energy is larger for ^{48}Ca. We note that whereas for ^{40}Ca the self-energy at negative energies is well constrained by experimental data this is not the case for ^{48}Ca. This shows a certain ambiguity in determining the shape of the potential below Fermi energy. This can be resolved by further experiments at Jefferson lab (Jlab) at high momenta for proton removal from ^{48}Ca. There are also no experimental data

for the deeply bound $s_{1/2}$ width in ^{48}Ca whereas it is measured for ^{40}Ca. This is another source of ambiguity in constraining the self-energy at negative energies for ^{48}Ca. This can also be removed by future experiments. Further clarification is provided by comparing the volume integral of the imaginary potentials for ^{48}Ca and ^{40}Ca. These potentials are given in Eqs. (4.8) and (3.5) which contain angular dependence. We therefore plot volume integrals according to Eq. (3.22) which employs projected volume integrals. The results plotted for protons for $\ell = 0$ to $\ell = 5$ are shown in Fig. 4.10. These plots include both surface and volume contributions to the self-energy. In Fig. 4.10 the red curve represents the volume integral of the ^{48}Ca self-energy and exhibits more absorption in the domain of surface absorption both at positive and negative energies. In the fit to obtain the parameters for the ^{40}Ca self-energy, the potential was constrained by the $(e, e'p)$ data at high missing momenta. For ^{48}Ca such data are not available and therefore the self-energy is not constrained at large missing energies. As a consequence, the energy distribution of high-momentum protons is not constrained and therefore it is not appropriate to evaluate the energy sum rule for this nucleus as it is dominated by such terms as discussed in Ch. 3 for ^{40}Ca. Although Figs 4.9 and 4.8 suggest more absorption for ^{48}Ca than ^{40}Ca, at these energies, Fig. 4.10 demonstrates that is not the case in terms of the total volume integral of the potential. The constraint of particle number and the charge density therefore forces the radius parameter to be smaller in case of ^{48}Ca compared to ^{40}Ca. At positive energies a similar effect is demonstrated in Fig. 4.10 because the elastic scattering data for protons constrain the volume integral above the Fermi energy. In the domain of volume absorption of ^{48}Ca and ^{40}Ca, $E > 50$ MeV, volume integrals are the same reflecting a fit to the scattering data in both nuclei. This suggests that protons in both nuclei interact in the interior of the nucleus with a similar composition of protons and neutrons. This is confirmed by comparing the interior densities in Figs. 4.5 and 3.12. These figures shows that the main difference is in the domain of surface absorption which argues for the larger skin for ^{48}Ca as shown in Fig. 4.7. Such a conclusion

can only be derived in the nonlocal DOM since proper results for densities can be obtained.

In Figs. 4.11 and 4.12 the neutron imaginary volume and surface potentials for ^{48}Ca are plotted respectively. There is less asymmetry dependence for neutrons than protons in ^{48}Ca. Consequently proton spectroscopic factors and occupation numbers are more affected than for neutrons, moving from ^{40}Ca to ^{48}Ca due to increased correlation for protons with the extra 8 neutrons. For completeness the corresponding results for neutrons are plotted in Figs. 4.11-4.13 noting that neutron data provide considerably less restrictions on these results compared to protons.

4.6.2 Spectral functions and spectroscopic factors

A comparison of the valence spectroscopic factors for ^{48}Ca and ^{40}Ca are given in Tables 4.1 and 4.2. As one can see in Table 4.1 the spectroscopic factors for the orbits near the Fermi energy are smaller for protons in ^{48}Ca. The above discussion of the volume integrals of the imaginary potentials is consistent with these results. Neutron spectroscopic factors do not follow the same trend, as we see in Table 4.2 the neutron spectroscopic factors remain almost the same in these two isotopes. It confirms the higher correlation between proton-neutron than neutron-neutron which can partially be explained by the tensor force [61, 25]. It is

Table 4.1: Comparison of proton spectroscopic factors in ^{40}Ca and ^{48}Ca.

orbit	^{48}Ca	^{40}Ca
$0d_{5/2}$	0.64	0.80
$0d_{3/2}$	0.65	0.79
$0f_{7/2}$	0.58	0.73
$1s_{1/2}$	0.71	0.82

also in agreement with the results in [20] which implies that protons with energies near the Fermi surface experience larger correlations with increasing asymmetry for $N > Z$. The

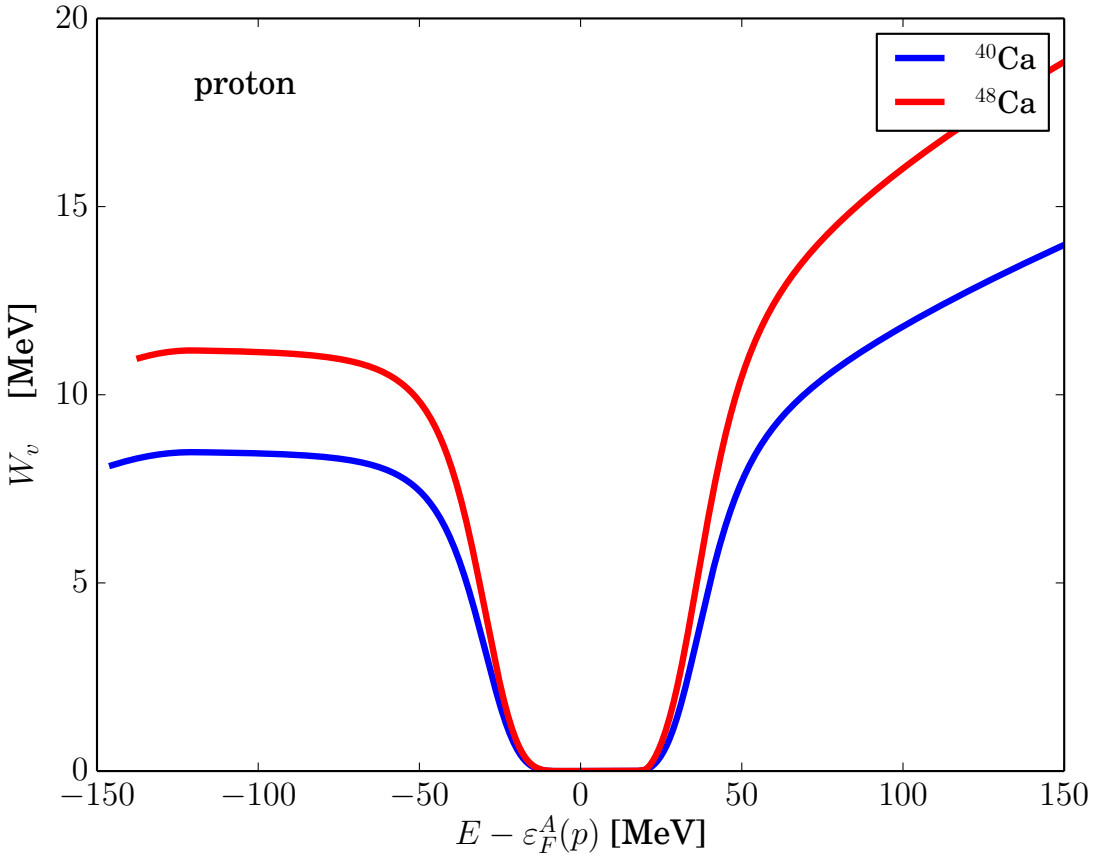

Figure 4.8: The energy dependence of the imaginary part of the proton volume potential $W^{vol,p}(E)$.

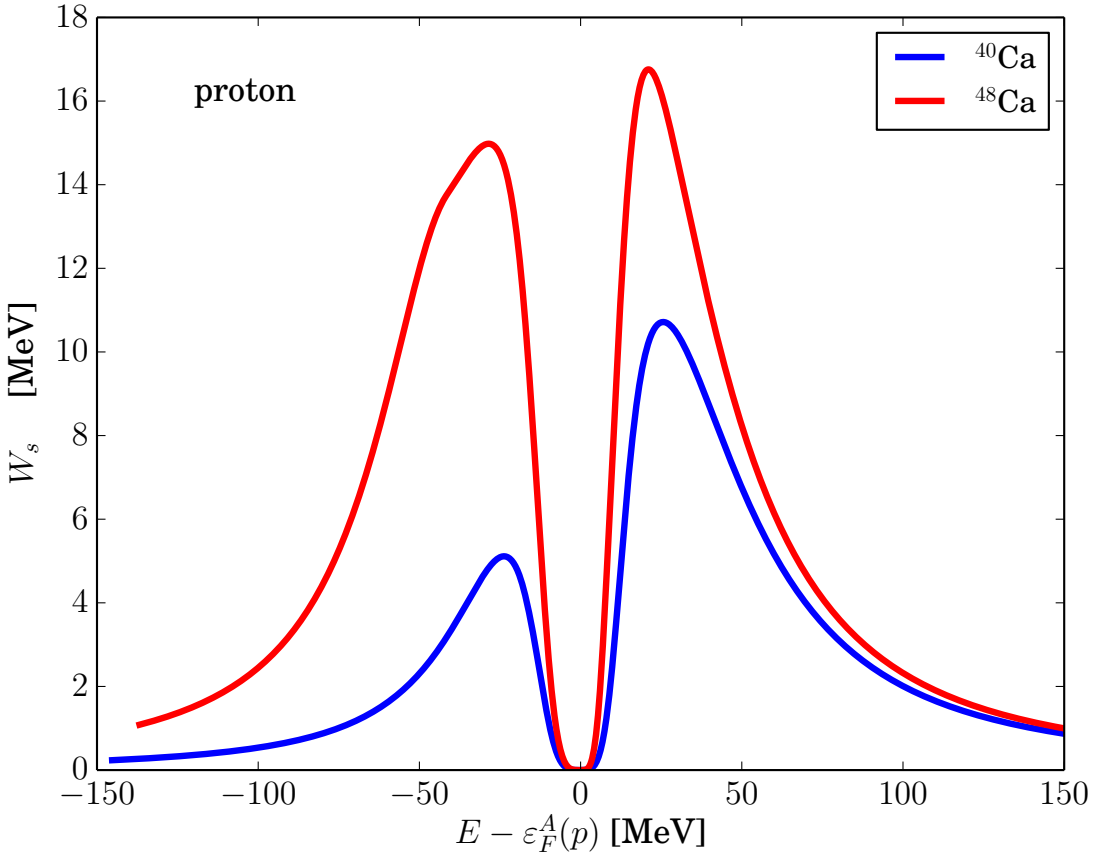

Figure 4.9: The energy dependence of the imaginary part of the proton surface potential $W^{sur,p}(E)$.

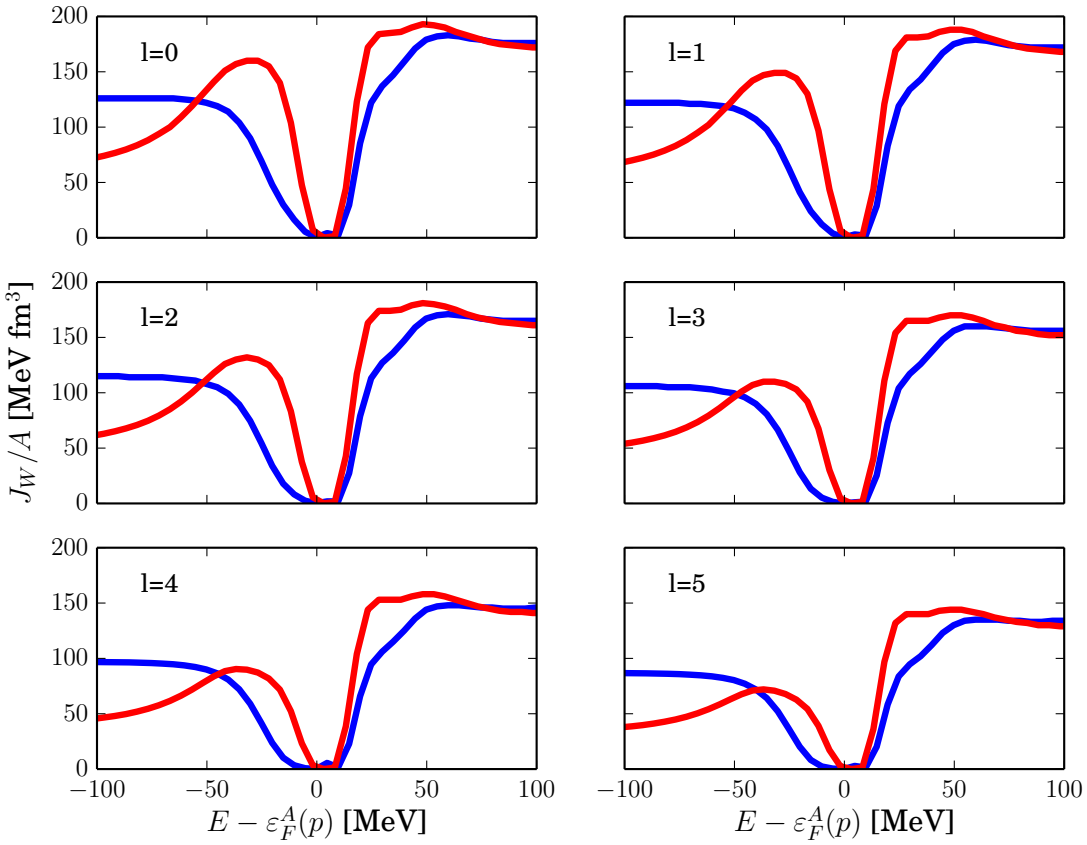

Figure 4.10: Comparison of the volume integral of the imaginary part of the potential for protons in ^{48}Ca (red) and ^{40}Ca (blue).

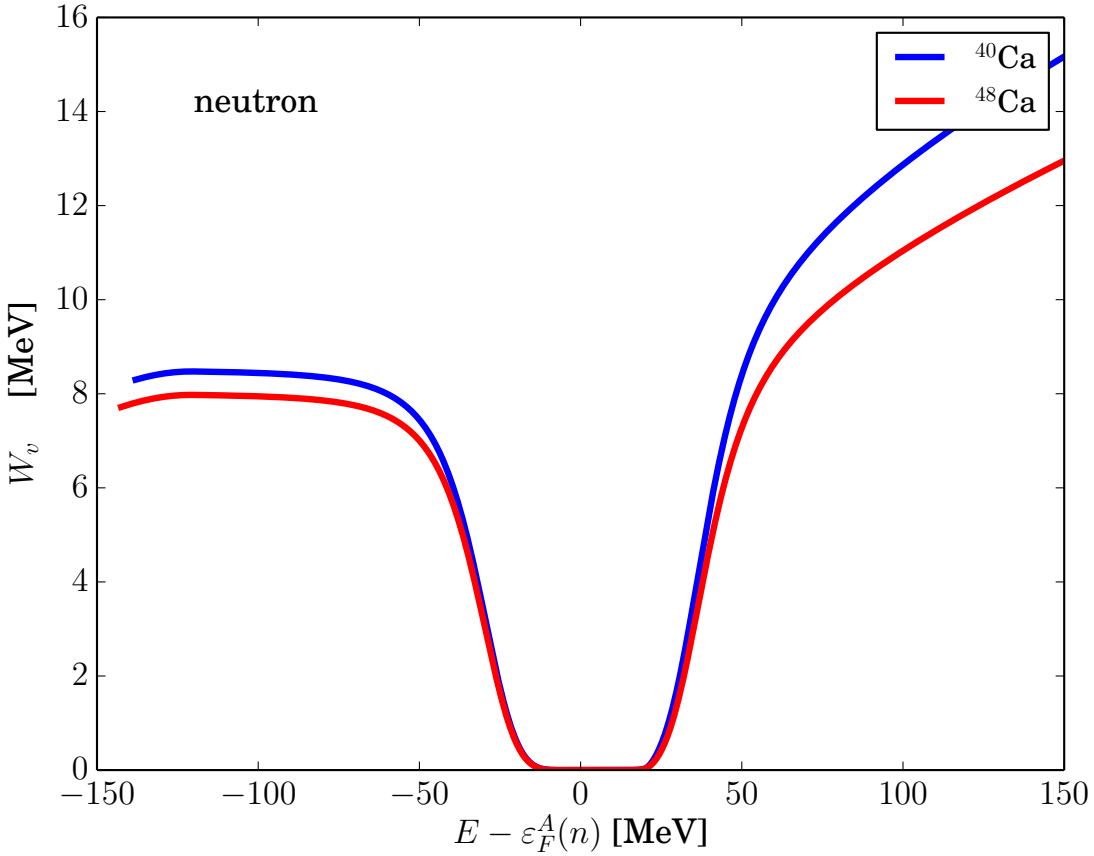

Figure 4.11: The energy dependent part of the neutron volume potential $W^{vol,n}(E)$.

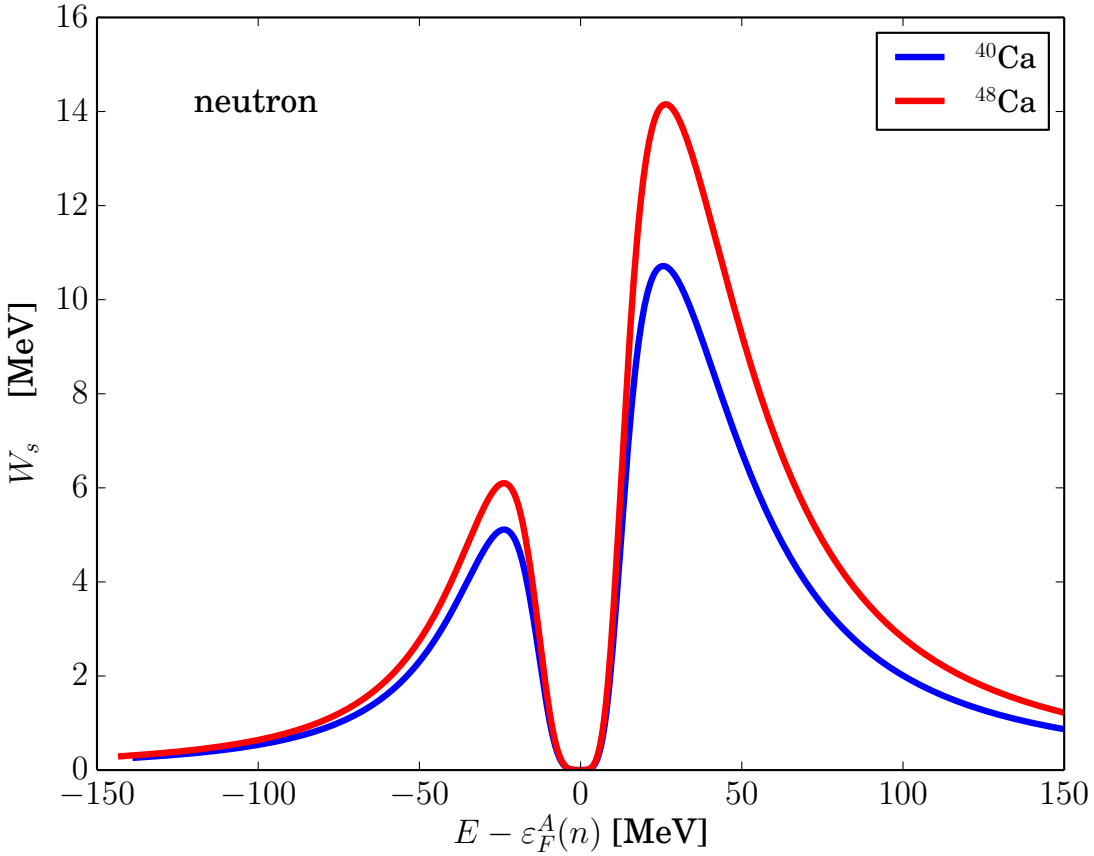

Figure 4.12: The energy dependence part of the neutron surface potential $W^{sur,n}(E)$.

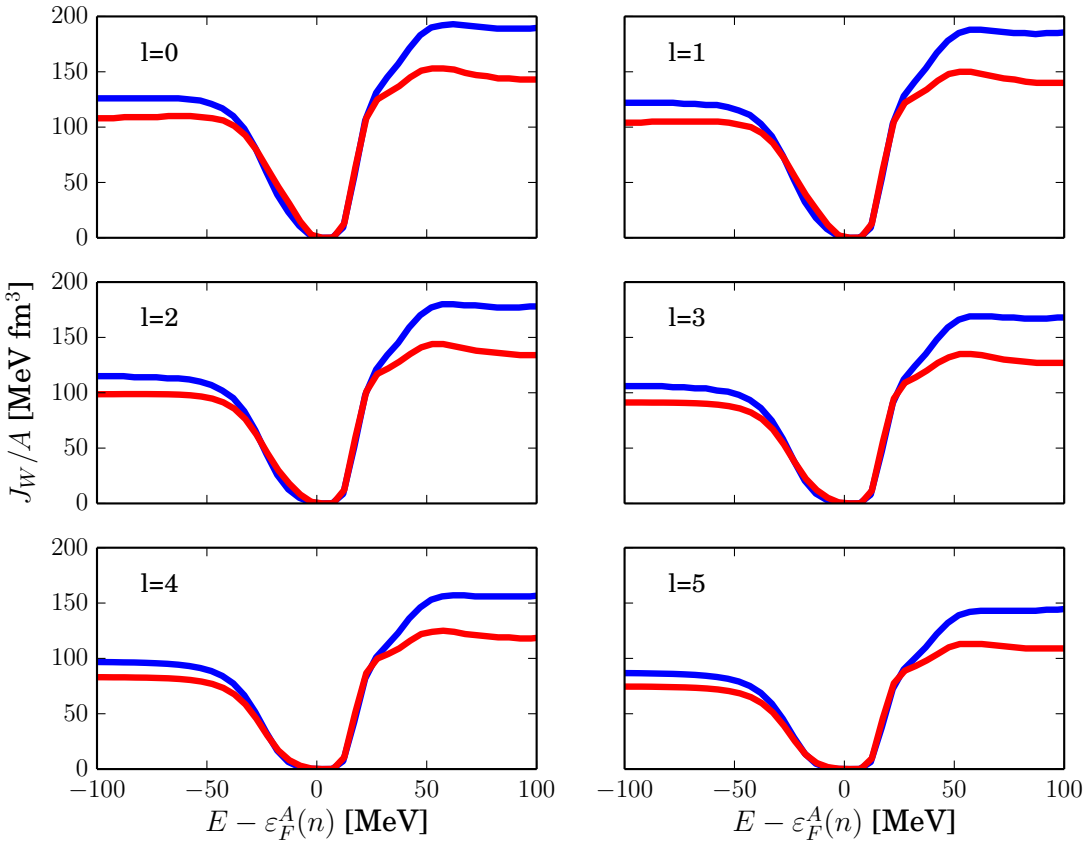

Figure 4.13: Comparison of the volume integral of the imaginary part of the potential for neutrons in ^{48}Ca (red) and ^{40}Ca (blue).

Table 4.2: Comparison of neutron spectroscopic factors in ^{40}Ca and ^{48}Ca.

orbit	^{48}Ca	^{40}Ca
$1p_{3/2}$	0.78	0.78
$1p_{1/2}$	0.77	0.80
$0f_{7/2}$	0.80	0.72
$0d_{3/2}$	0.77	0.79
$1s_{1/2}$	0.80	0.82

proton spectral function of the bound orbits are plotted in Fig. 4.14 and for neutrons in Fig. 4.15 . The numerical calculations to obtain the spectral functions are totally different for negative and positive energies. The small discontinuity, which is more significant for $f_{7/2}$, seen in Fig. 4.14 is partially explained by the difficulty to include the Coulomb potential at low energy. The plotted spectral functions in Fig. 4.14 can be compared to Fig. 3.4. The difference in the width of the $0s$ orbit reflects the effect of the volume integral which is not constrained by data in case of ^{48}Ca. There is an increase in absorption in ^{48}Ca that can be seen in more detail in Fig. 4.16.

The spectral functions in Fig. 4.16 for protons and Fig. 4.17 for neutrons are shifted so that the Fermi energy is at zero. It makes it easier to compare the proton spectral functions. As one can see in Fig. 4.16 the ^{48}Ca proton spectral functions exhibit more strength at all energies except at the quasi-hole peaks. This fact accounts for the lower spectroscopic factor and describe the correlations in the latter Ca isotope. Comparing the spectral functions in Figs. 4.14 and 4.15 we can see there is more depletion to the continuum for protons in ^{48}Ca. This effect is more significant for the $f_{7/2}$ orbit which is an occupied state for neutrons in ^{48}Ca. In Fig. 4.18 the occupation numbers are plotted for protons and neutrons as a function of the position of the quasi-hole or quasi-particle peaks. The most obvious observation is the reduction of the proton occupation number from ^{40}Ca (triangles) to ^{48}Ca (squares). The reduction is larger for orbits close to the Fermi energy reflecting the increased absorption. It is no surprise that the proton and neutron occupation numbers are almost the same in

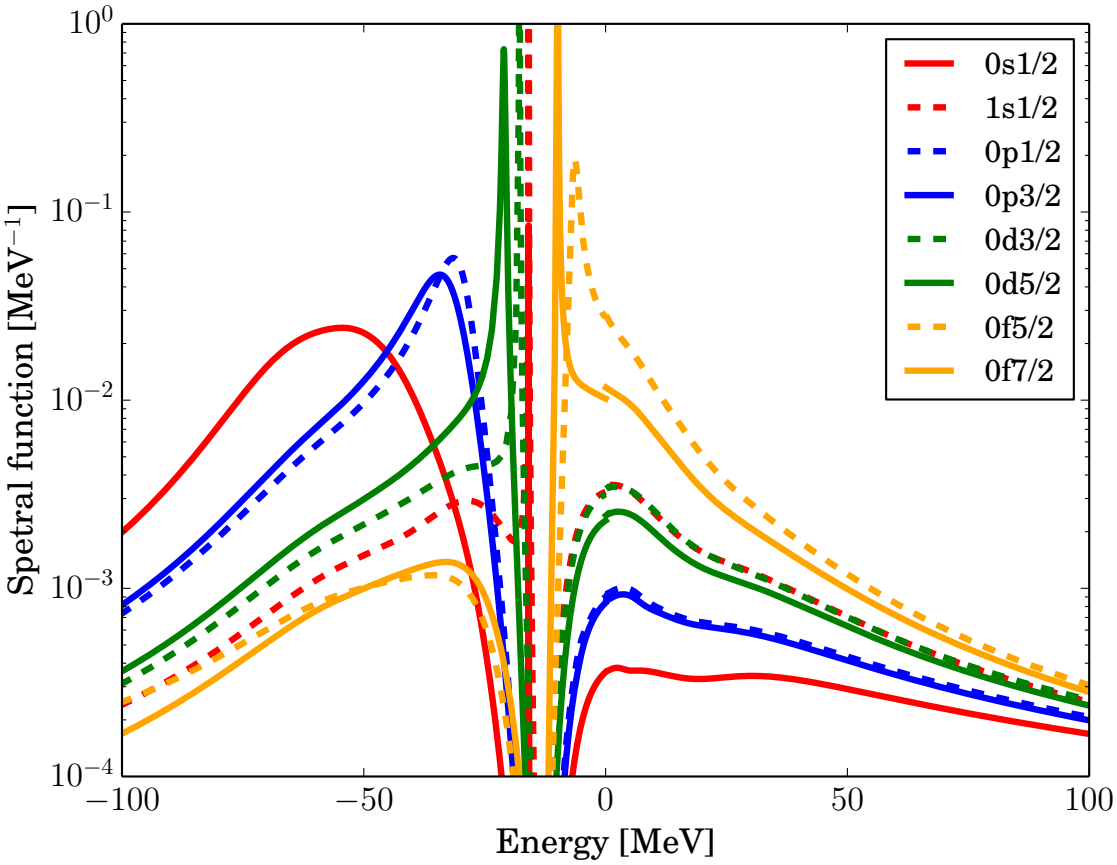

Figure 4.14: Proton spectral functions for ^{48}Ca.

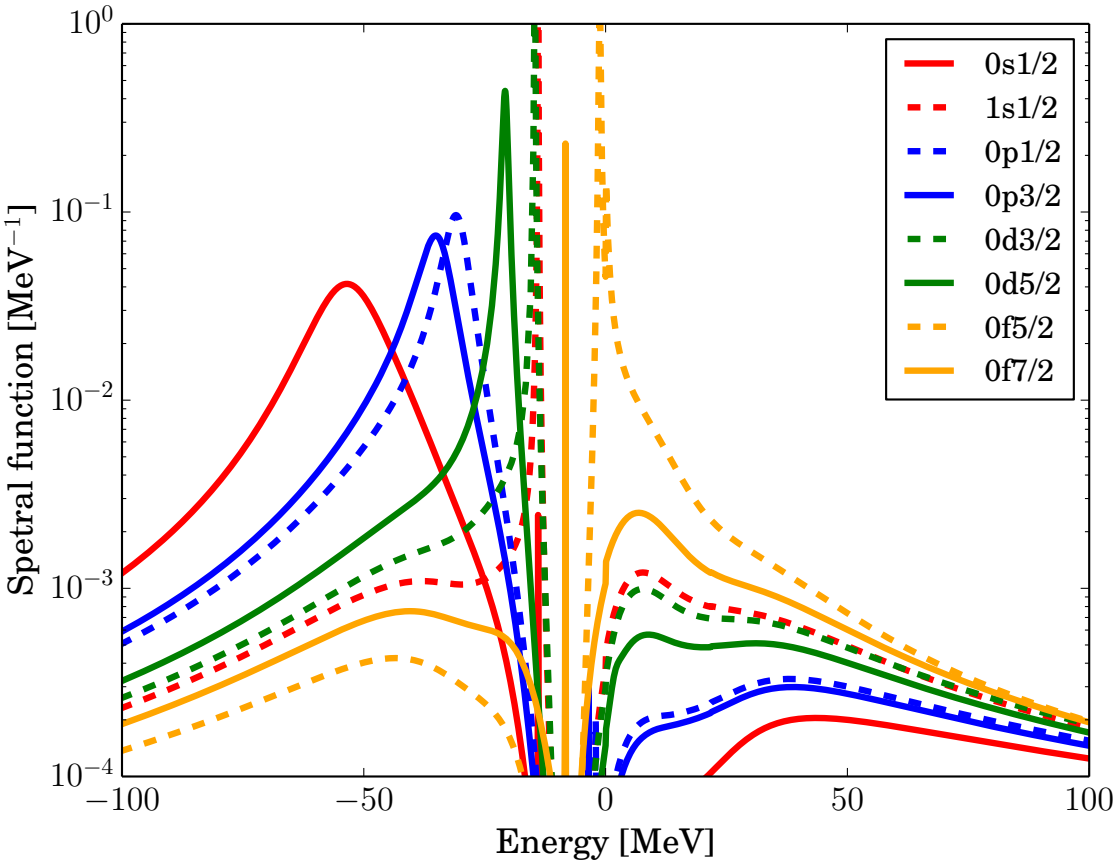

Figure 4.15: Neutron spectral functions for ^{48}Ca.

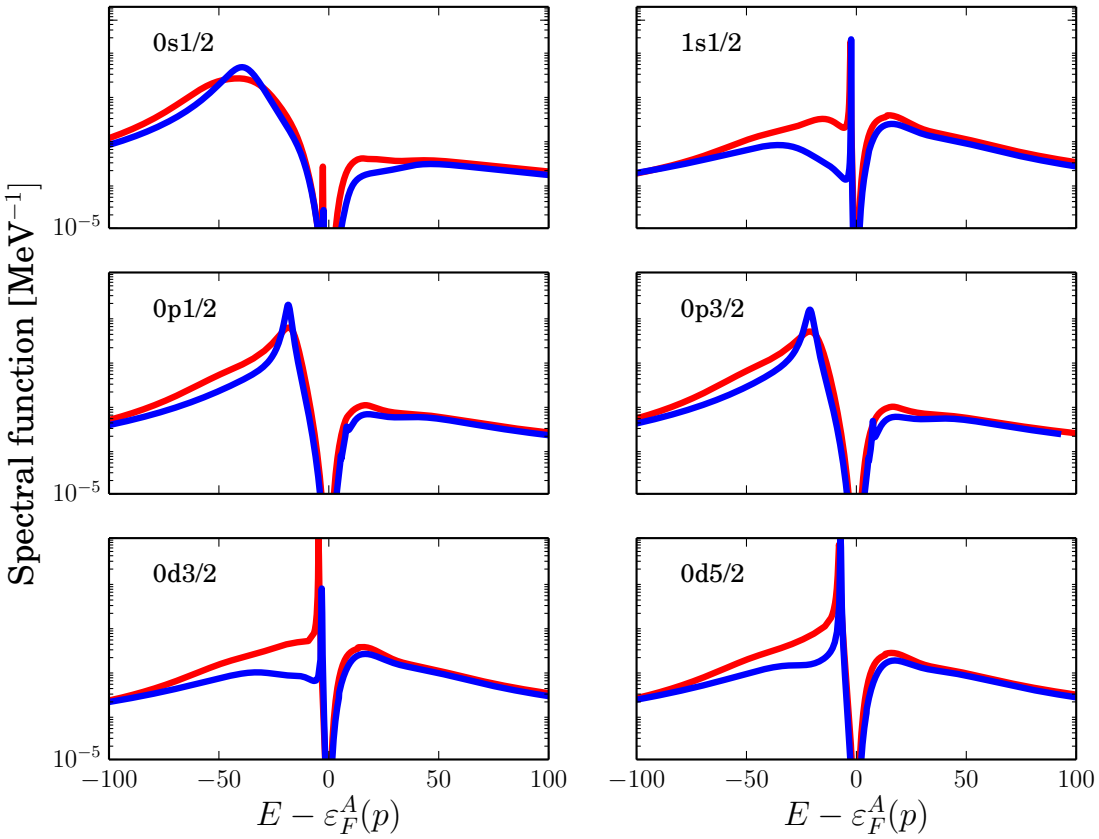

Figure 4.16: Comparison of proton spectral function for ^{48}Ca (red) and ^{40}Ca (blue) for the first and second s orbits and the p and d spin-orbit partners.

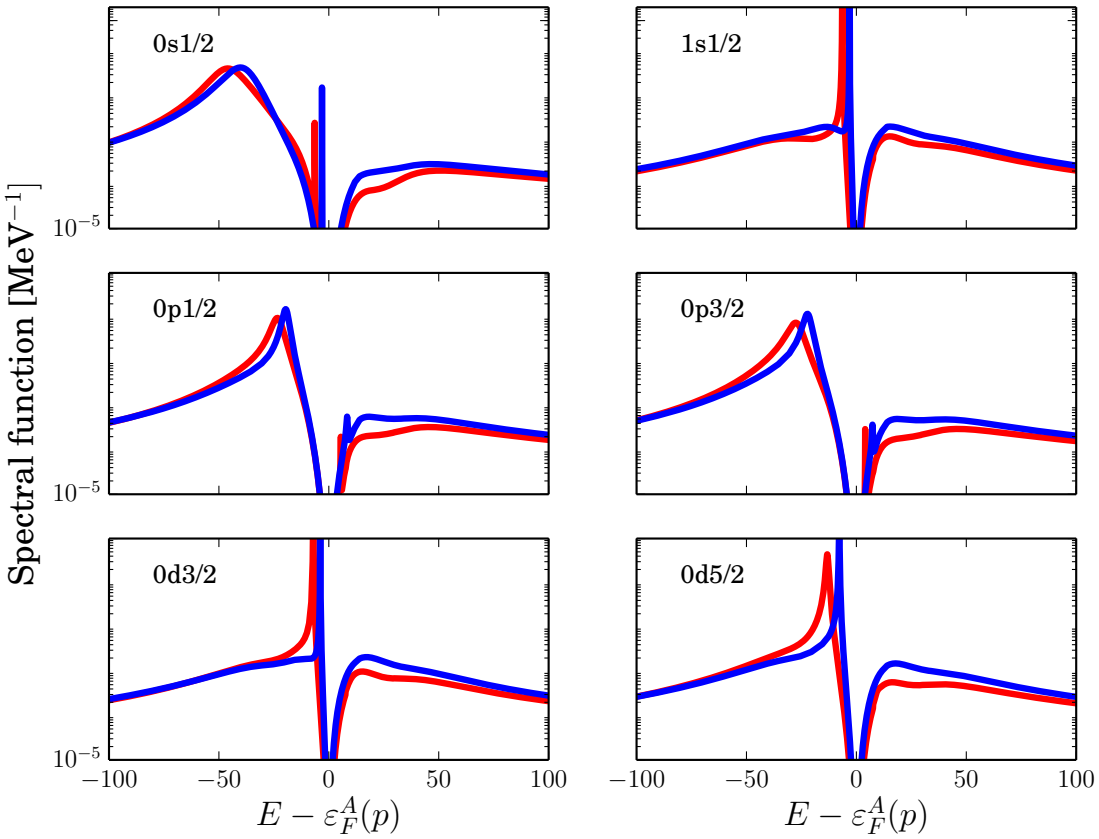

Figure 4.17: Comparison of neutron spectral functions for ^{48}Ca (red) and ^{40}Ca (blue) for the same orbits as in Fig 4.16.

^{40}Ca, since the only difference is the Coulomb energy shift (the shift in the triangles in Fig. 4.18). The occupation number slightly increases for neutrons in ^{48}Ca compared to ^{40}Ca. The $f_{7/2}$ neutron orbit is occupied in ^{48}Ca is represented by the green square on the top right in Fig. 4.18.

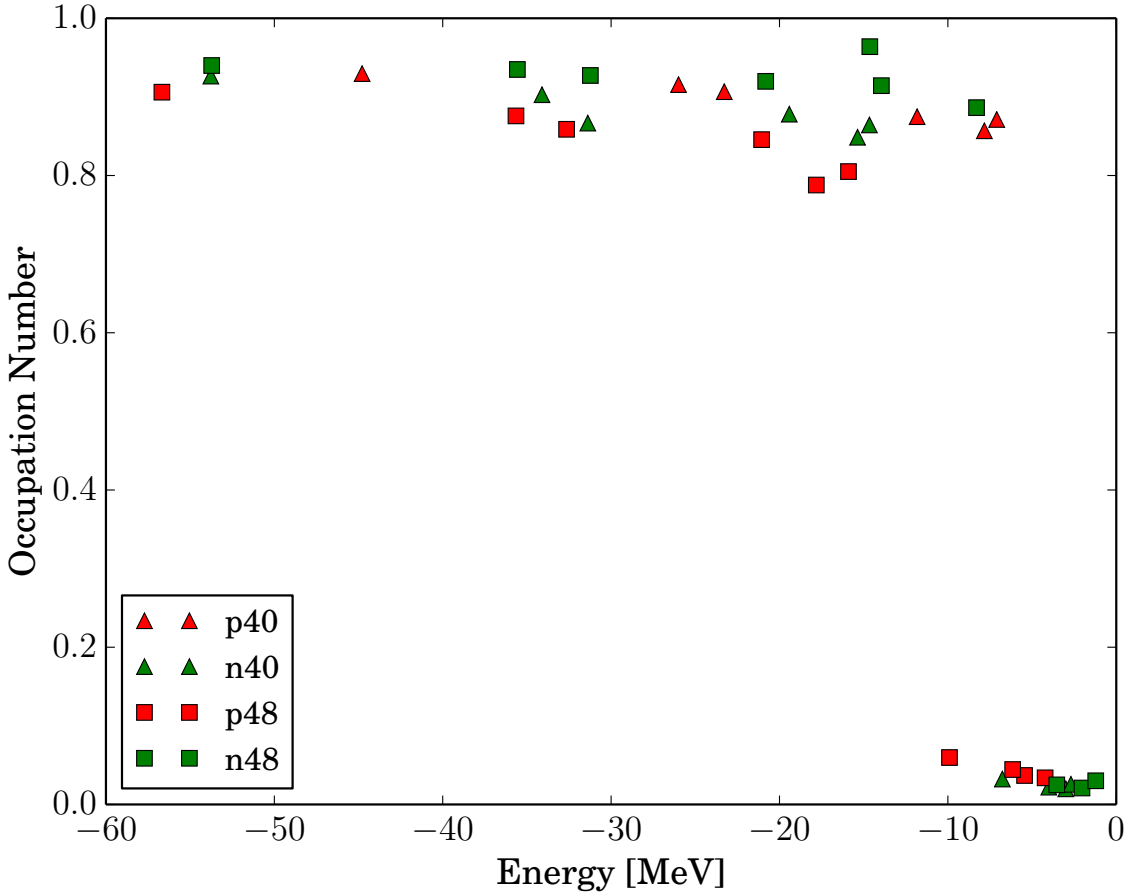

Figure 4.18: Occupation numbers for the double closed-shell nuclei ^{48}Ca and ^{40}Ca.

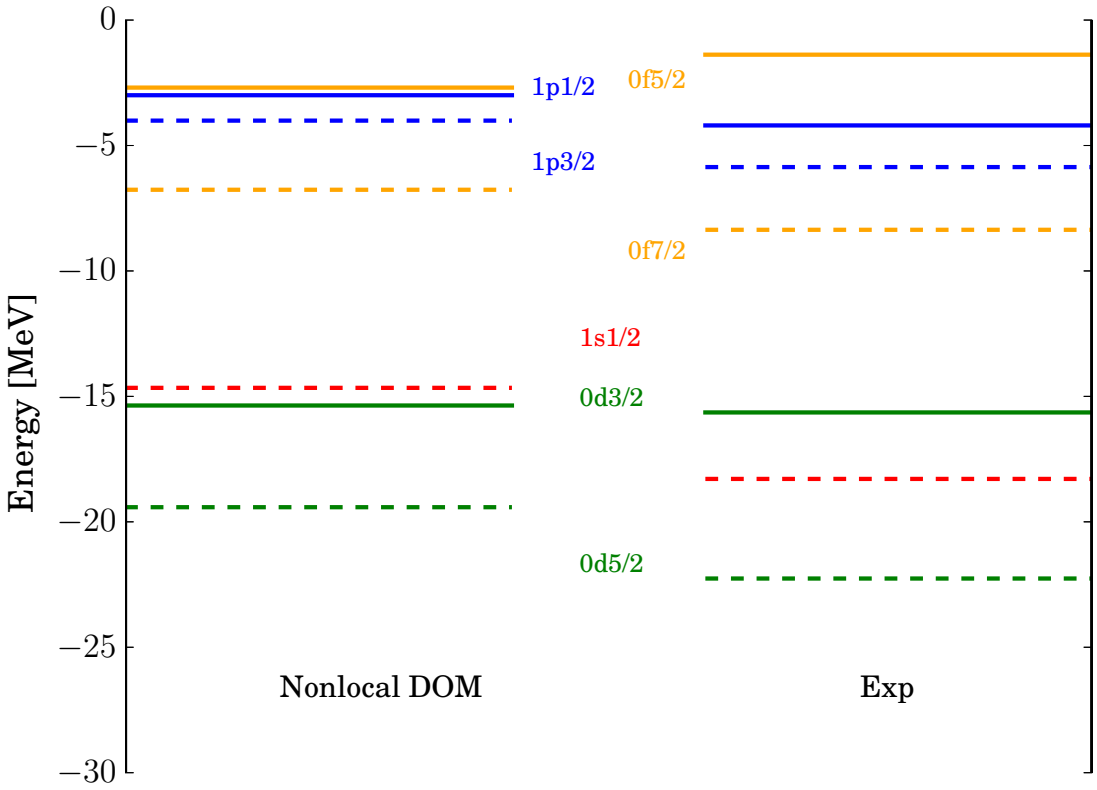

Figure 4.19: Comparison of experimental and fitted neutron single-particle levels for ^{40}Ca. Experimental data are taken from mass tables and relevant excitation energies in individual nuclei.

Table 4.3: Neutron energy levels near the Fermi energy in ^{40}Ca compared to experiment.

orbit	DOM [MeV]	Exp [MeV]
$0f_{7/2}$	-7.36	-8.36
$0d_{3/2}$	-16.2	-15.6
$1s_{1/2}$	-15.3	-18.3

4.6.3 Level structure

The positions of quasi-particle peaks near the Fermi energies for neutrons and protons for both ^{40}Ca and ^{48}Ca are plotted in the Figs. 4.19-4.22. These fitted energy levels do not exactly reproduce the experimental data but are reasonably consistent. It is useful to keep in mind that these energy levels are just a couple of data points in the fit. We note for example that the spin-orbit splitting calculated in the DOM tends to be smaller than the experimental one for all cases. Comparing the number of data points associated with elastic scattering with result near the Fermi energy in determining the chi-squared below and above the Fermi energy one might conclude that it is not straightforward to get very good results for all the energy level values at their experimental values. As expected the single-particle energies look more squeezed close to Fermi energy for the DOM compared to the HF (role of dispersive correction). As a future extension the tensor force can be directly incorporated in the HF term. This can show how the protons and neutrons are influenced by the explicit effect of the tensor force [61]. Figures 4.19 and 4.20 are the same except a shift in the levels due to the Coulomb potential whereas for ^{48}Ca eight more neutrons provide for a mostly filled $f_{7/2}$ state.

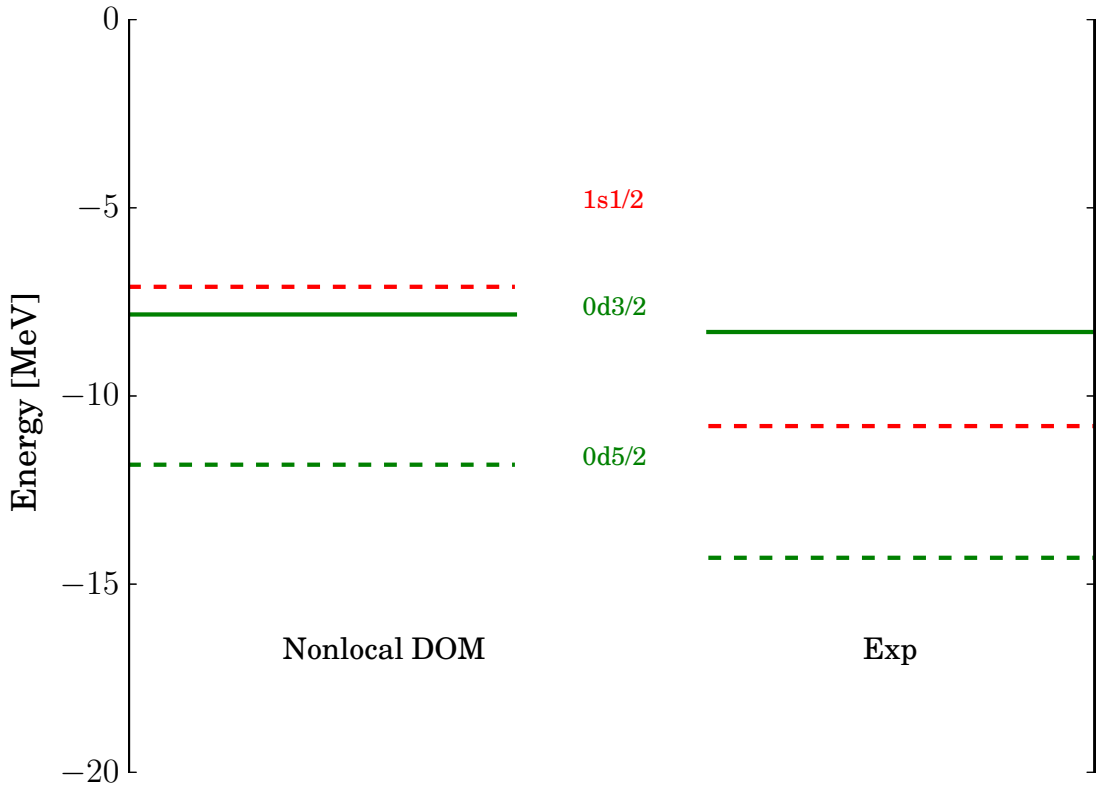

Figure 4.20: Comparison of experimental and fitted for proton single-particle levels for ^{40}Ca.

Table 4.4: Proton energy levels near the Fermi energy in ^{40}Ca compared to experiment.

orbit	DOM [MeV]	Exp [MeV]
$0d_{5/2}$	-11.8	-14.3
$0d_{3/2}$	-7.8	-8.3
$1s_{1/2}$	-7.1	-10.8

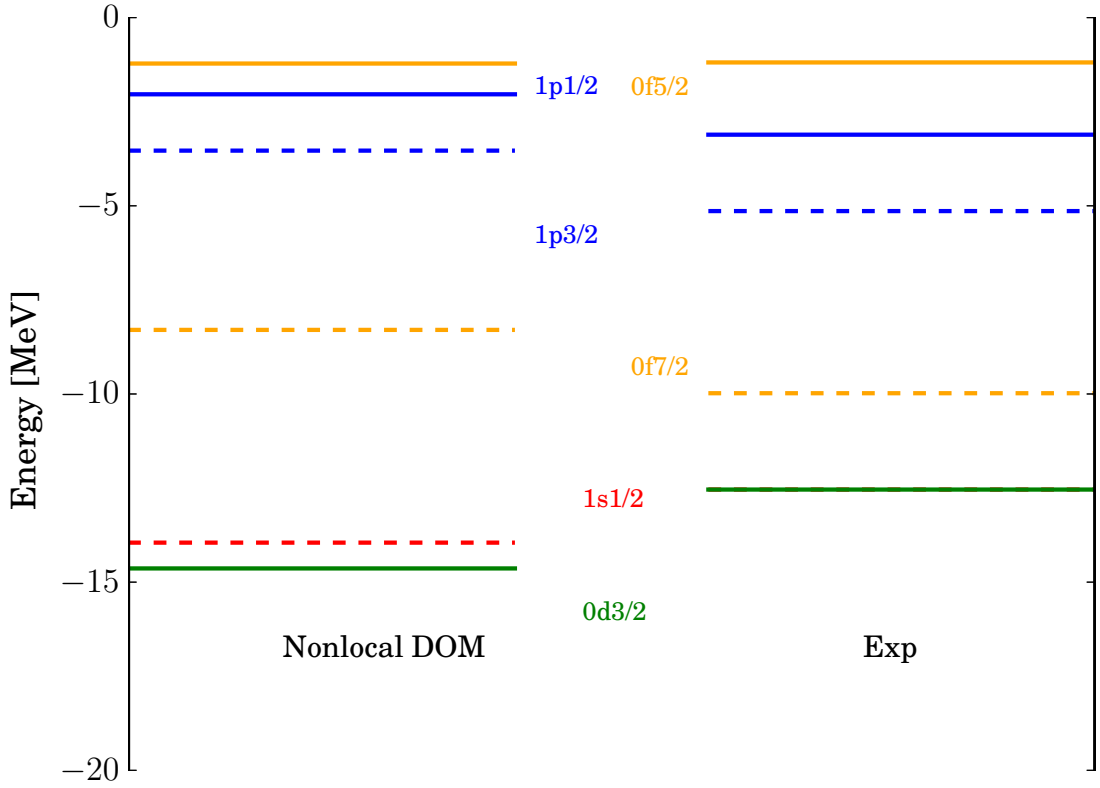

Figure 4.21: Comparison of experimental and fitted for neutron single-particle levels for ^{48}Ca.

Table 4.5: Neutron energy levels near the Fermi energy in ^{48}Ca compared to experiment.

orbit	DOM [MeV]	Exp [MeV]
$1p_{3/2}$	-3.5	-5.14
$1p_{1/2}$	-2.0	-3.11
$0f_{7/2}$	-8.3	-9.9
$0d_{3/2}$	-14.6	-12.5
$1s_{1/2}$	-13.9	-12.5

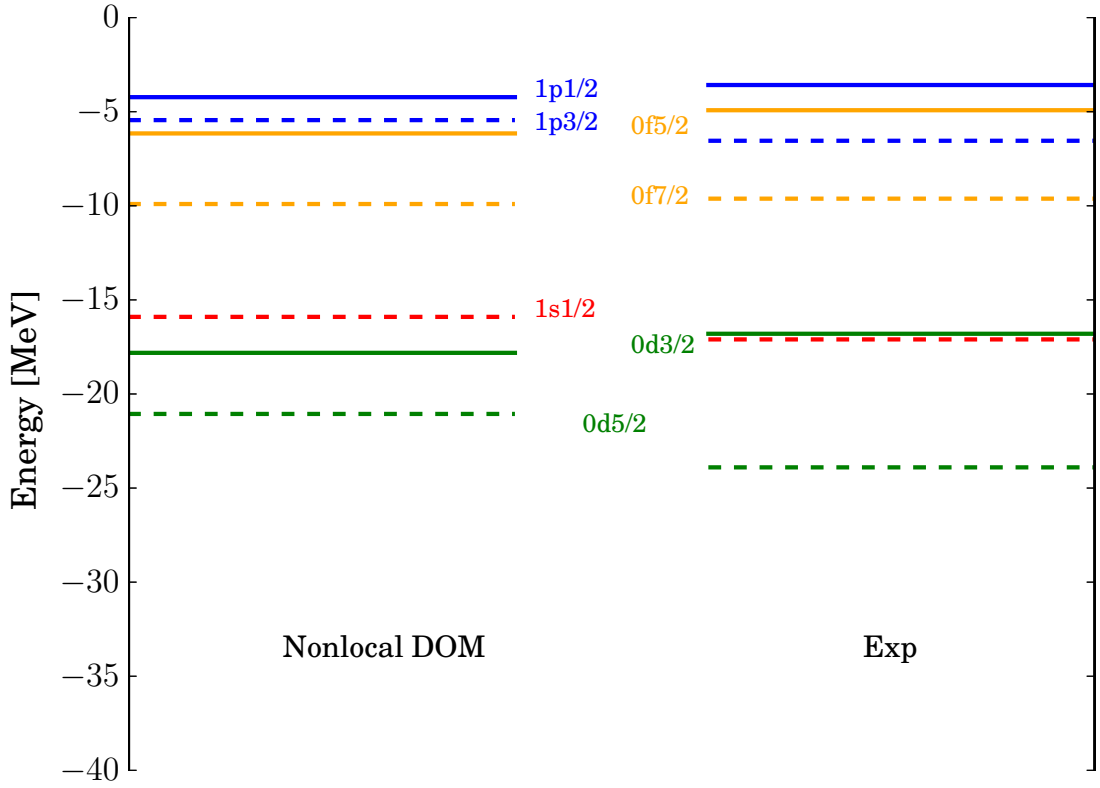

Figure 4.22: Comparison of experimental and fitted for proton single-particle levels for ^{48}Ca.

Table 4.6: Proton energy levels near the Fermi energy in ^{48}Ca compared to experiment.

orbit	DOM [MeV]	Exp [MeV]
$1p_{3/2}$	-5.4	-6.5
$1p_{1/2}$	-4.2	-3.6
$0f_{7/2}$	-9.9	-9.6
$0d_{3/2}$	-17.8	-16.8
$1s_{1/2}$	-15.9	-17.1

5 Conclusions

The main purpose of this work was to implement a fully nonlocal DOM as an extension of the research reported in [62]. In previous local DOM calculations, many properties of nuclei were studied with emphasis on scattering data at positive energies. The energy dependence contained in the HF self-energy leads to serious difficulties in describing the solution of the Dyson equation at negative energies and requires the introduction of an energy-independent nonlocal term. Nonlocality is also necessary to describe the imaginary part of the self-energy in order to accurately represent particle number and the nuclear charge density. In Ch. 3 a completely nonlocal implementation of the DOM is presented for ^{40}Ca. Contrary to local versions of the DOM, the nonlocal DOM can represent particle number and the charge density accurately for the first time. In addition, high-momentum protons constrained by experimental data from Jefferson Lab can be adequately represented leading to a binding energy of ^{40}Ca ground-state of 7.91 MeV per particle. The latter value leaves only 0.64 MeV per particle binding for higher-body interactions which is of similar size as found in Green's function Monte-Carlo calculations for light nuclei. Furthermore it is shown that the fit to elastic scattering data determines the amount of SP strength in this energy domain associated with bound orbits providing a quantitative measure of the depletion of the Fermi sea. By comparing the spectral functions at positive and negative energies for these bound

orbits we have investigated the relevant sum rule describing depletion and occupation. The nonlocal DOM self-energy is able to describe the available experimental data at positive energies for both protons and neutrons with the same quality as the local version. Overall, the nonlocal DOM implementation was able to describe all available bound-state data for ^{40}Ca accurately. Starting from the constrained self-energy for ^{40}Ca a nonlocal DOM implementation is presented for ^{48}Ca in Ch. 4. It includes an additional $N - Z$ term in the self-energy. The same procedure used in Ch. 3 was applied and the relevant experimental data at positive as well as negative energies. At positive energies a substantial improvement is obtained compared to the local DOM for the description of neutron elastic scattering data in this nucleus. An important quantity with astrophysical implications is the neutron distribution which leads to a neutron skin $\delta R = R_n - R_p$. The value we predict for the neutron skin is $\delta R = 0.249 \pm 0.023$ fm. This value is larger than most mean-field calculations of this quantity and substantially larger than the value of an ab initio calculation. A future experiment at Jefferson Lab employing parity violating elastic electron scattering may clarify this situation. More experimental data for proton knock-out from ^{48}Ca especially at negative energies may provide additional constraints related to high-momentum protons in this nucleus. Applying the nonlocal DOM formalism for heavier elements like ^{208}Pb should be a high priority for future work. The nonlocal DOM generates different distorted waves than the local version and a reanalysis of the $(e, e'p)$ reaction is required to clarify the consistency of spectroscopic factors extracted from such experiments and the present study.

Bibliography

[1] J. S. Bell and E. J. Squires. *Phys. Rev. Lett.*, 3:96, 1959.

[2] C. Mahaux and R. Sartor. *Adv. Nucl. Phys.*, 20:1, 1991.

[3] W. H. Dickhoff, D. Van Neck, S. J. Waldecker, R. J. Charity, and L. G. Sobotka. *Phys. Rev. C*, 82:054306, 2010.

[4] M. H. Mahzoon, R. J. Charity, W. H. Dickhoff, H. Dussan, and S. J. Waldecker. *Phys. Rev. Lett.*, 112:162503, 2014.

[5] H. Dussan, M. H. Mahzoon, R. J. Charity, W. H. Dickhoff, and A. Polls. *Phys. Rev. C*, 90:061603, 2014.

[6] J. Piekarewicz. *Revista Mexicana de Fisica S*, 54, 2008.

[7] C. J. Horowitz and J. Piekarewicz. *Phys. Rev. C*, 64:062802, 2001.

[8] C. J. Horowitz and J. Piekarewicz. *Phys. Rev. Lett.*, 86:5647, 2001.

[9] A. Ross, L. J. Titus, F. M. Nunes, M. H. Mahzoon, W. H. Dickhoff, and R. J. Charity. *Phys. Rev. C*, 92:044607, 2015.

[10] W. H. Dickhoff and D. Van Neck. *Many-Body Theory Exposed!* World Scientific, New Jersey, 2008.

[11] H. Lehmann. *Nuovo Cim.*, 11:342, 1954.

[12] A. L. Fetter and J. D. Walecka. *Quantum Theory of Many-Particle Systems.* Dover, 2003.

[13] E. Titchmarsh. *Introduction to the theory of Fourier integrals.* Clarendon Press, Oxford University, 1986.

[14] N. Michel. *The European Physical Journal A*, 42:523, 2009.

[15] A. Nadasen, P. Schwandt, P. P. Singh, W. W. Jacobs, A. D. Bacher, P. T. Debevec, M. D. Kaitchuck, and J. T. Meek. *Phys. Rev. C*, 23:1023, 1981.

[16] J. M. Mueller, R. J. Charity, R. Shane, L. G. Sobotka, S. J. Waldecker, W. H. Dickhoff, A. S. Crowell, J. H. Esterline, B. Fallin, C. R. Howell, C. Westerfeldt, M. Youngs, B. J. Crowe, and R. S. Pedroni. *Phys. Rev. C*, 83:064605, 2011.

[17] H. Dussan, S. J. Waldecker, W. H. Dickhoff, H. Müther, and A. Polls. *Phys. Rev. C*, 84:044319, 2011.

[18] A. H. Bethe. *Phys. Rev.*, 57:1125, 1940.

[19] R. E. Le Levier and D. S. Saxon. *Phys. Rev.*, 87:40, 1952.

[20] R. J. Charity, L. G. Sobotka, and W. H. Dickhoff. *Phys. Rev. Lett.*, 97:162503, 2006.

[21] F. D. Becchetti and G. W. Greenlees. *Phys. Rev.*, 182:1190, 1969.

[22] A.J. Koning and J.P. Delaroche. *Nuclear Physics A*, 713:231, 2003.

[23] R.L. Varner, W.J. Thompson, T.L. McAbee, E.J. Ludwig, and T.B. Clegg. *Phys. Rep.*, 201:57, 1991.

[24] F Perey and B. Buck. *Nucl. Phys.*, 32:353, 1962.

[25] S. J. Waldecker, C. Barbieri, and W. H. Dickhoff. *Phys. Rev. C*, 84:034616, 2011.

[26] R. J. Charity, J. M. Mueller, L. G. Sobotka, and W. H. Dickhoff. *Phys. Rev. C*, 76:044314, 2007.

[27] I. Brida, Steven C. Pieper, and R. B. Wiringa. *Phys. Rev. C*, 84:024319, 2011.

[28] H. de Vries and de Jager C. W. *At. Nucl. Data Tables*, 36:495, 1987.

[29] H. Müther and I. Sick. *Phys. Rev. C.*, 70:041301(R), 2004.

[30] A. Deltuva, A. C. Fonseca, and P. U. Sauer. *Phys. Rev. C.*, 71:054005, 2005.

[31] A. Deltuva, A. C. Fonseca, and P. U. Sauer. *Annu. Rev. Nucl. Part. Sci.*, 58:27, 2008.

[32] G. Jacob and T. A. J. Maris. *Rev. Mod. Phys.*, 45:6, 1973.

[33] S. Frullani and J. Mougey. *Adv. Nucl. Phys.*, 14:1, 1984.

[34] W. H. Dickhoff and C. Barbieri. *Prog. Part. Nucl. Phys.*, 52:377, 2004.

[35] J. M. Udias, P. Sarriaguren, E. Moya de Guerra, E. Garrido, and J. A. Caballero. *Phys. Rev. C*, 51:3246, 1995.

[36] G.J. Kramer, H.P. Blok, J.F.J. Van Den Brand, H.J. Bulten, R. Ent, E. Jans, J.B.J.M. Lanen, L. Lapiks, H. Nann, E.N.M. Quint, G. Van Der Steenhoven, P.K.A. De Witt Huberts, and G.J. Wagner. *Phys. Lett. B*, 227:199, 1989.

[37] N. B. Nguyen, S. J. Waldecker, F. M. Nunes, R. J. Charity, and W. H. Dickhoff. *Phys. Rev. C*, 84:044611, 2011.

[38] D. Rohe, C. S. Armstrong, R. Asaturyan, O. K. Baker, S. Bueltmann, C. Carasco, D. Day, R. Ent, H. C. Fenker, K. Garrow, A. Gasparian, P. Gueye, M. Hauger, A. Honegger, J. Jourdan, C. E. Keppel, G. Kubon, R. Lindgren, A. Lung, D. J. Mack, J. H. Mitchell, H. Mkrtchyan, D. Mocelj, K. Normand, T. Petitjean, O. Rondon, E. Segbefia, I. Sick, S. Stepanyan, L. Tang, F. Tiefenbacher, W. F. Vulcan, G. Warren, S. A. Wood, L. Yuan, M. Zeier, H. Zhu, and B. Zihlmann. *Phys. Rev. Lett.*, 93:182501, 2004.

[39] D. Rohe. *Habilitationsschrift*. University of Basel, Basel, 2004.

[40] A. E. L. Dieperink and T. de Forest. *Phys. Rev. C*, 10:543, 1974.

[41] H. Müther, A. Polls, and W. H. Dickhoff. *Phys. Rev. C*, 51:3040, 1995.

[42] S. C. Pieper and R. B. Wiringa. *Annu. Rev. Nucl. Part. Sci.*, 51:53, 2001.

[43] A. Gade, D. Bazin, B. A. Brown, C. M. Campbell, J. A. Church, D. C. Dinca, J. Enders, T. Glasmacher, P. G. Hansen, Z. Hu, K. W. Kemper, W. F. Mueller, H. Olliver, B. C. Perry, L. A. Riley, B. T. Roeder, B. M. Sherrill, J. R. Terry, J. A. Tostevin, and K. L. Yurkewicz. *Phys. Rev. Lett.*, 93:042501, 2004.

[44] O. Jensen, G. Hagen, M. Hjorth-Jensen, B. Alex Brown, and A. Gade. *Phys. Rev. Lett.*, 107:032501, 2011.

[45] R.J. Charity, W.H. Dickhoff, L.G. Sobotka, and S.J. Waldecker. *Eur. Phys. J. A*, 50, 2014.

[46] R. Machleidt, F. Sammarruca, and Y. Song. *Phys. Rev. C*, 53:R1483, 1996.

[47] R. B. Wiringa, V. G. J. Stoks, and R. Schiavilla. *Phys. Rev. C*, 51:3, 1995.

[48] H. Müther and W. H. Dickhoff. *Phys. Rev. C*, 72:054313, 2005.

[49] B. E. Vonderfecht, W. H. Dickhoff, A. Polls, and A. Ramos. *Phys. Rev. C*, 44:R1265, 1991.

[50] G. W. Greenlees, G. J. Pyle, and Y. C. Tang. *Phys. Rev.*, 171:1115, 1968.

[51] C. Barbieri and W. H. Dickhoff. *Phys. Rev. C*, 63:034313, 2001.

[52] C. Barbieri and W. H. Dickhoff. *Phys. Rev. C*, 65:064313, 2002.

[53] G. Hagen and et al. *Nature Physics*, 2015.

[54] R. Shane, R.J. Charity, J.M. Elson, L.G. Sobotka, M. Devlin, N. Fotiades, and J.M. ODonnell. *Nucl. Instru. Meth. A*, 614:468, 2010.

[55] C. J. Horowitz, S. J. Pollock, P. A. Souder, and R. Michaels. *Phys. Rev. C*, 63:025501, 2001.

[56] J. Mammei et al. CREX: Parity-violating measurement of the weak charge distribution of ^{48}Ca to 0.02 fm accuracy. 2015.

[57] C. J. Horowitz, Z. Ahmed, C.-M. Jen, A. Rakhman, P. A. Souder, M. M. Dalton, N. Liyanage, K. D. Paschke, K. Saenboonruang, R. Silwal, G. B. Franklin, M. Friend, B. Quinn, K. S. Kumar, D. McNulty, L. Mercado, S. Riordan, J. Wexler, R. W. Michaels, and G. M. Urciuoli. *Phys. Rev. C*, 85:032501, 2012.

[58] F. J. Fattoyev and J. Piekarewicz. *Phys. Rev. C*, 86:015802, 2012.

[59] PREXII. http://hallaweb.jlab.org/parity/prex/prexii.pdf. 2015.

[60] A. Abrahamyan et al. *Phys. Rev. Lett.*, 108:112502, 2012.

[61] T. Otsuka, T. Suzuki, R. Fujimoto, H. Grawe, and Y. Akaishi. *Phys. Rev. Lett.*, 95:232502, 2005.

[62] Seth Waldecker. Improving the dispersive optical model toward a dispersive self-energy method. *Ph.D. thesis Washington University*, 2011.

Appendices

A

^{40}Ca parameters

The HF parameters are shown in Table A.1. We note that the number of parameters is the same as for the local HF potential employed in Ref. [16]. The corresponding equations where these parameters are introduced have also been listed in this table. The spin-orbit parameters are gathered in Table A.2. We have kept the parameters of the imaginary component fixed to the values found in Ref. [16] as indicated by the asterisk.

The parameters pertaining to volume absorption are displayed in Table A.3. Motivated by the theoretical work of Refs. [25, 17], we allow for different nonlocalities above and below the Fermi energy. While we observe small differences for the radius and diffuseness parameters other parameters show very minor differences and could have been kept identical above and below the Fermi energy in the fit.

Surface absorption parameters are collected in Table A.4. We have abandoned a strict symmetry assumption for the surface-absorption parameters but the values displayed in Table A.4 indicate that most parameters acquire very similar values above and below the Fermi energy and a symmetric version may be restored in future work. Since the emphasis of surface absorption is around the Fermi energy, it removes about as much single-particle strength

Table A.1: Fitted parameter values for the proton and neutron nonlocal HF potential in ^{40}Ca. The table also contains the number of the equation that defines each individual parameter.

parameter	value	Eq.
V_{HF}^0 [MeV]	100.06	(3.1)
r^{HF} [fm]	1.10	(3.1)
a^{HF} [fm]	0.68	(3.1)
β_{vol_1} [fm]	0.66	(3.1)
β_{vol_2} [fm]	1.56	(3.1)
x_1	0.48	(3.1)
V_{wb}^0 [MeV]	15.0	(3.2)
ρ_{wb} [fm]	2.06	(3.2)
β_{wb} [fm]	1.10	(3.2)

Table A.2: Fitted parameter values for the local HF and imaginary spin-orbit potentials in ^{40}Ca. For those parameters indicated by an asterisk we kept the same values as in Ref. [16]. The table also contains the number of the equation that defines each individual parameter.

parameter	value	Eq.
$V_0^{so}[MeV]$	6.03	(3.4)
r^{so} [fm]	1.02	(3.4)
a^{so} [fm]	0.66	(3.4)
A^{so} [MeV]	-3.65(*)	(3.12)
$B^{so}[MeV]$	208(*)	(3.12)

Table A.3: Fitted parameter values for proton and neutron potentials in ^{40}Ca that determine volume absorption. The table also contains the number of the equation that defines each individual parameter.

parameter	value	Eq.
r_{vol}^{+} [fm]	1.37	(3.6)
a_{vol}^{+} [fm]	0.68	(3.6)
β_{vol}^{+} [fm]	0.64	(3.6)
r_{vol}^{-} [fm]	1.44	(3.6)
a_{vol}^{-} [fm]	0.50	(3.6)
β_{vol}^{-} [fm]	0.81	(3.6)
A_{+}^{vol} [MeV]	7.74	(3.8)
B_{+}^{vol} [MeV]	25.87	(3.8)
E_{p+}^{vol} [MeV]	13.59	(3.8)
A_{-}^{vol} [MeV]	9.50	(3.8)
B_{-}^{vol} [MeV]	27.29	(3.8)
E_{p-}^{vol} [MeV]	5.50	(3.8)
α [MeV$^{-1/2}$]	0.125	(3.9)
E_{a}^{+} [MeV]	19.59	(3.9)
E_{a}^{-} [MeV]	120	(3.9)

Table A.4: Fitted parameter values for proton and neutron potentials in ^{40}Ca that determine surface absorption. The table also contains the number of the equation that defines each individual parameter.

parameter	value	Eq.
r_{sur}^{+} [fm]	1.15	(3.6)
a_{sur} [fm]	0.60(*)	(3.6)
β_{sur}^{+} [fm]	0.94	(3.6)
r_{sur}^{-} [fm]	1.19	(3.6)
β_{sur}^{-} [fm]	2.07	(3.6)
A_{+}^{sur} [MeV]	12.31	(3.10)
B_{+s1}^{sur} [MeV]	13.87	(3.10)
B_{+s2}^{sur} [MeV]	36.62	(3.10)
C_{+}^{sur} [MeV]	17.21	(3.10)
A_{-}^{sur} [MeV]	7.21	(3.10)
B_{-s1}^{sur} [MeV]	14.34	(3.10)
B_{-s2}^{sur} [MeV]	25.46	(3.10)
C_{-}^{sur} [MeV]	17.33	(3.10)

B

^{48}Ca parameters

In the following table the parameters for the ^{48}Ca self-energy are collected that optimize the nonlocal self-energy for this nucleus.

Table B.1: All relevant parameters for the HF, volume and SO parts of the nonlocal DOM self-energy for ^{48}Ca are collected below.

parameter	value	Eq.
$\alpha_{HF}^{asym(p)}$ [MeV]	1.24	(4.1)
$\alpha_{HF}^{asym(n)}$ [MeV]	5.62	(4.1)
$r_{asym}^{HF(p)}$ [fm]	1.53	(4.1)
$r_{asym}^{HF(n)}$ [fm]	1.03	(4.1)
$\beta_{vol1(p)}^{asym}$ [fm]	1.56	(4.1)
$\beta_{vol1(n)}^{asym}$ [fm]	1.56	(4.1)
$V_{NZ}^{so(p)}$ [MeV]	-1.31	(4.2)
$V_{NZ}^{so(n)}$ [MeV]	-20.30	(4.2)
$C_{asym}^{vol(p)}$ [MeV]	1.00	(4.7)
$C_{asym}^{vol(n)}$ [MeV]	18.00	(4.7)

Table B.2: The parameters that determine the surface asymmetry part of the nonlocal DOM self-energy for ^{48}Ca are collected below.

parameter	value	Eq.
$\beta_{sur,p}^{asym-}$ [MeV]	1.87	(4.8)
$\beta_{sur,n}^{asym-}$ [MeV]	0.56	(4.8)
$\beta_{sur,p}^{asym+}$ [MeV]	1.44	(4.8)
$\beta_{sur,n}^{asym+}$ [MeV]	0.61	(4.8)
$A_{asym+}^{sur,p}$ [MeV]	4.01	(4.4)
$A_{asym+}^{sur,n}$ [MeV]	4.04	(4.4)
$A_{asym-}^{sur,p}$ [MeV]	4.50	(4.4)
$A_{asym-}^{sur,n}$ [MeV]	1.00	(4.4)
$B_{asym+s1}^{sur,p}$ [MeV]	13.86	(4.4)
$B_{asym+s1}^{sur,n}$ [MeV]	15.86	(4.4)
$B_{asym-s1}^{sur,p}$ [MeV]	14.34	(4.4)
$B_{asym-s1}^{sur,n}$ [MeV]	14.34	(4.4)
$B_{asym+s2}^{sur,p}$ [MeV]	17.20	(4.4)
$B_{asym+s2}^{sur,n}$ [MeV]	15.08	(4.4)
$B_{asym-s2}^{sur,p}$ [MeV]	17.32	(4.4)
$B_{asym-s2}^{sur,n}$ [MeV]	17.32	(4.4)
$C_{asym+}^{sur,p}$ [MeV]	36.62	(4.4)
$C_{asym+}^{sur,n}$ [MeV]	40.46	(4.4)
$C_{asym-}^{sur,p}$ [MeV]	25.46	(4.4)
$C_{asym-}^{sur,n}$ [MeV]	25.46	(4.4)
$r_{asym+}^{sur(p)}$ [fm]	1.06	(4.8)
$r_{asym+}^{sur(n)}$ [fm]	1.45	(4.8)
$r_{asym-}^{sur(p)}$ [fm]	1.29	(4.8)
$r_{asym-}^{sur(n)}$ [fm]	1.19	(4.8)